Experimental Validation of Wet Compression with a Twin Screw Compressor Prototype

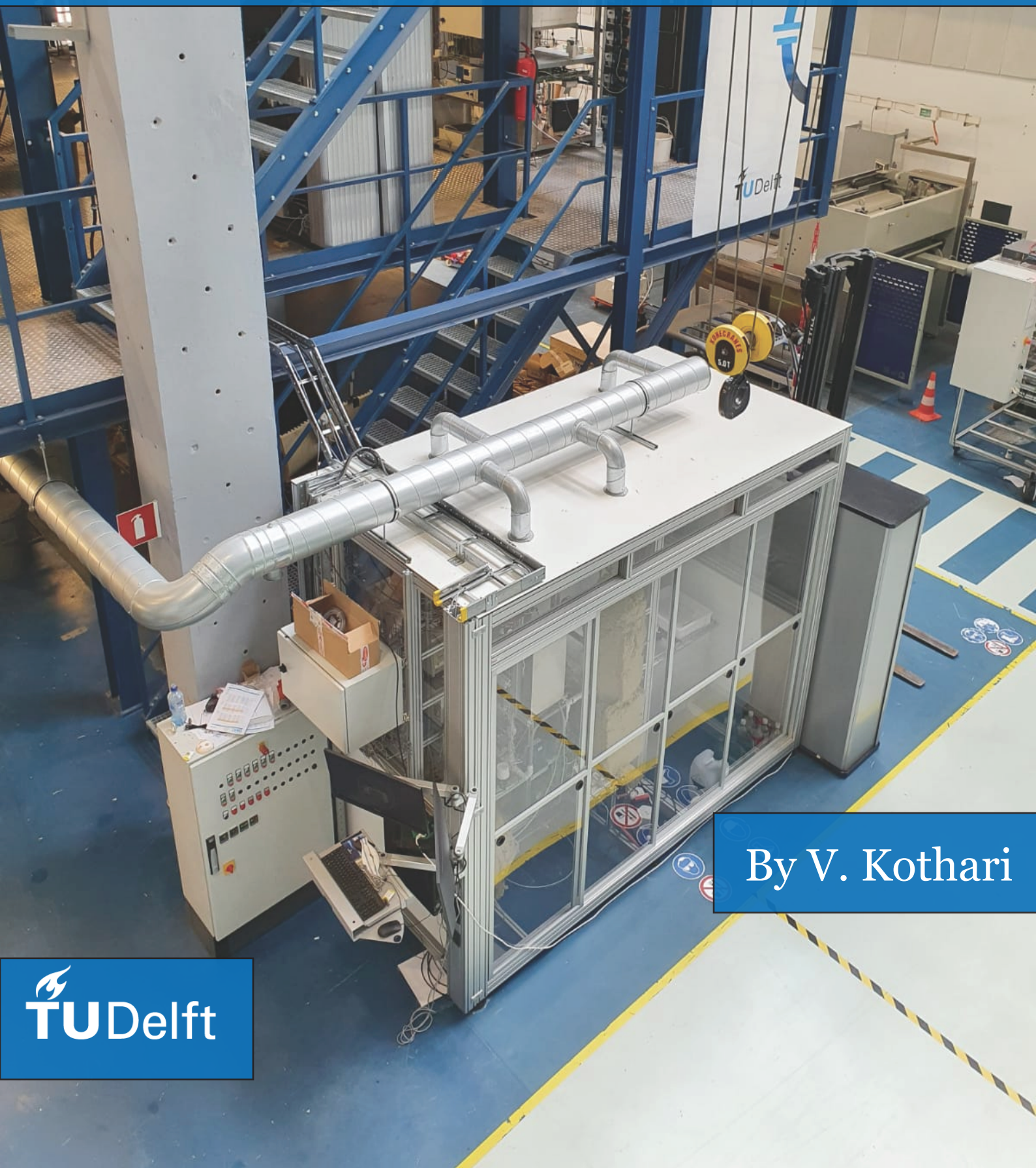

By V. Kothari

TUDelft

Experimental validation of wet compression with a twin screw compressor prototype

by

V. Kothari

[ME 55035 including ME 55010]

to obtain the degree of Master of Science
at the Delft University of Technology.
to be defended publicly on Monday September 21, 2020 at 10:00 AM.

Student number:	4796195	
Project duration:	January 6, 2020 – September 21, 2020	
Thesis committee:	Dr. Ir. C.A. Infante Ferreira,	TU Delft, Chair & Supervisor
	Prof. Dr. Ir. T. J. H. Vlugt,	TU Delft
	Dr. Ir. R. Delfos,	TU Delft
	Dr. Ir. V. Gudjonsdottir	
	Ir. A. Goethals,	Atlas Copco

TU Delft

Abstract

According to Spoelstra et al. (2018) 80% of the current greenhouse gas emissions are due to the demand for energy, mostly in the form of electricity and heat. The industrial sector accounts for almost 32% of global greenhouse gas emissions. Hence, decarbonising these energy carriers has attracted much attention. This decarbonisation can be done through various routes: reducing the final energy consumption by improving process conditions and efficiency, reusing waste heat and by an outright energy transition to renewable sources. In this study, the focus is on reusing waste heat. Heat pumps have the potential to drastically reduce energy requirements in the industry and in that way reduce emissions (Kiss and Infante Ferreira, 2017). van de Bor et al. (2015) compared different heat pump technologies and for industrial applications where there is a temperature glide of the heat source and/or sink compression-resorption heat pumps (CRHP) utilizing wet compression can achieve higher coefficient of performance (COP) than alternative technologies. However, an isentropic efficiency of 70% for the compressor was assumed. If this limit is not reached there might be no advantage of wet compression compared to the traditionally used vapour compression heat pump (VCHP) as pointed out by several authors (Itard and Machielsen (1994), and Zaytsev (2003)). This study consists of experimental and modelling aspects. The compressor model is experimentally validated in this thesis.

A deep knowledge about relevant topics like wet compression, compressor specifications, thermodynamic and geometrical models is developed before starting off with the experiments. The experiments are carried out for four rotational speeds: 10320 rpm, 12910 rpm, 14205 rpm and 15500 rpm, taking system constraints into account. Two approaches are considered here: the homogeneous approach and the heterogeneous approach. In the homogeneous approach, the concentration of ammonia is constant across the compressor and process medium is treated as a single entity. In the heterogeneous approach, an assumption is made: only the vapour is compressed whereas the liquid exchanges heat with the vapour leading to partial evaporation.

Higher pressure ratios and temperature lifts can be attained with lower inlet vapour qualities at the same speed. This is an advantage of using wet compression. For the homogeneous approach, the power required by the compressor increases as the rotational speed increases. The cooling water not only removes heat from the mechanical components like bearings, seals and gearbox but also a part of the process heat. The heat removed by the cooling water is higher for higher rotational speeds. The isentropic efficiency increases as the amount of liquid in the compressor increases. The highest isentropic efficiency is found to be 44%. The trend of the isentropic efficiency for higher rotational speeds is not exactly straightforward. It is seen that the vapour leaving the compressor might be superheated. The mechanical efficiency is practically independent of the inlet vapour quality and pressure ratio, with an average of 74%. However, the mechanical efficiency is sensitive to changes in the magnitude of the heat removed by the cooling water. The volumetric efficiency increases with an increase in the inlet vapour quality and reduces at higher pressure ratios. For the heterogeneous calculation scheme, the required compression power is much less than that for the homogeneous calculation scheme. The power required for compression reduces as the amount of liquid in the compressor reduces. Higher isentropic efficiencies are achieved using the heterogeneous scheme. The highest isentropic efficiency is 75% which is above the threshold. The isentropic efficiency increases until an inlet vapour quality of ca. 0.76 and a pressure ratio of ca. 3.0 and then decreases. The mechanical efficiency reduces with an increase in the amount of vapour in the compressor and increases with pressure ratio for all rotational speeds. Reproducibility of the experimental results is checked and confirmed for 10320 rpm after two months of operation at higher rotational speeds.

The model developed by Guðmundsdóttir (2018) is based on a finite volume method. This model uses governing equations, compressor port properties and leakage paths that were developed and used by Zaytsev (2003) and Tang (1995). The model needed to be fine-tuned to provide accurate data. The compressor port sizes and locations were updated using a similar twin-screw compressor. The

effect of various factors such as clearance, leakage sizes and flow coefficients is seen on the isentropic and volumetric efficiencies. The clearance has the most prominent influence on the efficiencies causing a 21% drop in isentropic efficiency and 4.2% drop in volumetric efficiency when it is increased from 0.05 mm to 0.15 mm. Validation of the model making use of the experimental performance is carried out. Optimizing all the contributing variables and the fact that the clearance might increase after prolonged operation, the average difference between the experimental and simulated isentropic efficiency is 6.3% and 31% for the volumetric efficiency. It was concluded that the model is more sensitive to the changes contributing to a change in the isentropic efficiency rather than the volumetric efficiency.

Acknowledgements

This thesis would be incomplete without the people around me. I would to thank them for their unwavering support.

Firstly, I would like to thank my thesis supervisor Dr. Carlos Infante Ferreira for his continued guidance. I was first introduced to Dr. Infante Ferreira in my quarter 1 course: Refrigeration and Heat Pump Fundamentals. It was here I truly developed a liking for this topic which just grew as I progressed through the course. I would like to thank him for inspiring me and imparting his knowledge. Our meetings and discussions always left me with a new approach to the challenge, a new way of thinking. In this thesis, I have learnt the value of perseverance. I have enjoyed working on this study and tackling challenges head on. Sir, thank you for the opportunity.

I would like to give a warm thanks to Dr. Vilborg Gudjonsdottir, my daily supervisor. I enjoyed learning about the topic and the experimental set-up from you. I enjoyed our short but fun-filled time in the Process and Energy Laboratory, which became rather quotidian after you left. I will never forget the amazing smell of ammonia, the gentle itchiness of the glass-wool insulation or playing music in the lab to drown the compressor noise. Thank you for always answering those small and seemingly unimportant questions.

I would like to thank my friends: Nishant, Stefan and Marko for all the great times we have had in these two years. Thank you for the much needed distractions and the company. I would like to give a special thanks to Saloni, who has been a constant support throughout this thesis. Thank you for listening, your advises, your cooking; thank you for just being there. I would like to thank all my other friends, professors and staff at the Energy and Process Technology Department, TU Delft. These two years have been an unforgettable journey. I am grateful that you all are a part of my life.

Lastly, I would like to thank my family. My parents have always been the pillars of my life. They are the reason I am what I am today. My sister, Isha, is the spark of my life. Thank you for always shining so brightly, touching everyone around you. Also, thank you for helping me with the graphics in this report. I do not think I can ever put to words the constant, unrelenting and unwavering support my family has shown me. Making you all proud of me is the best feeling there is.

V. Kothari
Delft, August 2020

Contents

Nomenclature

Roman Symbols

A	Area	mm^2
C	Clearance	mm
C_{fd}	Flow Coefficient for Discharge	
C_{fl}	Flow Coefficient for Leakage	
C_{fs}	Flow Coefficient for Suction	
C_{p}	Specific Heat Capacity at constant pressure	$J(kgK)^{-1}$
D	Gap distance of the plate heat exchanger	m
D_1	Male Rotor Diameter	mm
F	Load	N
$FTip$	Female Rotor Tip Sealing Line Length	mm
g	Gibbs free energy	Jkg^{-1}
H	Enthalpy	J
$HBHole$	Housing Cusp Blow Hole Area	mm^2
h	Specific enthalpy	Jkg^{-1}
$\bar{h}$	Molar specific enthalpy	$Jkmol^{-1}$
L	Length	m
M	Molar mass	$kgkmol^{-1}$
$MTip$	Male Rotor Tip Sealing Line Length	mm
m	Mass of mixture	kg
$\dot{m}$	Mass flowrate	kgs^{-1}
n	Rotational speed of compressor	rpm
$\bar{n}$	Unit Vector	
Pr	Pressure Ratio	
p	Pressure	Pa
$\dot{Q}$	Rate of Heat Transfer	W
q	Vapour quality	$molmol^{-1}$
r	Shaft Radius	mm
$\bar{r}$	Vector from Coordinate Origin to Surface	
r_{evap}	Fraction of evaporation	mm

S	Boundary Surface	m^2
s	Specific entropy	$Jkg^{-1}K^{-1}$
$\bar{s}$	Molar specific entropy	$Jkmol^{-1}K^{-1}$
T	Temperature	K
U	Heat transfer coefficient	$W(m^2K)^{-1}$
u	Uncertainty	
V	Volume	m^3
v	Specific volume	m^3kg^{-1}
$\bar{v}$	Molar specific volume	m^3kmol^{-1}
W	Width	m
$\dot{W}$	Power	W
w	Mass fraction of ammonia in mixture	
$\bar{w}$	Molar fraction of ammonia in vapour-liquid phase	
w_e	Elastic radial load	Nm^{-1}
w_L	Mass fraction of ammonia in liquid phase	
w_v	Mass fraction of ammonia in vapour phase	
$\bar{w_L}$	Molar fraction of ammonia in liquid phase	
$\bar{w_v}$	Molar fraction of ammonia in vapour phase	
z_1	Number of lobes on male rotor	
z_2	Number of lobes on female rotor	

Greek Symbols

Δ	Difference	
δ	Lip contact thickness	mm
η	Efficiency	
μ	Coefficient of Friction	
$\bar{\mu}$	Chemical Potential	$Jmol^{-1}$
ω	Rotational Speed in second	$revs^{-1}$
ρ	Density	kgm^{-3}
φ	Shaft rotation angle	

Subscripts

1	State point 1
2	State point 2
3	State point 3
4	State point 4

abs	Absorber
A	Ammonia
be	Bearings
Carnot	Carnot
comp	Compressor
cw	Cooling Water
c	Critical condition
desorber	Desorber
dis	Discharge
elec	Electric
evap	Evaporation
exp	Experimental
e	Evaporation of liquid
flow	Total Flow
f	Friction
glide	glide
het	Heterogeneous
h	high
ind	Indicated
initial	initial value
inst	Installed
in	Inflow
is	Isentropic
i	Compression element
lift	Lift
LL	Liquid remaining in Liquid Phase
Lorentz	Lorentz
lub	Lubrication
L	Liquid phase
l	low
max	Maximum
mech	Mechanical
model	Model
oil	oil

out	Outflow	
process	Process side	
process	process	
rotor	Rotor	
se	Seals	
sink	Sink	
source	Source	
sub	Subcooler	
suc	Suction	
s	Shaft	
total	Total	
vL	Liquid Formed from Vapour	
vol	Volumetric	
v	Vapour phase	
WW	waste water	
W	Water	

Abbreviations

COP	Coefficient of performance	
CRHP	Compression resorption heat pump	
CWR	Cooling Water Return	
CW	Cooling Water	
EU	European Union	
GWP	Global warming potential	
HACHP	Hybrid absorption compression heat pump	
IHEX	Internal Heat Exchanger	
IPCC	Intergovernmental Panel for Climate Change	
NG	Natural Gas	
TDF	Temperature driving force	K
UNFCCC	United Nations Framework Convention on Climate Change	
VCHP	Vapour compression heat pump	
VHC	Volumetric Heat Capacity	MJm^{-3}

1

Introduction

Strive not to be Successful, but to achieve Excellence. Success will inevitably follow.

Indian Proverb

Climate change is a phenomenon that has always occurred throughout history. We know this by studying ice cores, corals, layers of sedimentary rocks, ocean sediments and tree rings. Many of these changes are due to slight variations in the orbit of the Earth which subsequently change the amount of solar energy it receives from the sun. However, Shaftel et al. (2020) mention that since the mid-20th century, this warming has accelerated to unprecedented degrees, largely due to human activities. Edenhofer et al. (2014) mention in an International Panel of Climate Change (IPCC) report that the Earth's surface temperature has increased, the amounts of snow and ice have diminished and sea levels have risen. So, climate change is not something that has suddenly started. From paleoclimate data, there have been times when the Earth has been warmer than it is today. But this data also reveals that the current warming is occurring at a much higher rate than ever before.

Taking this into consideration, there have been several legislations regarding climate change and reducing greenhouse gas emissions. The Kyoto Protocol in 1997 was the first agreement between nations to reduce emissions of six greenhouse gases by 5% compared to their 1990 levels. According to a report by Amanatidis (2019), in 2012 this percentage was increased to 20%. The European Union (EU) changed this percentage again in 2014 to achieve greenhouse gas emissions 40% below 1990 levels by 2030. This formed the basis of the Paris Agreement. On 12 December 2015, The United Nations Framework Convention on Climate Change (UNFCCC) adopted the Paris Agreement. As mentioned in the report by Amanatidis (2019) the main goal of this agreement is to limit the rise in global temperature to 2°C while pursuing efforts to limit it to 1.5°C. In November 2018, the EU has committed to a strategy enabling a climate neutral economy by 2050.

According to Spoelstra et al. (2018) 80% of the current greenhouse gas emissions are due to the demand for energy, mostly in the form of electricity and heat. Hence, decarbonising these energy carriers has attracted much attention. The industrial sector accounts for almost 32% of global greenhouse gas emissions. Energy intensive sectors of industry such as the iron and steel, oil refineries, chemicals and petrochemicals, food, non-metallic minerals, non-ferrous metals and the paper and pulp industry make up of 69% of the total energy consumption. In almost all of them, heat is the primary energy carrier. In 2012, thermal energy, that is, process heat and cooling accounted for 73% of the final energy consumption.

Keeping the above data in mind, for the EU to meet these energy targets, technical innovation and utilization of low carbon energy sources are key along with remaining in a competitive state. This decarbonisation can be done through various routes: reducing the final energy consumption by improving process conditions and efficiency, reusing waste heat and by an outright energy transition to renewable

energy sources.

The reuse of waste heat or excess heat has historically been seen by many as underutilized and undervalued and for good reason. The waste heat is usually discarded to the environment at temperatures which are too low for its reuse. One option then is to recover heat from these waste streams and upgrade their temperature to the required process condition. Heat pumps are a growing technology for industrial heat recovery applications. They have the potential to increase the industrial energy efficiencies by drastically reducing the energy requirements. Heat pumps require an input of heat and electricity. Utilizing renewable electricity to power heat pumps can also be a robust technology for reaching goals of sustainability. Hence, heat pumps are a technology that can not only retrofit current energy industries but also have a significant impact in the future for renewable applications. Gudjonsdottir (2020) mentions that historically heat pumps have not been widely accepted and integrated into energy systems majorly due to their large payback periods. New legislation and the ever-increasing socio-economic impacts of greenhouse emissions have attracted renewed interest in this technology.

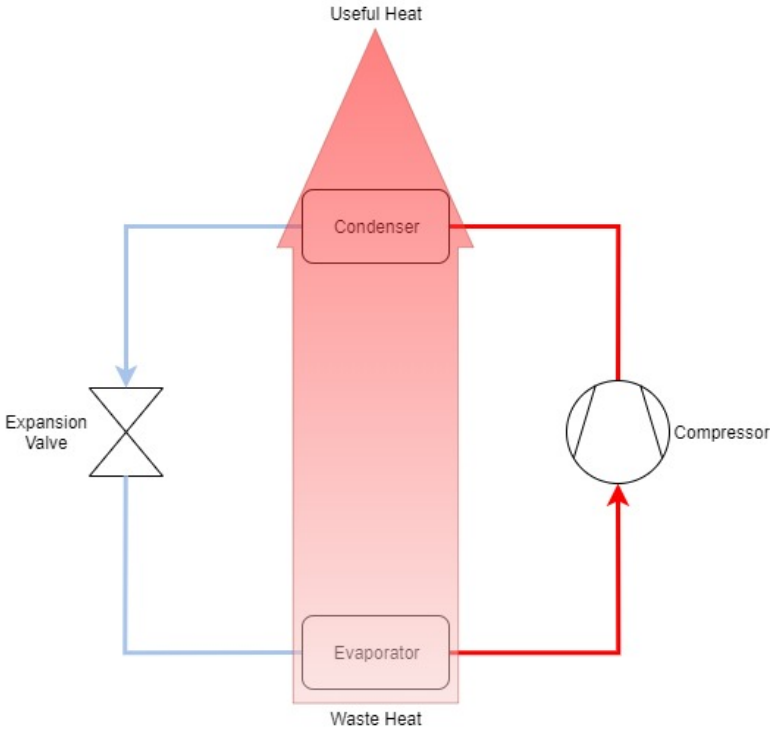

Figure 1.1: Heat Pump Schematic

1.1. Heat Pumps

Heat pumps, as the name suggests, pump heat (or energy) in the opposite direction, that is, from the colder space to the warmer space.The working principle of heat pumps is based on the physical property of the working fluid: the boiling point increases with increase in pressure. Hence, at low pressures the fluid can be evaporated (at low temperatures) and at high pressures it can be condensed (at high temperatures) (Kiss and Infante Ferreira, 2017). A schematic of a simple, conventional vapour compression heat pump (VCHP) is shown in Figure 1.1. Research is currently underway to improve its performance and efficiency by trying various configurations and refrigerants. One configuration that has shown potential is the compression-resorption heat pump (CRHP).

In this configuration, the evaporator and condenser are replaced by a desorber and resorber respectively. Heat is absorbed in the desorber and released in the resorber. CRHP's are particularly interesting in applications where there are high sink temperatures and high temperature glides of the heat source and/or the heat sink. This is due to reduction in vapour pressure and the non-isothermal

phase change of the zeotropic mixture, ammonia-water which is used as an absorption pair. The composition of the working fluid will change according to the different boiling points of ammonia and water. Hence, using such a binary mixture enables condensation and evaporation at gliding temperatures, attaining high temperatures at relatively lower pressure levels and hence higher efficiency and relatively higher coefficient of performance (COP). The non-isothermal phase change allows the temperature profiles across the desorber and resorber to match those of the external circuit. Therefore entropy generation caused by heat transfer over a limited temperature difference is reduced. Consequently, CRHPs are one of the feasible measures to approach the Lorentz cycle (Jensen et al., 2015b).

For industrial applications, CRHP's have an energy performance gain of over 20% over VCHP's (van de Bor et al., 2015). Moreover, both ammonia and water have 0 global warming potential (GWP) which also makes ammonia-water a suitable working fluid. A cycle comparison is shown in Figure 1.2.

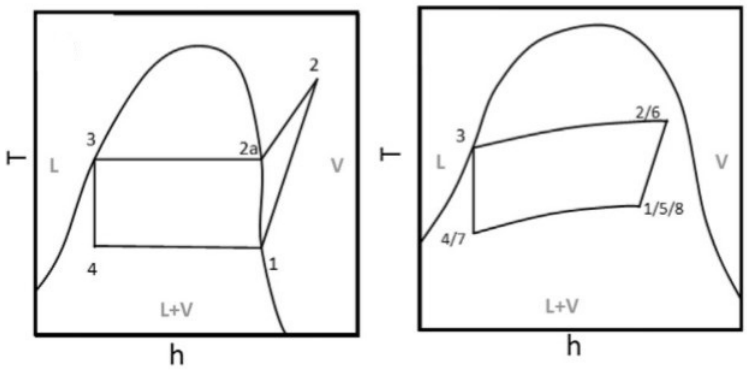

Figure 1.2: *T-h* diagrams for vapour compression heat pump (left) and compression resorption heat pump (right). As can be seen from the figure, the CRHP works exclusively in the two phase region avoiding the need for superheating. A detailed description of the state points can be found in van de Bor et al. (2015).

1.2. Compression Resorption Heat Pumps in Industry

An interesting application is the reuse of return waste heat streams of district heating to be used in industrial plants (van de Bor et al., 2015). These streams generally have a temperature of 40°C-60°C. Hence, to reuse, they either need to be heated up to high temperatures - to be used for heating - or cooled down to lower temperatures - to be used as cooling water. Hence, they can serve a dual purpose: they can be further cooled down (in the desorber) or heated back up (in the resorber) using a CRHP. Figure 1.3 illustrates this concept. Using wet compression (liquid as well as vapour is compressed in the compressor), superheating can be eliminated. This means that the heat pump can handle even higher temperatures of the waste heat stream. The waste water is split into two streams for the cold and hot utilities. CRHP's are particularly interesting to upgrade waste heat streams when there is a temperature glide involved (Gudjonsdottir, 2020). A temperature glide is the difference between the saturated vapour temperature and the saturated liquid temperature at constant pressure for zeotropic mixtures. Therefore, the temperature glide of the mixture can be matched with the temperature glide of the heat source/sink by varying the mixture composition (Gudjonsdottir, 2020).

1.3. Thesis Scope

In previous research, it has been proven that compression resorption heat pumps utilizing wet compression have a higher COP (van de Bor et al., 2015). However, a critical assumption was made here: the isentropic efficiency of the compressor was taken to be 70%. This threshold must be reached in order for CRHP's using wet compression to have a feasible advantage over conventional VCHP's (Itard, 1998). One way to increase this efficiency is to reduce the irreversibilities in the system (Gudjonsdottir, 2020). At TU Delft, a prototype twin-screw compressor, manufactured by Atlas Copco, is being used in this study. A simple schematic of the experimental set-up can be seen in Figure 1.4. Compressor models for an ammonia-water mixture and an ammonia-carbon dioxide-water mixture have already been developed. However, these models need to be fine-tuned for the current compressor prototype.

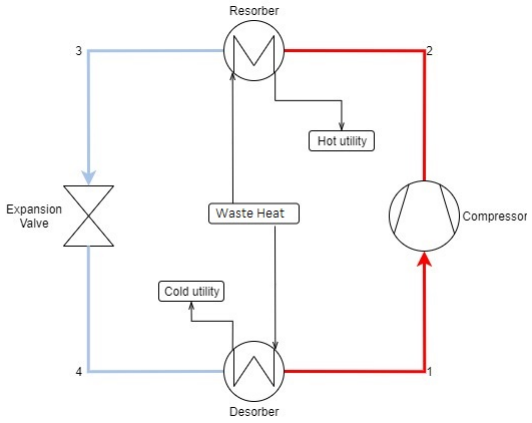

Figure 1.3: Schematic of a Compression Resorption Heat Pump

Therefore, this research project has one aim: to try to reach 70% isentropic efficiency of the compressor. For this, the existing compressor models need to be experimentally validated. Hence, a series of experiments will be developed and carried out based on these MATLAB models. This study solely focuses on the performance of the twin-screw compressor which forms a part of the compression resorption heat pump. In order to reach this aim, several research questions need to be answered:

- For different rotational speeds of the compressor and vapour qualities of the ammonia-water mixture, what is the performance of the twin-screw compressor prototype?
- Experimentally, what are the advantages and disadvantages of utilizing wet compression in this set-up?
- How can the current compressor model be optimized in order to predict the experimentally determined compressor performance?
- What is the performance of the compressor as determined by the compressor model? Is this performance in agreement with the experimentally determined performance?
- What are the future prospects of this study?

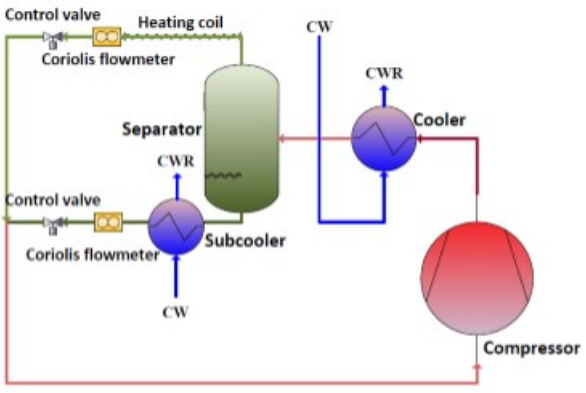

Figure 1.4: A simplified Process and Instrumentation Diagram of the experimental set-up at TU Delft. After the compressor, the process medium is cooled in the absorber using cooling water (CW). Here CWR refers to the return cooling water. The flow is then separated into vapour and liquid lines. Coriolis flowmeters measure the flow in the vapour and liquid line.

1.4. Thesis Methodology

Figure 1.5 gives an overview of the research methodology that will be used in this thesis. A detailed literature review will be carried out on compression resorption heat pumps that use dry compression via the Osenbruck cycle and those that use wet compression. A comparison will be drawn between them and the decision made to use wet compression will be justified.

This thesis consists of two methods: experimental and simulation. A model has been developed to simulate the compressor so that its performance and characteristics can be investigated. In order to validate this performance, an experimental plan will be developed and executed. Before carrying out the experiments, certain aspects of the setup need to be upgraded, for example, the discharge temperature sensors. After this is done, the experiments will be carried out in a sequence of increasing rotational speed of the compressor. The raw data will then be post-processed and subsequently analysed. The compressor port and leakages sizes and timings used to the model need to be altered for greater accuracy. Using the experimental operating conditions, the model will be simulated in MATLAB. Results of both, the experiments and the simulations, will be discussed. This experimental performance data will then be compared to the performance as predicted by the model. Lastly, conclusions and recommendations will be made.

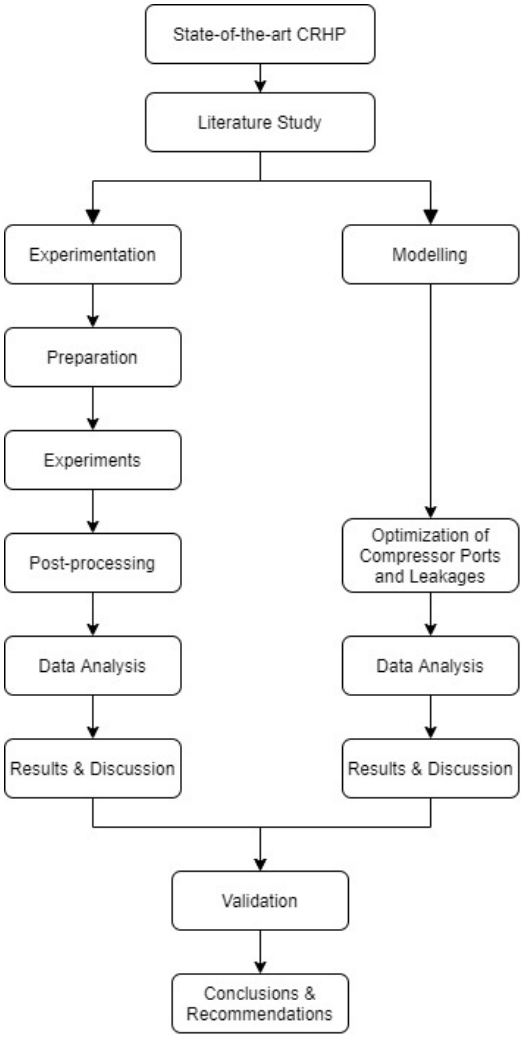

Figure 1.5: Thesis Research Methodology. Experimentation will be carried out first. The operating conditions of the experiments will be put into the model. Subsequently, validation of the model by using the experimental performance will be carried out.

1.5. Thesis Report Outline

Chapter 1 gives the introduction of the thesis, briefly describing the current trends of energy consumption and climate changes. It emphasizes on one potential solution: reusing waste heat through heat pumps. Furthermore, this chapter provides a peek into the current study stating the scope, research questions and methodology.

Chapter 2 talks about the relevant literature survey done for this study. It justifies why wet compression is utilized here by drawing a comparison to the dry compression cycle (Osenbruck cycle). This chapter introduces and explains twin-screw compressors. Relevant experimental research done with twin-screw compressors is also discussed here. Furthermore, the geometric and thermodynamic aspects of the compressor models are discussed. The thermodynamic properties of the process medium (ammonia-water) are also mentioned here.

Chapter 3 is about the experimental aspect of this study. It describes the compressor and the experimental set-up being used. It talks about the sensors used in the set-up along with the necessary preparation needed to start the experiments. It gives an overview of the experimental procedure and certain constraints that need to be taken into account while performing the experiments. Subsequently, it contains the two approaches taken for data analysis: the homogeneous approach and the heterogeneous approach. Lastly, the results from the experiments are discussed.

Chapter 4 deals with the modelling aspect of this study. First, a comparison is drawn between the compressor used in this study and the ones used by Tang (1995) and Zaytsev (2003). A complete geometric comparison is drawn, including port sizing and leakage path estimation. Along with this, port timing determination of the compressor used in this study is elaborated. Subsequently, the results from the compressor model are discussed and the effect of various factors such as clearance, leakages paths, pressure drop etc., on the compressor performance can be seen. Furthermore, this chapter contains the model optimization and validation.

Chapter 5 is the conclusion of this study. It contains all the major conclusions drawn from this thesis along with important recommendations for future work on this project.

2

Background

Knowledge gives Humility, from Humility, one attains Character; From Character, one acquires Wealth; from Wealth, Righteousness follows and then one attains Happiness

Bhagavad Gita

In this chapter, a detailed background of compression resorption heat pumps is provided. Research which has already been carried out on this project has been summarized. Several key questions have been answered - why CRHP with wet compression, what are twin screw compressors, what are the possible alternatives - to name a few. A comparison is drawn between the highly developed Osenbruck Cycle and a wet compression cycle. Relevant research done on the Osenbruck cycle is summarized in Table 2.1 and then compared to a CRHP with wet compression in Table 2.2. For a complete study regarding a CRHP, a model has been developed by TU Delft containing two sections: a thermodynamic or performance section and a geometrical section. Previous work done on both sections have been described here. Since ammonia-water is used as the working fluid, its thermodynamic properties are included in the chapter. This chapter ends with conclusions which are drawn from this literature survey forming the foundation of the forthcoming chapters.

2.1. Compression Resorption Heat Pumps with Dry and Wet Compression

As is known, compression resorption heat pumps are characterized by using a refrigerant-absorbent pair that has a wide boiling temperature range. Evaporation of this mixture in the desorber is not complete, so the fluid leaving the desorber is a vapour/liquid mixture. There are two ways to implement the cycle. Osenbruck (1895) developed the Osenbruck cycle. The second way is to use a wet compression cycle.

2.1.1. Dry Compression

A general representation of this cycle is shown in Figure 2.1 (a). Such a system is usually called a hybrid absorption compression heat pump (HACHP). Heat is supplied from the heat source to the desorber. After the desorber, the vapour/liquid mixture is separated using a liquid-vapour separator. The vapour phase is sent to the compressor while the liquid phase is recirculated using a solution pump. This liquid stream is lean (weak in ammonia). After passing through a solution heat exchanger, the liquid stream and the compressed vapour stream are mixed before entering the absorber. Diabatic absorption of the ammonia vapour into the lean liquid takes place in the absorber releasing heat to the sink. The ammonia-water stream exiting the absorber is a saturated liquid mixture. This stream is then subcooled

and throttled to a lower pressure before passing through the desorber to complete the cycle.
In Figure 2.1 (b), the temperature lift as shown in equation 2.1 is defined as:

$$\Delta T_{\text{lift}} = T_{\text{sink,out}} - T_{\text{source,in}} \tag{2.1}$$

The temperature differences of the source and sink are between the inlets and outlets of the source and sink respectively. We can observe from the figure that the profiles of the equilibrium absorption and desorption process are non-linear. Here, they are shown as convex curves, but they could also be concave or both (depending on the circulation ratio and the mass fraction of ammonia). Therefore, when modelling an HACHP, a positive temperature difference must be maintained across the length of the heat exchangers and not just at the inlets and outlets (Jensen et al., 2015b).

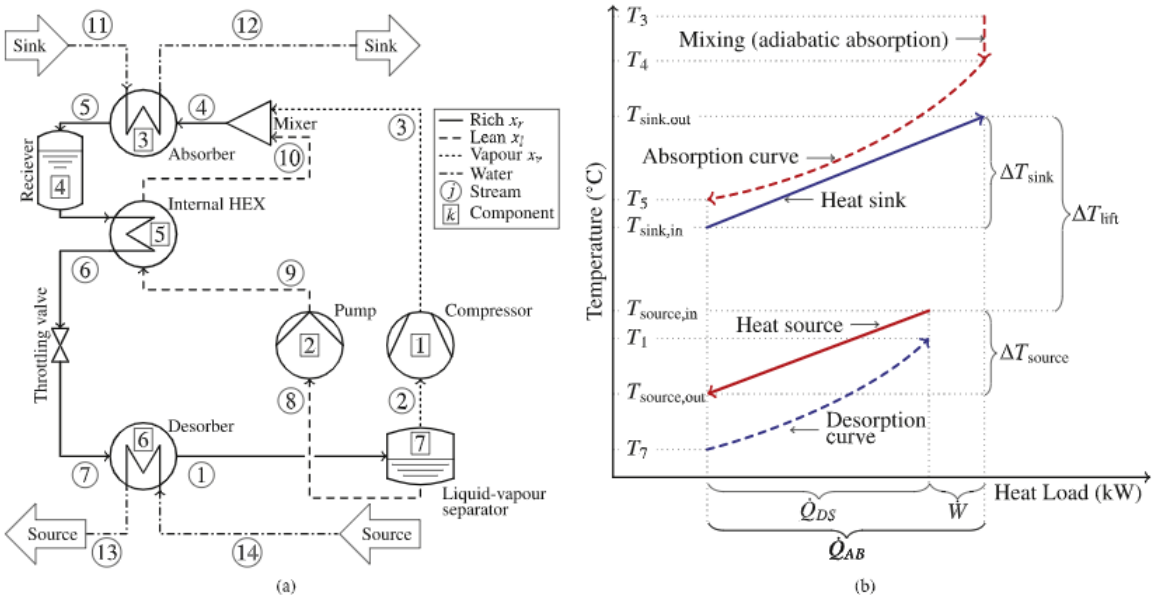

Figure 2.1: (a) The Osenbruck cycle schematic for the HACHP process and (b) the corresponding temperature - heat load diagram (Jensen et al., 2015b)

Jensen et al. (2015b) compared an HACHP working with ammonia-water to a conventional VCHP with natural working fluids - R717 and R600a. They investigated the feasibility of an HACHP based on an economic analysis as well as a technical analysis. The design variables were the mass fraction of ammonia and the circulation ratio (the ratio of the mass of the rich mixture to the mass of the lean mixture). They had the following conclusions:

- HACHP delivers higher heat supply temperature and higher temperature lifts than conventional VCHPs.
- Heat supply temperatures up to 150°C and temperature lifts of 60 K are attainable using commercially available equipment. They also show an economic benefit compared to natural gas combustion in burners.
- The significant constraint to HACHP is the compressor discharge temperature. This could be reduced by using a two stage compressor. This constraint could also be relaxed using a cooled screw compressor or an oil-free compressor.
- Reducing the sink/source temperature difference, an increase in the maximum attainable heat supply temperature can be seen while decreasing the temperature lift.
- On comparing the present value of the HACHP with the VCHP, three conclusions were drawn. In general, the HACHP operates at a lower cost when the heat supply temperature is above 80°C, for almost all operating conditions. Secondly, using a VCHP with R717 has virtually no

significant difference and both technologies can be considered for these operating conditions. For high temperature applications, a VCHP is usually used with R600a however HACHP should be applied since it is feasible, both technically and economically, for a wider range of operating conditions.

Jensen et al. (2015a) evaluated working domains for feasible heat supply temperatures for different pressure levels (28 bar, 50 bar and 140 bar). The standard refrigeration cycle (28 bar) is compared with a cycle containing high pressure ammonia components (50 bar) and a cycle using transcritical carbon dioxide (140 bar). The performance depends on the COP, low and high pressure levels, discharge temperature of the compressor, amount of water in the vapour and volumetric heat capacity. These parameters are influenced by ammonia concentration and circulation ratio. Hence, the authors set to find a suitable combination using a numerical model for the three refrigeration cycles. Taking a recommendation from their previous paper, a gas cooler is now used to cool the vapour coming out of the compressor in the HACHP. This heat is given to the sink stream to further heat it up after the absorber. The schematic is the same as shown in Figure 2.1 but with a gas cooler between the compressor and mixer. A design constraint was imposed on the mass fraction of ammonia in the vapour. 5% water was allowed in the ammonia compressors, that is, at 28 bar and 50 bar. The maximum compressor discharge temperature for the ammonia compressors was set at 170°C to avoid degeneration of the lubricant and 250°C for the transcritical CO_2 compressor. The results of the thermodynamic model are derived with constant component inputs like the efficiencies of the compressor and pump, effectiveness of the gas cooler and internal heat exchanger and the pinch point temperature difference of the absorber and the desorber. External operating conditions were also input to the thermodynamic model as constants like the sink temperature difference, the temperature lift, and the mass flows through the sink and source.

It is seen that all performance parameters are influenced by the ammonia concentration and the circulation ratio. Therefore, a correct combination of the two is required for a feasible design. For the three refrigeration cycles, feasible combinations for four heat supply temperatures (100°C, 125°C, 150°C and 175°C) have been analysed. For a heat supply temperature of 100°C, a set of feasible combinations for all three cycles exist. The smallest feasible set belongs to the standard ammonia cycle (28 bar) which is constrained by the compressor discharge temperature and the high pressure. For the high pressure ammonia cycle (50 bar), the set of feasible combinations is constrained by the compressor discharge temperature, the high pressure and the COP. The transcritical CO_2 cycle has the largest set constrained by the compressor discharge temperature, the volumetric heat capacity and the COP. For a heat supply temperature of 125°C, using the standard refrigeration cycle becomes infeasible. The set of feasible combinations for the high pressure ammonia cycle is constrained by the compressor discharge temperature and the high pressure. The transcritical CO_2 cycle is constrained by the same factors as for a heat supply temperature of 100°C, however, the set is larger for heat supply temperature of 125°C. For a heat supply temperature of 150°C, neither the standard nor the high pressure ammonia cycle has a set of feasible combinations because no combinations satisfy the T_{max} < 170°C and COP constraint. The set of feasible combinations for the transcritical CO_2 cycle is even larger and constrained only by the compressor discharge temperature and COP. For a heat supply temperature of 175°C, the transcritical CO_2 cycle is constrained by the compressor discharge temperature, COP and the high pressure which must be less than 140 bar.

Furthermore, the maximum heat supply temperature was also evaluated to get an idea of the attainable temperature levels for the three cycles. At this temperature, no combinations of the ammonia concentration and the circulation ratio will result in a feasible solution. HACHP's using a standard refrigeration cycle can attain a heat supply temperature of 111°C with an unmodified compressor, that is at 28 bar, 129°C at 50 bar and 147°C at 140 bar. If the compressor is modified to enable higher discharge temperatures (T_{max} = 250°C), 127°C can be achieved for the standard refrigeration cycle, 149°C for the high pressure ammonia cycle and 187°C for the transcritical CO_2 cycle. Not considering the mass fraction of ammonia in the vapour, the attainable heat supply temperature further rises to 182°C at 28 bar. At high pressures, this heat supply temperature increases further to 193°C (50 bar), 223°C (140 bar).

Sensitivity analysis shows that the greatest influence on compressor discharge temperature is from

the isentropic efficiency of the compressor. The high pressure is highly influenced by the absorber pinch point temperature difference. The vapour ammonia concentration is not influenced by the varying the component inputs. It was also recommended that in order to evaluate high temperature HACHPs, two stage compressor or an oil-cooled compressor should be used as it might decrease the compressor discharge temperature.

Jung et al. (2018) then investigated the HACHP to produce high temperature process water using an experimental setup which contained a rectifier between the desorber and compressor to ensure high purity ammonia vapour at the inlet. The key parameters studied were the system high pressure, ammonia concentration in the weak solution, liquid and vapour stream flow rates. As the ammonia concentration in the weak solution increases, the absorber heat transfer rate decreases but the COP increases. This is so because the decrease in energy input to the compressor outweighs the slow heat transfer in the absorber. The maximum absorption heat transfer rate increases as the system pressure increases. When this happens, the amount of ammonia generated in the desorber will also increase thereby increasing the power required by the compressor and hence reducing the COP. Hence, the authors found an optimal range of operating conditions. They concluded that the most significant factor to obtain high temperature process water is the ammonia concentration in the weak solution which should be kept between 0.4-0.45 while keeping the weak solution flow rate less than 0.03 kg/s and the pressure greater than 17 bar to obtain process water temperatures of greater than 80°C.

Kim et al. (2013) experimentally studied the variance of several operating characteristics of a HACHP using waste heat. The objective of the heat pump was to deliver hot water at temperatures over 90°C. For this, an Osenbruck cycle with two-stage compression, a rectifier and a desuperheater are used. Experimental studies were conducted to determine the influence of the ammonia-water mixture composition on the operation of the HACHP. The authors noted several advantages over conventional VCHP's like a large temperature glide, improved temperature lift, a flexible operating range and greater capacity control. The following experimental conclusions were drawn:

- The compressor discharge pressure increases as the ammonia concentration in the weak solution increased. This is due to higher saturation pressure of ammonia than water.
- Subsequently, the ammonia vapour mass flow rate and vapour density at the inlet of the compressor increased with the increase in concentration of ammonia in the weak solution.
- For the operating conditions in this study, the capacity of the entire system can be controlled by the ammonia concentration in the weak solution.
- The vapour mass quality and ammonia concentration in the strong solution at the inlet of the absorber increase with the increase in ammonia concentration in the weak solution. The ammonia vapour discharged from the compressor is mixed with the weak solution at the inlet of the absorber. The ammonia vapour mass flow rate is increased which further increases the vapour quality and concentration of the strong solution.
- The saturation pressure rises as the ammonia concentration in the weak solution is increased. This increases the compressor discharge vapour temperature. Ammonia is absorbed into water after mixing, which further increases the temperature of the strong solution.
- The temperature of the weak solution is increased by the IHEX and the intercooler. The temperature difference at the absorber and the heating capacity also increase on increasing the weak solution concentration. An increase in the temperature glide increases the concentration difference between weak and strong solution.
- However, as the solution gets stronger, the temperature profiles at the absorber and desorber are mismatched leading to a performance degradation - the heating COP decreases.

Jung et al. (2014) analyzed the thermal performance characteristics for ammonia-water plate bubble absorbers for an HACHP. These performance parameters were observed as functions of the absorber internal pressure, ammonia weak solution concentration and geometry of the plate heat exchanger

(absorber). A single stage compressor was used here. The authors concluded that the absorber capacity, COP, hot water outlet temperature and the heat transfer coefficient increase with increase in the absorber internal pressure and decrease with ammonia weak solution concentration. The internal pressure of the absorber has a greater impact on its capacity than the weak solution concentration. The maximum power and COP obtained are : 7.3 kW and 2.66 respectively at internal pressure of 1.85 bar, weak solution concentration of 49 wt%. At these conditions the hot water outlet temperature was found to be 80.7°C and maximum heat transfer coefficient of 1.91 kW/m^{2}K. The length aspect ratio *(L/D)* affects the heat transfer coefficient of the solution more significantly than the width aspect ratio *(W/D)*, where *D* is the gap distance of the plate heat exchanger.

Liu et al. (2018) uses an Osenbruck cycle to recover sensible heat from flue gas at temperatures around 150°C to generate saturated steam at certain conditions. An illustration of the heat pump utilized is shown in Figure 2.2. The sensible heat is put into a cascade system consisting of an absorption subsystem and a compression subsystem. First the flue gas is passed through the reboiler of the absorption subsystem and then through the evaporator of the compression subsystem. In this way the remainder of its low grade thermal energy is utilized. The high temperature waste heat is used to generate highly pure ammonia vapour in the rectifier and the lower temperature waste heat is used to evaporate the liquid ammonia. This unique system is then compared to a conventional CRHP system with a desorber and absorber. On analysing the exergy of the two systems, it was shown that this configuration has 4.69% higher exergy efficiency and lower power consumption (CRHP requiring 54.37% more). The compressor discharge temperature is also lower in the proposed system. The COP of the proposed system reaches 5.49, two times higher than the reference CRHP system. Economic analysis also showed that the proposed system has a payback period of 6.26 year.

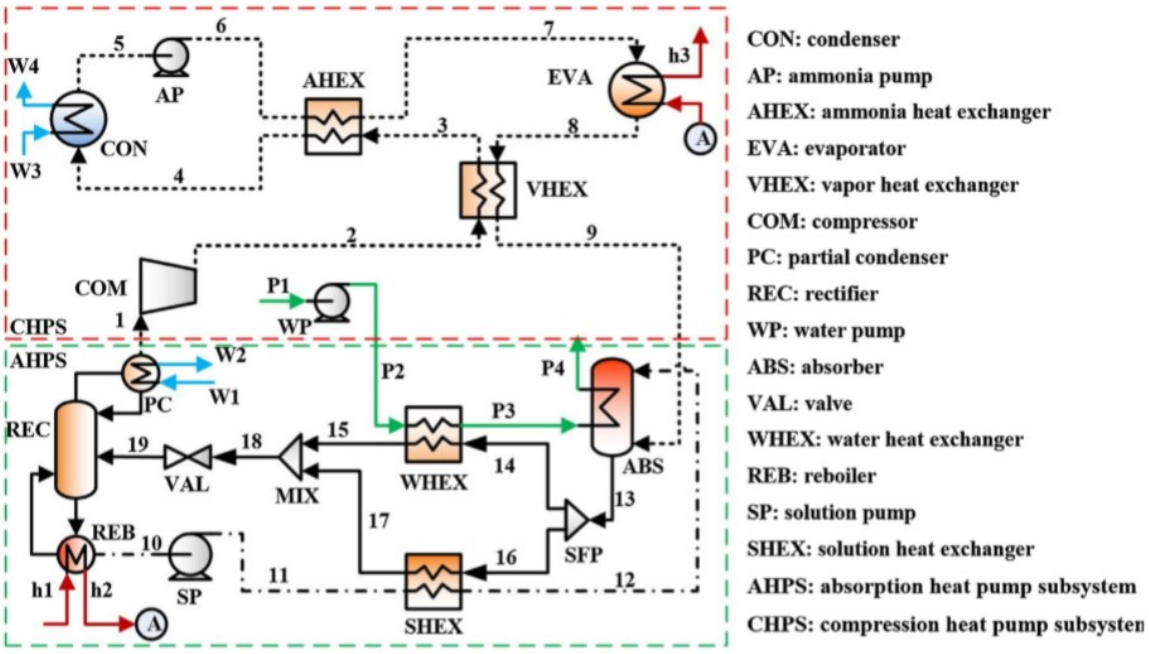

Figure 2.2: A schematic of a cascade hybrid ammonia-water absorption compression heat pump (Liu et al., 2018)

Table 2.1: Summary of Osenbruck cycle research

Author (year)	Working Fluid	Variables	Configuration	Major Conclusions
Kim et al. (2013)	Ammonia-Water	Ammonia concentration in the weak solution	Osenbruck Cycle with 2 stage compression, rectifier, desuperheater	Compressor discharge temperature increases with weak solution ammonia concentration
Jensen et al. (2015b)	Ammonia-Water	Mass fraction of ammonia, circulation ratio	Conventional Osenbruck cycle compared to VCHP	HACHP can deliver higher temperatures (up to 150°C) and higher temperature lifts (up to 60 K) than VCHPs. Economically better than NG burners
Jung et al. (2014)	Ammonia-Water	Absorber internal pressure, ammonia concentration in the weak solution, geometry of plate heat exchanger	Single stage compressor	The absorber heating capacity, COP, hot water outlet temperature and the heat transfer coefficient increase with increase in the absorber internal pressure and decrease with weak solution ammonia concentration
Jensen et al. (2015a)	Ammonia-Water	Mass fraction of ammonia, liquid circulation ratio (mass flow rate of the lean solution to that of the rich solution)	Osenbruck cycle with gas cooler	Major constraints for higher sink temperatures are high pressure, compressor discharge temperature and mass fraction of ammonia in the vapour.
Jung et al. (2018)	Ammonia-Water	Ammonia concentration in the weak solution	Osenbruck cycle with rectifier	As the weak solution ammonia concentration increases, COP increases, absorber heat transfer rate decreases
Liu et al. (2018)	Ammonia-Water	Mass fraction of ammonia-water, generation pressure, outlet temperature of condenser	Cascade system compared with conventional compression cycle	Proposed configuration has higher COP and exergy efficiency, lower compressor discharge temperature but higher payback period

2.1.2. Wet Compression

Wet compression can also be carried out in a CRHP, depending on the capability of the compressor. Since this is a two-phase compression process, it results in complexity. Itard (1998) has shown in her work under what conditions would wet compression be more favourable than dry compression in an Osenbruck cycle. This is done by comparing COP's of cycles using the two configurations - wet and dry compression - using different working fluids - pure refrigerants and mixtures. Her work shows that wet compression has few advantages when used with pure refrigerants. For a few refrigerants, a gain in COP can be seen. However, this gain is offset by the technological problems encountered. For non-zeotropic mixtures, wet compression leads to higher COP. However, this can also be offset if irreversibilities in the cycle are not kept in control and ideality is not approached, that is the isentropic efficiency of the compressor must be high enough.

van de Bor et al. (2015) also studied the effects of using wet and dry compression cycles while utilizing CRHPs. This work not only validated the conclusions already stated by Itard, that higher COPs are achieved with wet compression but also illustrated various shortcomings of dry compression. Lubrication is one such issue. In dry compression, outlet temperatures of the compressor can reach very high levels. In this case, oil may be needed inside the compressor as a lubricant. This can lead to further irreversibilities in the cycle. This lubricant may also accumulate in the heat exchangers, thereby reducing their effectiveness and efficiency. This will directly affect the overall performance of the heat pump. If wet compression is used, this problem can be surpassed since external lubrication is not required and superheating is also avoided.

Given below is Table 2.2 comparing the hybrid absorption compression heat pumps (HACHP) using the Osenbruck cycle and the compression resorption heat pumps (CRHP) using wet compression.

Table 2.2: Comparison of HACHP versus CRHP

Hybrid absorption compression heat pump	**Compression resorption heat pump**
Only the vapour undergoes compression. The liquid is recirculated via a solution pump (vapour phase compression).	Both the liquid and vapour undergo compression together (two phase compression).
Superheating of the vapour cannot be completely eliminated due to lubrication issues. This leads to very high compressor discharge temperatures affecting the performance. This can be solved using two-stage compression, oil-free compressor or a cooled screw compressor adding complexity.	Superheating can be eliminated since oil lubrication is not used in the process side. The process side is free of oil. This reduces the compressor discharge temperature to within allowable limits.
Widely studied hence less technologically challenging.	Not widely studied. Two phase compression adds complexity to the system. Irreversibilities must be kept small. Hence, a high isentropic efficiency is required for feasible operation.

2.2. Working Fluid Properties

Using a thermodynamic property database like the NIST database (REFPROP) developed by Lemmon et al. (2018), is a convenient way to determine essential values of various parameters.

Ammonia-water has been used as a working fluid for a long time. Its reliable, creates low noise and has good partial load behaviour (Ziegler and Trepp, 1984). The mixture can be used at high temperatures which makes it ideal for heat pumps. The concentration can control the temperature glide and can also be easily varied.

2.2.1. Ammonia-Water

The thermodynamic equilibrium properties of ammonia-water have been developed by Ziegler and Trepp (1984). They are an upgrade to the work done by Siegfried (1971), increasing the temperature range to 500 K and pressure range to 50 bar. According to the condition of phase equilibria:

$$T_\mathrm{L} = T_\mathrm{v} \tag{2.2}$$

$$p_\mathrm{L} = p_\mathrm{v} \tag{2.3}$$

$$\bar{\mu}_\mathrm{A,L} = \bar{\mu}_\mathrm{A,v} \tag{2.4}$$

$$\bar{\mu}_\mathrm{W,L} = \bar{\mu}_\mathrm{W,v} \tag{2.5}$$

The temperature, pressure and chemical potential of both phases are in equilibrium for all components. The Gibbs free energy of a liquid binary mixture is given in equations 2.6 and 2.7 (Zaytsev, 2003).

$$g_\mathrm{L} = (1 - \bar{w}_\mathrm{L})\bar{\mu}_\mathrm{W,L} + \bar{w}_\mathrm{L}\bar{\mu}_\mathrm{A,L} \tag{2.6}$$

$$\left(\frac{\partial g_\mathrm{L}}{\partial \bar{w}_\mathrm{L}}\right)_{p,T} = \bar{\mu}_\mathrm{A,L} - \bar{\mu}_\mathrm{W,L} \tag{2.7}$$

where $\bar{w}_\mathrm{L}$ is the liquid ammonia molar concentration. On solving equations 2.6 and 2.7 simultaneously, the chemical potentials of each component are obtained.

$$\bar{\mu}_\mathrm{A,L} = g_\mathrm{L} + (1 - \bar{w}_\mathrm{L})\left(\frac{\partial g_\mathrm{L}}{\partial \bar{w}_\mathrm{L}}\right)_{p,T} \tag{2.8}$$

$$\bar{\mu}_\mathrm{W,L} = g_\mathrm{L} - \bar{w}_\mathrm{L}\left(\frac{\partial g_\mathrm{L}}{\partial \bar{w}_\mathrm{L}}\right)_{p,T} \tag{2.9}$$

In the same way, the chemical potentials of each component in the gas phase can be obtained. Therefore, the system becomes:

$$T_\mathrm{L} = T_\mathrm{v} \tag{2.10}$$

$$p_\mathrm{L} = p_\mathrm{v} \tag{2.11}$$

$$g_\mathrm{L} - \bar{w}_\mathrm{L}\left(\frac{\partial g_\mathrm{L}}{\partial \bar{w}_\mathrm{L}}\right)_{p,T} = g_\mathrm{v} - \bar{w}_\mathrm{v}\left(\frac{\partial g_\mathrm{v}}{\partial \bar{w}_\mathrm{v}}\right)_{p,T} \tag{2.12}$$

Where the Gibbs energy of the liquid and gas phase can be found as functions of the phase pressure, temperature and molar concentration.

$$g_\mathrm{L} = f(p_\mathrm{L}, T_\mathrm{L}, \bar{w}_\mathrm{L}) \tag{2.13}$$

$$g_\mathrm{v} = f(p_\mathrm{v}, T_\mathrm{v}, \bar{w}_\mathrm{v}) \tag{2.14}$$

Now, using the Gibbs free energy we can find the equilibrium molar concentration in both phases and hence get other thermodynamic properties. Equation 2.15 gives the molar volume, equation 2.16 gives the molar entropy and equation 2.17 gives the molar enthalpy.

$$\bar{v} = \left(\frac{\partial g}{\partial p}\right)_{T,\bar{w}} \tag{2.15}$$

$$\bar{s} = \left(\frac{\partial g}{\partial T}\right)_{p,\bar{w}} \tag{2.16}$$

$$\bar{h} = -T^2 \left(\frac{\partial g}{\partial T}\right)_{p,\bar{w}} \tag{2.17}$$

These equations are applicable for both phases. Now the molar specific values are converted to the mass specific values. To do this, the molar specific values are divided by the molar mass of each phase which is given in equations 2.18 and 2.19.

$$M_{\mathrm{L}} = M_{\mathrm{A}}\bar{w}_{\mathrm{L}} + M_{\mathrm{W}}(1 - \bar{w}_{\mathrm{L}}) \tag{2.18}$$

$$M_{\mathrm{v}} = M_{\mathrm{A}}\bar{w}_{\mathrm{v}} + M_{\mathrm{W}}(1 - \bar{w}_{\mathrm{v}}) \tag{2.19}$$

Next, the vapour and liquid mass fractions are calculated from the known concentration of the mixture. When this is done, the specific entropy, enthalpy and volume of the mixture can be calculated.

2.2.2. Ammonia-Carbon Dioxide-Water

In order to implement ammonia-carbon dioxide-water into the compressor model, Gruijthuijsen (2019) generated tables using Aspen Plus. An interpolation scheme was used to calculate values in between the values already in the generated table. The same conservation equations will be used. They contain the partial derivatives of the specific volume and enthalpy. These partial derivatives are calculated at fixed ammonia and carbon dioxide concentration. In order to obtain these partial derivatives, two tables, one for specific volume and the other for specific enthalpy are needed for different pressure and temperature values. Another table for the entropy is needed to calculate the entropy production and to determine the isentropic efficiency of the compressor. This table is also generated for the same values of pressure and temperature as the previous table. The vapour quality is also of interest, primarily at the suction and discharge. Hence, it is directly looked up in Aspen.

2.3. Twin Screw Compressors

There are various types of compressors. The oil-free twin screw compressor is a better alternative than reciprocating compressors or conventional oil-injected screw compressors for ammonia-water compression. Reciprocating compressors are membrane or piston type machines. Operation costs are high since the lifetime of the membrane is short (Zaytsev, 2003). This compressor is not considered for a CRHP due to its high operating costs, small flow rate (0.3 to 45 m^3/h) and high investment costs (Zaytsev, 2003).

The twin screw compressor, as the name suggests, is a positive displacement compressor consisting of two parallel helical rotors. Positive displacement compressors have a positive reduction of gas volume within a closed space resulting in a rise in pressure. During the rotation of the rotors (male and female), the volume of the working cavity first increases from zero to a maximum value and then decreases back to zero. It performs essentially three operations: suction, compression and discharge simultaneously. The two rotors are: male and female. They mesh into each other. Usually the male rotor is driven by external work and drives the female. This compressor was developed in the 1930's to overcome surge phenomenon. Surge is a form of aerodynamic instability usually seen in axial or centrifugal compressors.

There are two types of twin screw compressors: oil-free and oil-injected. Conventional screw compressors with oil injection diminish the purity of the ammonia produced as the oil itself acts as the impurity. It might also develop other impurities such as hydrogen sulphide that causes deterioration of the lubricant (Tian et al., 2017). In the oil injected compressor, oil is used for lubrication, sealing and cooling. It does not contain any timing gears since oil permits a contact between the lobes and one rotor drives the other through the oil film. The oil free compressor utilizes timing gears between the driving and driven rotors without any physical contact between the lobes. In this compressor the working chamber is separated from the bearing chambers by sealings. Hence, no lubrication or impurity issues arise.

The compressor efficiency is a function of the internal compression ratio which in turn is dependent on the volume ratio. Efficiency is maximum if the internal compression is equal to the required duty. The volume efficiency does not fall drastically with increase in the pressure ratio. There isn't any void volume in screw compressors. Therefore, no void volume re-expansion which deteriorates the volume efficiency (Zaytsev, 2003).

Regarding wet compression, screw compressors are more tolerant to liquid carryover than conventional compressors. They do not have valves, nor thin blades that could be damaged by liquid. In 1990, wet compression was successfully shown with an air twin screw compressor using ammonia-water. The compressor ran smoother and with less noise due to the wet vapour. The only reported issue was the sealing of the compressor (Gudjonsdottir, 2020).

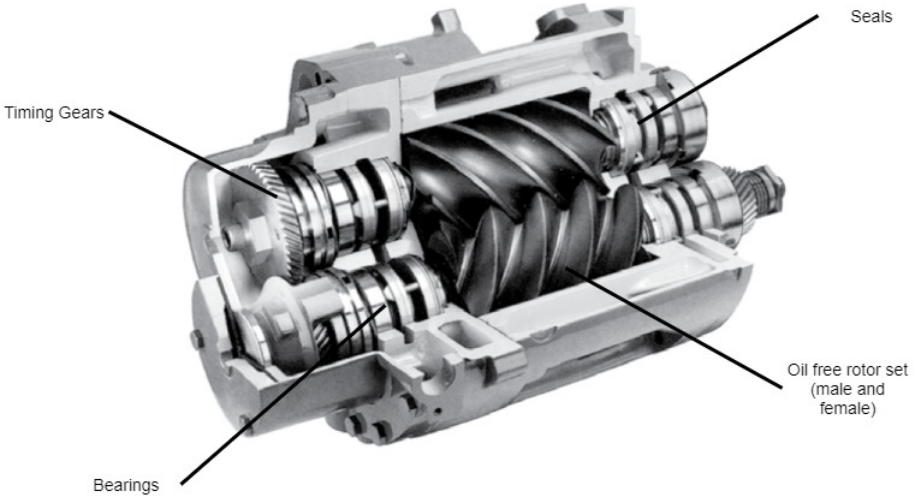

Figure 2.3: A half section of an oil-free twin screw compressor (Denver, 2020)

2.3.1. Experiments Done with Screw Compressors

In the past, various researchers have carried out a myriad of different but relevant model development along with experimental validation with screw compressors. It is also relevant to see which type of sensors these researchers have used. Some of the more pertinent research is mentioned in this section.

Tian et al. (2017) carried out an investigation on mass and heat transfer in an ammonia oil-free twin screw compressor with liquid injection for an ammonia refinery. A heterogeneous model was developed for this. The model used non-azeotropic mixture properties taking into account the evaporation effects during wet compression. This model was subsequently validated via experiments on a two-stage compression system. It was observed that liquid droplets will agglomerate through rotation and also be regenerated after collision making the size of the liquid droplets almost impossible to determine. In this paper, this agglomeration and regeneration are neglected in the compressor model. Tian et al. (2017) tested droplet diameters of less than 100 μm to achieve sufficient heat transfer. A pressure difference must be maintained within the injection nozzle to promote atomization via flashing. The isentropic efficiencies found for the two compressors were 75% and 64% respectively. They also recommend an injection nozzle after the start point of the compression process when there is maximum temperature glide. This will reduce the power consumption of the compressors. This new nozzle should have ca. 70% flow of the original nozzle at the suction port.

In this setup, Tian et al. (2017) used pressure gauges, thermometers and flow-meters. The pressure gauge is manufactured by Beijing Brightly (type YTN-100H) with a maximum range of 0 to 25 bar and an uncertainty of 1.5%. The temperature sensors are manufactured by Shanghai Hongda (type WSS-481Y) with a range of -40°C to 100°C. Unfortunately no information regarding the flow-meters used was provided.

Wang et al. (2018) later worked on the development of an oil-free twin-screw air compressor which is water lubricated for the production of high quality compressed air. Their research focused on an experimental study to assess the influence of various parameters like rotation speed, discharge pressure, water injection flowrate and water injection mode for power savings and improvements in efficiency. The rotation speed was varied from 2400 rpm to 5400 rpm. The discharge pressure was varied from 6 bar to 9 bar. The water is injected into the compressor at two locations: one to the bearings and shaft seals and the other to the rotor chamber. Two ports are drilled in the compressor casing to study the effects of injection positions. One is drilled at the bottom of the casing and faces the intersection of the two rotor holes and the other is at the middle section of the rotor chamber facing the two rotors. The compressor has a built-in volume ratio of 4.5. According to the results from the experiments, rotation speed affects the volumetric efficiency significantly. Volumetric efficiency increased with speed but the increment rate fell down. The efficiency increased by 16.5% from 2400 rpm to 5400 rpm. The leakage rates are almost constant at different speeds. Hence, the net mass of leakage would decrease with increasing speed due to shorter time for leakages. It is seen that till 3600 rpm the volumetric efficiency increased with discharge pressure. However, above 3600 rpm, the volumetric efficiency decreased with discharge pressure. Increasing the discharge pressure has two effects. One, it increases the pressure difference and thus increases the leakages. Two, it results in more water being injected into the compressor volume reducing the leakages. The first effect was dominant for speeds above 3600 rpm and the second was dominant when the speed was kept below 3600 rpm. The adiabatic efficiency trend was also observed. It first rises and then decreases with the rotation speed (above 4800 rpm). This decrease was attributed to greater impact of flow and friction losses. The specific power consumption first decreased sharply with the speed and then slowly. At speeds greater than 4800 rpm, the specific power was nearly constant. However, at 5400 rpm the specific power was slightly higher than at 4800 rpm. The final conclusions of the paper said that rotation speed should be relatively high for high efficiency since the compressor has low tip speed. They also observed that injecting a large amount of water directly in the compressor rather than using liquid-injection twin-screw compressors could also be feasible and effective.

Wang et al. (2018) used temperature, pressure, power and flowrate sensors for their research. They are tabulated in the table given below.

Table 2.3: Measurement instrumentation used by Wang et al. (2018)

Parameter	Measuring instrument	Range	Accuracy
Temperature	Pt100 (Class B)	0°C-100°C	±0.5%
Pressure	BP210	0-2.5 MPa	±0.1%
Volumetric flowrate	ASME nozzle flowmeter	1-2 m^3/min	±0.25%
Water flowrate	Vortex flowmeter	3-20 L/min	±0.5%

He et al. (2018) conducted an interesting investigation of oil-free twin-screw air compressor for a truck with a fuel cell system. They varied the rotation speed from 5000 rpm to 10000 rpm and discharge pressures from 1.4 bar to 2.2 bar to assess the performance of the compressor via parameters such as air flow rate, power consumption and discharge pressure. They saw that the pressures observed in the compression process are much lower than seen in the theoretical process. This is mainly due to leakages. Hence, clearances should be controlled. The flowrate increases almost linearly with rotation speed but decreases with discharge pressure (again due to increase of leakages). The volumetric efficiency also increases with rotation speed but the increment decreases. The volumetric efficiency decreases with discharge pressure. The power consumption of the compressor increases with rotation speed and discharge pressure as expected. Increasing the rotation speed increases the isentropic efficiency due to reduction in leakages (at the same discharge pressure). However, this curve tends to

flat out for higher speeds, even showing a reduction for lower pressures at 10000 rpm. This reduction in leakages is offset by the pressure losses generated due to air flow resistance at the suction and discharge of the compressor at higher speeds. Therefore there exists a peak point. The mechanical efficiency remains almost constant for 7000 rpm to 10000 rpm. The specific power consumption decreases for lower rotation speeds but is almost constant for higher speeds. No information regarding the measurement instrumentation was given.

2.4. Performance Models

Van de Bor and Infante Ferreira (2013) compared the performance of different heat pump cycles resulting in a performance map for the selection of heat pumps based on their energy efficiency and investment required. Heat pumps work best when the required temperature lift is minimized.

The Carnot efficiency of a heat pump is given in equation 2.20:

$$COP_{\text{Carnot}} = \frac{T_{\text{h}}}{T_{\text{h}} - T_{\text{l}}} \tag{2.20}$$

Where T_{h} is the sink temperature - that is, temperature of the hot utility - and T_{l} is the source temperature - that is, temperature of the cold utility or return stream from district heating network. Since we work with temperature glides in CRHP's, it is better to use the Lorentz COP than the Carnot COP. This Lorentz COP approximated by Yilmaz (2003) is given in equation 2.21:

$$COP_{\text{Lorentz}} = \frac{2T_{\text{h}} - \Delta T_{\text{h,glide}}}{2T_{\text{h}} - \Delta T_{\text{h,glide}} - 2T_{\text{l}} - \Delta T_{\text{l,glide}}} \tag{2.21}$$

Taking equal glides on both the sides, this equation is further simplified.

$$COP_{\text{Lorentz}} = \frac{2T_{\text{h}} - \Delta T_{\text{h,glide}}}{2\Delta T_{\text{lift}} - 2\Delta T_{\text{glide}}} \tag{2.22}$$

$$\Delta T_{\text{lift}} = T_{\text{h}} - T_{\text{l}} \tag{2.23}$$

The error introduced using the approximation by Yilmaz (2003) varies from 0% to 7%. Now we have:

$$\frac{COP_{\text{Lorentz}}}{COP_{\text{Carnot}}} = \frac{1}{1 - \frac{\Delta T_{\text{glide}}}{\Delta T_{\text{lift}}}} \tag{2.24}$$

From Equation 2.24 a graph can be derived illustrating the advantage of using temperature glides when compared to conventional cycles. In conventional cycles, this COP ratio will be 1. Hence, this shows that significant improvements in performance can be made using CRHP's. Furthermore, this paper shows the economic evaluation of different heat pumps considering thermodynamic losses like temperature driving force and isentropic losses. When the temperature driving force (TDF) is considered as 10% of the lift and taking glide as 50% to 75%, the payback period of the heat pump was found to be 3 years. CRHP's reduce the energy usage by 68% and energy costs by 72% which was almost double that of conventional VCHP's. The paper shows that for large temperature glides, CRHP's do have an advantage over other technologies.

Building on the same model, van de Bor et al. (2015) then compared different heat pumps and power cycles for low grade heat recovery applications. Here, the compressor was assumed to operate at 70% isentropic efficiency. Referring to Figure 1.2 (right), T_3 is the fixed waste water source temperature (for example 60°C) plus a 5 K driving force, T_1 is the fixed waste water source temperature minus a 5 K driving force. To ensure that this pinch temperature does not fall below 5 K, the desorber and resorber are divided into 100 control volumes. Inputs to the model are the ammonia concentration (w), the temperature of waste water stream and the temperature driving force.

$$T_3 = T_{\text{WW}} + TDF \tag{2.25}$$

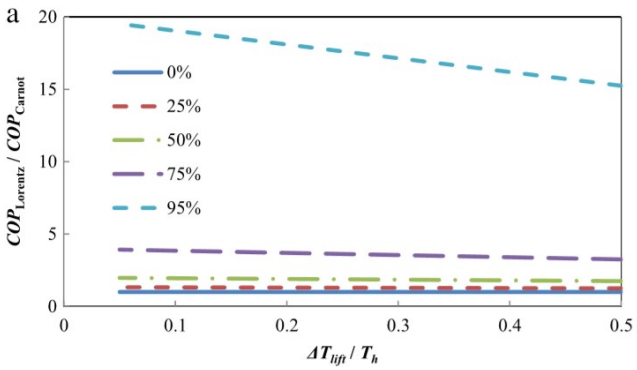

Figure 2.4: Ratio of Lorentz COP and Carnot COP as a function of dimensionless temperature lift. The graph shows different values of the glide to lift ratio.

$$T_1 = T_{WW} - TDF \tag{2.26}$$

For the wet compression cycle, a value of p_1 is initially assumed. From which h_1 and s_1 can be found. Assuming an ideal cycle, no entropy change will occur across the compressor. Hence, using the assumed efficiency of the compressor we can arrive at the actual enthalpy at the outlet. Subsequently, we can find the COP of the cycle:

$$h_1, s_1 = f(p_1, T_1) \tag{2.27}$$

$$s_1 = s_{2,is} \tag{2.28}$$

$$p_2, p_3, h_3, h_4 = f(T_3, q = 0) \tag{2.29}$$

$$h_{2,is} = f(p_3, s_{2,is}) \tag{2.30}$$

$$\eta_{is} = \frac{h_{2,is} - h_1}{h_2 - h_1} \tag{2.31}$$

$$COP = \frac{h_2 - h_3}{h_2 - h_1} \tag{2.32}$$

For the CRHP, the COP showed a decreasing trend with increasing ammonia concentration. An economic evaluation revealed that the maximum economic benefit was obtained from the CRHP and since the entire temperature glide can be used on both the resorber and desorber. Hence, the authors concluded that CRHP's work best in comparison for heating water from 60°C to values above 100°C.

Van De Bor et al. (2014) investigated the performance of CRHPs for high temperature lift situations in 50 industrial cases to shorten the payback period. Here, an equilibrium model was developed for the heat pump using ammonia-water as the working fluid. The industrial cases were primarily for distillation processes. Heat pumps can be used to upgrade the low quality energy in the condenser in order to drive the reboiler of the column and thus reduce the energy consumption. Inlet and outlet temperatures of the reboiler and condenser are used to calculate the efficiency of the heat pump without looking at the geometry of the compressor. Again, the ammonia concentration was varied. The TDF was assumed to be 5 K at the resorber outlet and desorber inlet. The vapour quality was varied at the resorber inlet. The equilibrium model has certain assumptions listed below:

- T_3, that is, resorber outlet temperature is 5 K higher than the process temperature
- Either T_4, that is, desorber inlet temperature is 5 K lower than the process outlet temperature and >5 K lower than process inlet temperature or vice versa
- Pressure losses are neglected in both the heat exchangers
- The isentropic efficiency of the compressor is assumed to be 70%
- Electric drive efficiency is 100%
- No heat loss to the surroundings

The vapour quality (q) is varied at the inlet of the resorber (state point 2) from 10% to 100% in increments of 1%. The ammonia concentration (w) is varied from 0.5% to 99.5% in steps of 0.5%. For lower temperature glides, this step size was reduced since the temperature glides in the heat exchangers are very sensitive to the composition of the working fluid. Assuming the resorber outlet (state point 3) to be saturated liquid, the higher pressure and resorber inlet conditions are determined.

$$p_3 = p_2 = f(T_3, q = 0, \bar{w}) \tag{2.33}$$

$$T_2 = f(p_2, q_2, \bar{w}) \tag{2.34}$$

$$h_2 = f(p_2, q_2, \bar{w}) \tag{2.35}$$

$$h_3 = f(p_3, q = 0, \bar{w}) \tag{2.36}$$

$$h_4 = h_3 \tag{2.37}$$

Now that we have our basic properties, we can choose from two routes depending on the temperature glides (process side) at the heat exchangers.

Route 1: Temperature glide at resorber > Temperature glide at desorber

The desorber pressure is obtained from which the enthalpy at the outlet is found as a function of the pressure and entropy. The desorber inlet temperature (state point 4) is taken 5 K lower than the process conditions.

$$p_1 = p_4 = f(T_4, h_{\text{desorber}}, \bar{w}) \tag{2.38}$$

We know that the entropy at the outlet of the compressor for the theoretical case of 100% isentropic efficiency should be the same as the inlet entropy. This is used as an starting point to determine the desorber outlet conditions (state point 1).

$$h_{1,\text{ initial}} = f(p_1, s_{1,\text{ initial}}, \bar{w}) \tag{2.39}$$

Iterations are carried out until the value of the enthalpy at desorber outlet converges from the following equations:

$$h_1 = \frac{h_{2,\text{is}} - \eta_{is}\, h_2}{1 - \eta_{\text{is}}} \tag{2.40}$$

$$h_1 = f(p_1, s_1, \bar{w}) \tag{2.41}$$

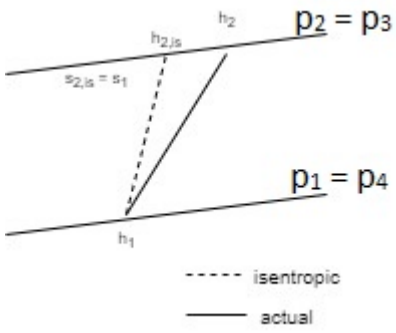

Figure 2.5: Method used to calculate the desorber outlet enthalpy

Now the temperature at the outlet of the desorber can be determined.

$$T_1 = f(p_1, h_1, \bar{w}) \tag{2.42}$$

If this temperature is greater than the process temperature minus 5 K, the corresponding ammonia concentration is discarded. Alternatively the TDF at inlet of the desorber could be increased.

Route 2: Temperature glide at resorber < Temperature glide at desorber

First the temperature at the desorber outlet is taken as the process temperature minus the TDF (5 K). The entropy is also assumed at this point in the cycle. This entropy is equal to the isentropic entropy at the compressor outlet.

$$T_1 = T_{\text{process}} - 5K \tag{2.43}$$

$$s_1 = s_{2,\text{is}} \tag{2.44}$$

An initial value of enthalpy for the desorber outlet is used to start the iterations using the same equations 2.40 and 2.41 used in route 1 .

$$h_{1,\text{ initial}} = f(T_1, s_{1,\text{ initial}}, \bar{w}) \tag{2.45}$$

Now we get the converged value for the enthalpy and pressure:

$$h_1 = f(T_1, s_1, \bar{w}) \tag{2.46}$$

$$p_1 = p_4 = f(T_1.s_1, \bar{w}) \tag{2.47}$$

Now the temperature at the inlet of the desorber can be determined.

$$T_4 = f(p_4, h_4, \bar{w}) \tag{2.48}$$

Van der Bor showed that optimal performance is obtained when saturated vapour (q = 1) enters the resorber. This leads to less energy input required by the compressor. Therefore investment and operating costs are reduced. This results in shorter payback periods. This paper also shows that CRHPs deliver economic advantages for temperature lifts up to 124 K. Optimum results are obtained when the glide of the process is matched by the glide of the resorber. The temperature glide of the desorber plays a less influential role. At higher resorber outlet temperatures, low ammonia concentrations are favourable and vice versa. The optimal ammonia concentration is dependent on the operating temperature of the resorber which determines the operating pressure of the resorber which in turn influences the temperature glide. This dependency is larger in cases where higher ammonia concentrations are used.

2.5. Compressor Models

It is already known that unless the isentropic efficiency of a compressor using wet compression is greater than 70%, there is no clear advantage over vapour compression heat pumps. Many people have previously worked on this project developing compressor models. In this section, their contributions are reviewed in brief.

Zaytsev (2003) developed a complete wet compression model, including a geometry part and a thermodynamic part. In this research it was also determined that screw compressors are most suitable for wet compression since they are can not only tolerate liquid carry over but also have a high efficiency. This model requires a detailed description of the geometry of the screw compressor increasing its complexity. Wet compression can be implemented in two ways: with or without liquid injection. With liquid injection, the liquid needs to be first cooled by additional heat exchangers so that the refrigerant does not flash into the compressor. Also, the concentration of ammonia changes when liquid is injected. Without liquid injection, the two phase mixture is directly compressed. The concentration of ammonia remains constant. Zaytsev (2003) performed experiments with wet compression in a twin screw compressor with liquid injection, however could not reach higher efficiencies.

Gudjonsdottir (2020) then further developed Zaytsev's compressor model for a new compressor prototype using wet compression with ammonia-water. This new compressor prototype is used for experimentation in this study. Liquid injection is no longer considered, hence the concentration of ammonia is taken as a constant in the mass and energy balance. This prototype also utilizes timing gears, hence friction losses between the rotors are not considered. A labyrinth seal, between the suction and discharge side of the compressor, was the major cause of leakage in Zaytsev's model. No such seal is

present in the new compressor. Gudjonsdottir's model had a long computational time because of which Guðmundsdóttir (2018) developed a simplified model to predict the performance without compromising accuracy, but in a quicker and more efficient manner.

Gruijthuijsen (2019) later developed a compressor model, building on Guðmundsdóttir's work, to increase the performance of the compressor using an ammonia-carbon dioxide-water mixture. This model was developed to predict the performance characteristics of the compressor for different CO_2 concentrations and comparing it with no CO_2 addition.

2.5.1. Detailed Model

Zaytsev (2003) proposed a compressor geometry model for an oil-free two phase twin-screw compressor using ammonia-water as an input to the thermodynamic simulation model. The thermodynamic part of the model is built on the conservation laws for a control volume and the equations of state. The characteristics of the screw compressor geometry required are the compressor cavity, volume, leakage path areas, suction and discharge port areas and position of injection ports (if liquid is injected). All these parameters can be described as a function of the rotation angle of the male rotor. The geometry model along with the performance model can be used to determine parameters of the compressor such as various efficiencies, flow rate and compression power. A homogenous *pT* model is used here with the underlying assumption that the vapour and liquid are in equilibrium. From this the conservation equations 2.49, 2.50 and 2.51 arise for the working mixture inside a control volume *V*.

The conservation of mixture mass:

$$dm = \sum_{i=1}^{l} dm_{\text{in,i}} - \sum_{i=1}^{n} dm_{\text{out,i}} \tag{2.49}$$

The conservation of ammonia mass:

$$d(mw) = \sum_{i=1}^{l} w_{\text{in,i}} dm_{\text{in,i}} - w \sum_{i=1}^{n} dm_{\text{out,i}} \tag{2.50}$$

The conservation of energy:

$$\delta Q + \sum_{i=1}^{l} h_{\text{in,i}} dm_{\text{in,i}} - h \sum_{i=1}^{n} dm_{\text{out,i}} = dH - Vdp \tag{2.51}$$

The specific volume *v* is a function of pressure, temperature and the mass concentration of ammonia in the mixture *w*. It is defined as the mass of ammonia contained in one kg of the mixture. Solving the above equations for pressure, mass concentration of ammonia and temperature as a function of the male rotor angle leads to the governing equations of 2.52, 2.53 and 2.54.

On solving the mixture mass conservation equation 2.49, we get the governing mass conservation equation 2.52.

$$\frac{dp}{d\varphi} = \frac{1}{\left(\frac{\partial v}{\partial p}\right)_{T,w}} \left[\frac{v}{m} \left(\sum_{i=1}^{n} \left(\frac{dm_{\text{out}}}{d\varphi} \right)_i - \sum_{i=1}^{l} \left(\frac{dm_{\text{in}}}{d\varphi} \right)_i \right) + \frac{1}{m} \frac{dV}{d\varphi} - \left(\frac{\partial v}{\partial T} \right)_{p,x} \frac{dT}{d\varphi} - \left(\frac{\partial v}{\partial w} \right)_{p,T} \frac{dw}{d\varphi} \right] \tag{2.52}$$

Differentiating -by the shaft rotation angle φ- and solving the ammonia mass conservation equation 2.50 we get the ammonia concentration in the control volume.

$$\frac{dw}{d\varphi} = \frac{1}{m} \left[\sum_{i=1}^{l} w_{\text{in,i}} \left(\frac{dm_{\text{in}}}{d\varphi} \right)_i - w \sum_{i=1}^{l} \left(\frac{dm_{\text{in}}}{d\varphi} \right)_i \right] \tag{2.53}$$

When the compressor operates without liquid injection and the mass concentration of ammonia in the suction flow remains constant, the concentration inside the compressor cavity will remain constant. However, when liquid injection is used, this concentration will vary since the concentration of ammonia in the injection is generally not the the same as in the main flow (Zaytsev, 2003).

Solving the energy conservation equation 2.51, we obtain an expression for the derivative of the temperature by the shaft rotation angle in 2.54.

$$\frac{dT}{d\varphi} = \frac{T\left(\frac{\partial v}{\partial T}\right)_{p,w}\left[\frac{v}{m}\left(\sum_{i=1}^{n}\left(\frac{dm_{\text{out}}}{d\varphi}\right)_i - \sum_{i=1}^{l}\left(\frac{dm_{\text{in}}}{d\varphi}\right)_i\right) + \frac{1}{m}\frac{dV}{d\varphi} - \left(\frac{\partial v}{\partial w}\right)_{p,T}\frac{dw}{d\varphi}\right]}{\left(\frac{\partial v}{\partial p}\right)_{T,w}\left(\frac{\partial h}{\partial T}\right)_{p,w} + T\left(\frac{\partial v}{\partial T}\right)^2_{p,w}} + \frac{\frac{\delta Q}{d\varphi} + \sum_{i=1}^{l}(h_{\text{in,i}} - h)\left(\frac{dm_{\text{in}}}{d\varphi}\right)_i - m\left(\frac{\partial h}{\partial w}\right)_{p,T}\frac{dw}{d\varphi}}{m\left(\frac{\partial h}{\partial T}\right)_{p,w} + \frac{mT}{\left(\frac{\partial v}{\partial P}\right)_{T,w}}\left(\frac{\partial v}{\partial T}\right)^2_{p,w}} \tag{2.54}$$

By numerical integration of these equations we can get the pressure, temperature and overall concentration of the ammonia-water mixture. Hence, the thermodynamic state of the mixture within the control volume can be defined. Subsequently, other thermodynamic parameters can be obtained using a property database.

2.5.2. Simplified Model

Guðmundsdóttir (2018) simplified the detailed model by Zaytsev (2003) by not considering liquid injection. Hence, the concentration of ammonia remains constant and the derivations of *w* can be neglected. Hence, equation 2.53 can be neglected. The remaining governing equations are also simplified.

The conservation of mass:

$$\frac{dp}{d\varphi} = \frac{1}{\left(\frac{\partial v}{\partial p}\right)_{T,w}}\left[\frac{v}{m}\left(\sum_{i=1}^{n}\left(\frac{dm_{\text{out}}}{d\varphi}\right)_i - \sum_{i=1}^{l}\left(\frac{dm_{\text{in}}}{d\varphi}\right)_i\right) + \frac{1}{m}\frac{dV}{d\varphi} - \left(\frac{\partial v}{\partial T}\right)_{p,w}\frac{dT}{d\varphi}\right] \tag{2.55}$$

The conservation of energy:

$$\frac{dT}{d\varphi} = \frac{T\left(\frac{\partial v}{\partial T}\right)_{p,w}\left[\frac{v}{m}\left(\sum_{i=1}^{n}\left(\frac{dm_{\text{out}}}{d\varphi}\right)_i - \sum_{i=1}^{l}\left(\frac{dm_{\text{in}}}{d\varphi}\right)_i\right) + \frac{1}{m}\frac{dV}{d\varphi}\right]}{\left(\frac{\partial v}{\partial p}\right)_{T,w}\left(\frac{\partial h}{\partial T}\right)_{p,w} + T\left(\frac{\partial v}{\partial T}\right)^2_{p,w}} + \frac{\frac{\partial Q}{\partial \varphi} + \sum_{i=1}^{l}(h_{\text{in,i}} - h)\left(\frac{dm_{\text{in}}}{d\varphi}\right)_i}{m\left(\frac{\partial h}{\partial T}\right)_{p,w} + \frac{mT}{\left(\frac{\partial v}{\partial P}\right)_{T,w}}\left(\frac{\partial v}{\partial T}\right)^2_{p,w}} \tag{2.56}$$

Guðmundsdóttir (2018) has determined that the most suitable approach for the model implementation would be to merge certain aspects of Zaytsev's model with the model developed by Chamoun et al. (2013). This model takes into account liquid injection. However, this part of the model by Chamoun et al. (2013) will be left out as here there is no liquid injection. It is based on the following assumptions:

- Constant inlet velocity and no pressure drop during the suction process
- Pressure and enthalpy are homogeneous throughout the working space at any given instant
- Pressure pulsations in the suction and discharge port are neglected

The model by Chamoun et al. (2013) eventually solves the mass and energy balance given in equation 2.57 and 2.58

$$a\frac{\Delta p}{\Delta \varphi} + b\frac{\Delta h}{\Delta \varphi} + c\frac{\Delta V}{\Delta \varphi} = \dot{m}_{\text{l,in}} - \dot{m}_{\text{l,out}} \tag{2.57}$$

$$d\frac{\Delta p}{\Delta \varphi} + e\frac{\Delta h}{\Delta \varphi} + f\frac{\Delta V}{\Delta \varphi} = \dot{m}_{\text{l,in}} h_{\text{l,in}} - \dot{m}_{\text{l,out}} h_{\text{l,out}} + \dot{Q}_{\text{in}} \tag{2.58}$$

Where the coefficients are shown in equations 2.59 and 2.60

$$a = V\left(\frac{\partial \rho}{\partial p}\right)_h \omega \quad b = V\left(\frac{\partial \rho}{\partial h}\right)_p \omega \quad c = \rho\omega \tag{2.59}$$

$$d = V\left(\left(\frac{\partial \rho}{\partial p}\right)_h - 1\right)\omega \quad e = V\left(\rho + h\left(\frac{\partial \rho}{\partial h}\right)_p\right)\omega \quad f = (h\rho)\omega \tag{2.60}$$

Since Zaytsev's model uses less assumptions than Chamoun et al. (2013) and its efficiency equations are more relevant to the conservation equations used, Guðmundsdóttir (2018) uses the efficiency equations from Zaytsev (2003). The indicated power and isentropic power are defined as shown in equations 2.61 and 2.62.

$$\dot{W}_{\text{ind}} = z_1 \frac{n}{60} \int p dV \tag{2.61}$$

$$\dot{W}_{\text{is}} = \dot{m}(h_{\text{is}} - h_{\text{suc}}) \tag{2.62}$$

The shaft power is the total power that affects the process. Friction exists in the bearings, seals and between the two rotors. However, the compressor in study uses timing gears, hence this factor can be neglected.

$$\dot{W}_{\text{s}} = \dot{W}_{\text{ind}} + \dot{W}_{\text{f,comp}} + \dot{W}_{\text{f,se}} + \dot{W}_{\text{f,be}} \tag{2.63}$$

Where the friction in the bearings and seals can be given by equations 2.64 and 2.65 respectively. Here μ is the coefficient of friction.

$$\dot{W}_{\text{f,be}} = r\omega\mu F_{\text{be}} \tag{2.64}$$

$$\dot{W}_{\text{f,se}} = 2\pi r^2 \omega\mu(w_{\text{e}} + \delta\Delta p) \tag{2.65}$$

Now the efficiencies can be defined as shown in equations 2.66, 2.67 and 2.68. Chamoun et al. (2013) as well as Tang (1995) assumed a mechanical efficiency of 90%.

$$\eta_{\text{is,comp}} = \frac{\dot{W}_{\text{is}}}{\dot{W}_{\text{ind}}} \tag{2.66}$$

$$\eta_{\text{is,inst}} = \frac{\dot{W}_{\text{is}}}{\dot{W}_{\text{s}}} \tag{2.67}$$

$$\eta_{\text{vol}} = \frac{v_{\text{suc}} \int \frac{dm}{d\varphi} d\varphi}{V_{\text{max}}} \tag{2.68}$$

A rough estimate of the volume curve, leakage paths and the port areas is enough. Guðmundsdóttir (2018) references the graphs constructed by Tang (1995) for the leakage paths in the compressor at different rotational degrees.

Guðmundsdóttir (2018) first starts the simulation with an initial cycle without leakage consisting of the conservation equations (Equations 2.55 and 2.56) and the thermodynamic properties. After this has been done, the base values for the entire compression process are available and can be used. The leakages flow from the discharge end towards the suction end due to pressure differences between the cavities. It flows from high pressure to low pressure through the corresponding leakage path depending on where in the compressor it is flowing.

2.5.3. Heterogeneous Model

Tian et al. (2017) developed a heterogeneous model to study the various characteristics of an ammonia-water twin screw compressor with liquid injection in an ammonia refinery. In this model, they use a mass diffusion equation along with the thermodynamic and physical property database which was developed and then validated using REFPROP (Lemmon et al., 2018). They observe the effect of liquid injection to the compressor power consumption and predict the temperature glide. Subsequently the research recommends an optimization method. Previous models discussed above, all assume a homogeneous nature of mixing between ammonia-water. In this section, a brief overview is given into how a possible heterogeneous thermodynamic model can be developed.

The schematic of the ammonia refinery is shown in Figure 2.6. Superheated ammonia vapour with a concentration of 98% is mixed with saturated ammonia solution just before suction of compressor I. Supplement ammonia solution (40%) is injected into this compression mixture. This mixture is then cooled down in after-cooler I before the gas-liquid separator I. The gas is then sucked to the second stage compressor. The second stage cycle is similar to the first stage cycle with the exception of supplement liquid injection. The drainage is sent to an ammonia course distillation tower. At the end of both stages, high pressure ammonia at concentrations higher than 99.6% is produced.

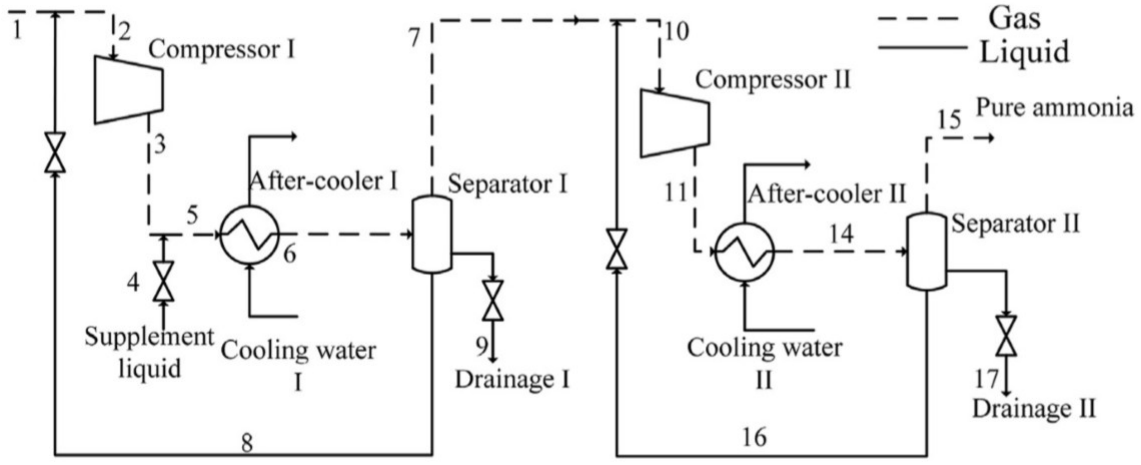

Figure 2.6: Schematic of the ammonia refinery developed to increase the concentration of ammonia from 98% to 99.6% Tian et al. (2017)

To solve the mass diffusion equation, several thermal and physical properties are required. The dew and bubble point temperatures (as a function of pressure and mole fraction), the mass diffusion coefficient, the surface tension and the dynamic viscosity are taken from literature. The specific volume, enthalpy and entropy are calculated using the Gibbs energy function.

The energy balance across the compressor can be expressed as in equation 2.69.

$$\dot{m}_{\text{suc}} h_{\text{suc}} + \dot{W}_s = \dot{m}_{\text{dis}} h_{\text{dis}} + \dot{W}_{\text{lub}} \tag{2.69}$$

Here, $\dot{W}_{\text{lub}}$ is the heat carried away by the bearing lubricant. To simplify the heat transfer, it is assumed that all the heat released by the compressor is taken away by the bearing lubricant. The compression process is discretized into several independent compression elements, each with a constant pressure step. These elements are sequential, that is, the discharge of one element is the suction of the element succeeding it and so on. In each compression element, the liquid and vapour components are treated as independent entities and compressed individually. The heterogeneous compression model is based on the concentration and energy balance equations and considers mass diffusion. Here, $\bar{w}_{\text{L}}$ is the molar fraction of ammonia in the ammonia-water liquid mixture and $\bar{w}_{\text{V}}$ is the molar fraction of ammonia in the ammonia-water vapour mixture. The heterogeneous model can be represented by the

set of equations given in 2.70-2.77 for the i^{th} compression element.

$$\dot{m}^{\mathsf{L}}_{\text{out,i}} = \dot{m}^{\mathsf{L}}_{\text{in,i}} - \Delta\dot{m}_{\text{evap,i}} \tag{2.70}$$

$$\dot{m}^{\mathsf{v}}_{\text{out,i}} = \dot{m}^{\mathsf{v}}_{\text{in,i}} + \Delta\dot{m}_{\text{evap,i}} \tag{2.71}$$

$$\dot{m}^{\mathsf{L}}_{\text{out,i}}\bar{w}_{\text{L,out,i}} = \dot{m}^{\mathsf{L}}_{\text{in,i}}\bar{w}_{\text{L,in,i}} - \Delta\dot{m}_{\text{evap,i}}\bar{w}_{\text{evap,i}} \tag{2.72}$$

$$\dot{m}^{\mathsf{v}}_{\text{out,i}}\bar{w}_{\text{v,out,i}} = \dot{m}^{\mathsf{v}}_{\text{in,i}}\bar{w}_{\text{v,in,i}} + \Delta\dot{m}_{\text{evap,i}}\bar{w}_{\text{evap,i}} \tag{2.73}$$

$$h^{\mathsf{L}}_{\text{out,i}} = h^{\mathsf{L}}(T^{\mathsf{L}}_{\text{out,i}}, p_{\text{out,i}}, \bar{w}_{\text{L,out,i}}) \tag{2.74}$$

$$h^{\mathsf{v}}_{\text{out,i}} = h^{\mathsf{v}}(T^{\mathsf{v}}_{\text{out,i}}, p_{\text{out,i}}, \bar{w}_{\text{v,out,i}}) \tag{2.75}$$

$$\dot{m}^{\mathsf{L}}_{\text{out,i}}h^{\mathsf{L}}_{\text{out,i}} + \dot{m}^{\mathsf{v}}_{\text{out,i}}h^{\mathsf{v}}_{\text{out,i}} + \dot{W}_{\text{lub}} = \dot{m}^{\mathsf{L}}_{\text{in,i}}h^{\mathsf{L}}_{\text{in,i}} + \dot{m}^{\mathsf{v}}_{\text{in,i}}h^{\mathsf{v}}_{\text{in,i}} + \dot{W}_{\text{s}} \tag{2.76}$$

$$\Delta T_{\text{out,i}} = T^{\mathsf{v}}_{\text{out,i}} - T^{\mathsf{L}}_{\text{out,i}} \tag{2.77}$$

Here, $\Delta T_{\text{out,i}}$ refers to the temperature difference between the two phases and $\Delta m_{\text{e,i}}$ is the evaporated mass flowrate.

2.6. Conclusion

In this chapter, a detailed literature review about the background of compression resorption heat pumps is provided. This chapter has outlined various concepts like HACHP and CRHP cycles, wet versus dry compression, property models for ammonia-water, screw compressors and its performance. Heat pumps can undergo dry or wet compression. The Osenbruck cycle is employed when dry compression is used. CRHP's with wet compression have a higher COP but this can be offset due to the technological challenges and irreversibilities in the system. An oil-free twin screw compressor is not only a better alternative to other types of compressors but also more suited for wet compression. Researchers have carried out various experiments to study screw compressors with different configurations and setups. Their results are seen as an expected trend for this thesis however the different configurations and operating conditions have to be taken into account. Performance models and compressor models have been developed which will be used in this thesis as well.

In this research, a homogenous compressor model will be used. This model was first developed by Zaytsev (2003) and Guðmundsdóttir (2018) later simplified the model to reduce computational time. Guðmundsdóttir merged Zatysev's detailed compressor model with the model developed by Chamoun et al. (2013) to get a simplified compressor model since a detailed geometry of the compressor is unavailable. Liquid injection has been left out from Zatysev's model since liquid is injected into the vapour stream before suction in the setup used. A brief understanding of a heterogeneous model is also developed. In this model, the liquid and vapour are not in equilibrium. A fraction of the liquid evaporates in the compressor changing the concentration of the solution at the discharge. This heterogeneous model is used as an alternate form of describing the experimental performance of the twin-screw compressor.

After achieving an understanding of the operation and performance of a CRHP, an experimental plan is developed and carried out. Over a range of ammonia concentrations, rotational speeds and vapour qualities, the performance of oil-free twin screw compressor is investigated further in the coming chapters. The results from this experimental study are subsequently used to validate the compressor model developed by Guðmundsdóttir (2018).

3

Experimentation

Only with industry and persistent efforts do the works get accomplished, not merely by wishing. The deer does not enter a lion's mouth on its own, without him going for the hunt.

Hitopadesha

In this chapter, the entire experimentation procedure shown in Figure 1.5 is discussed in detail. First, an overview of the entire experimental setup at the Process and Energy Laboratory at TU Delft is given. Preparing the setup for experimentation is needed since new temperature sensors at the compressor suction and discharge were added. Then the experimental plan is presented. After each experimental run, the data is compiled, processed and evaluated. The experimental results are shown and discussed in section 3.5 and 3.7.

3.1. Experimental Setup

Figure 3.1 is the process and instrumentation diagram of the experimental setup. A twin-screw compressor manufactured by Atlas Copco is used in this experimental setup. The compressor operates oil-free on the process side. The compressor is run by an electric motor manufactured by Siemens. Synchronisation gears drive the two rotors. The gearbox and the bearing house are oil lubricated. This oil is cooled by cooling water in a plate heat exchanger. Table 3.1 lists the known geometrical characteristics of the screw compressor.

The compressed binary mixture of ammonia-water passes through two plate heat exchangers (absorber) in series where partial absorption takes place. The flow is then separated in the separator. This is done mainly to control and accurately measure the vapour quality at the inlet of the compressor. By separating the liquid flow from the vapour flow, we can control the amount of liquid and vapour via control valves. The vapour flow leaves from the top of the separator while the liquid flow leaves from the bottom. Electric tracing provides additional heat to the vapour flow making it slightly superheated. This not only ensures accurate flow readings but also prevents condensation of the vapour after leaving the separator. Coriolis flow sensors measure the flow in the liquid and the vapour lines. The liquid flow is subcooled by approximately 10 K to protect the electronics of the flow sensor. The flows are expanded as they pass through the control valves. Near the inlet of the compressor, the liquid is injected into the vapour flow through a spray nozzle. Pressure sensor P-401 is between the control valve and the nozzle. The pressure here is slightly higher than the suction pressure (P-403). The state point 1 refers to the inlet of the compressor. State point 2 refers to the outlet of the compressor.

Table 3.1: Geometrical Characteristics of the Twin Screw Compressor at TU Delft

Maximum Volume per Cavity (V_{max})	5.72 x 10^{-5}	m^3
Length of the rotors (L)	0.0840	m
Male Rotor Diameter (D_1)	0.0500	m
Rotational Speed of the male rotor	10320-15550	rpm
Number of lobes on the male rotor (z_1)	4	
Number of lobes on the female rotor (z_2)	6	
Clearance (C)	0.050	mm

3.1.1. Sensors and Accuracy

Various sensors are used in this setup for temperature, pressure and flow measurement at different locations. Table 3.2 lists the type, range and accuracy of these sensors. The ammonia-water side mass flows are measured by Coriolis mass flow meters from Bronkhorst while the water volume flows have been measured with electromagnetic flow sensors from Siemens. Temperatures have been measured with PT-100 sensors which have been calibrated and showed an accuracy of ±0.06 K in the temperature range 20°to 180°C.

Table 3.2: Accuracy of sensors used in the experimental setup

Sensor Type	**Range**	**Accuracy**	**Unit**
PT-100, Type A, temperature sensors [T]	+20 to +180	±0.06	°C
Bronkhorst RHM12 Rheonik Coriolis vapour mass flow meter [$\dot{m}_v$]	30 to 200	±0.75 %	kg/h
Bronkhorst IP-65 Coriolis liquid mass flow meter [$\dot{m}_L$]	1.5 to 75	±0.5 %	kg/h
Siemens Sitrans P DS III, P410, pressure sensors [p]	-1 to 16	±1.348%	barg
Siemens SITRANS F M MAG 5000, volume flow sensors [$\dot{m}_{cw,sub}, \dot{m}_{cw,oil}$]	0 to 300	0.5%	l/h
Siemens SITRANS F M MAG 5000, volume flow sensors [$\dot{m}_{cw,abs}$]	0 to 900	0.5 %	l/h
Siemens, electric power consumption [$\dot{W}_{elec}$]	0 to 75	0.5	kW

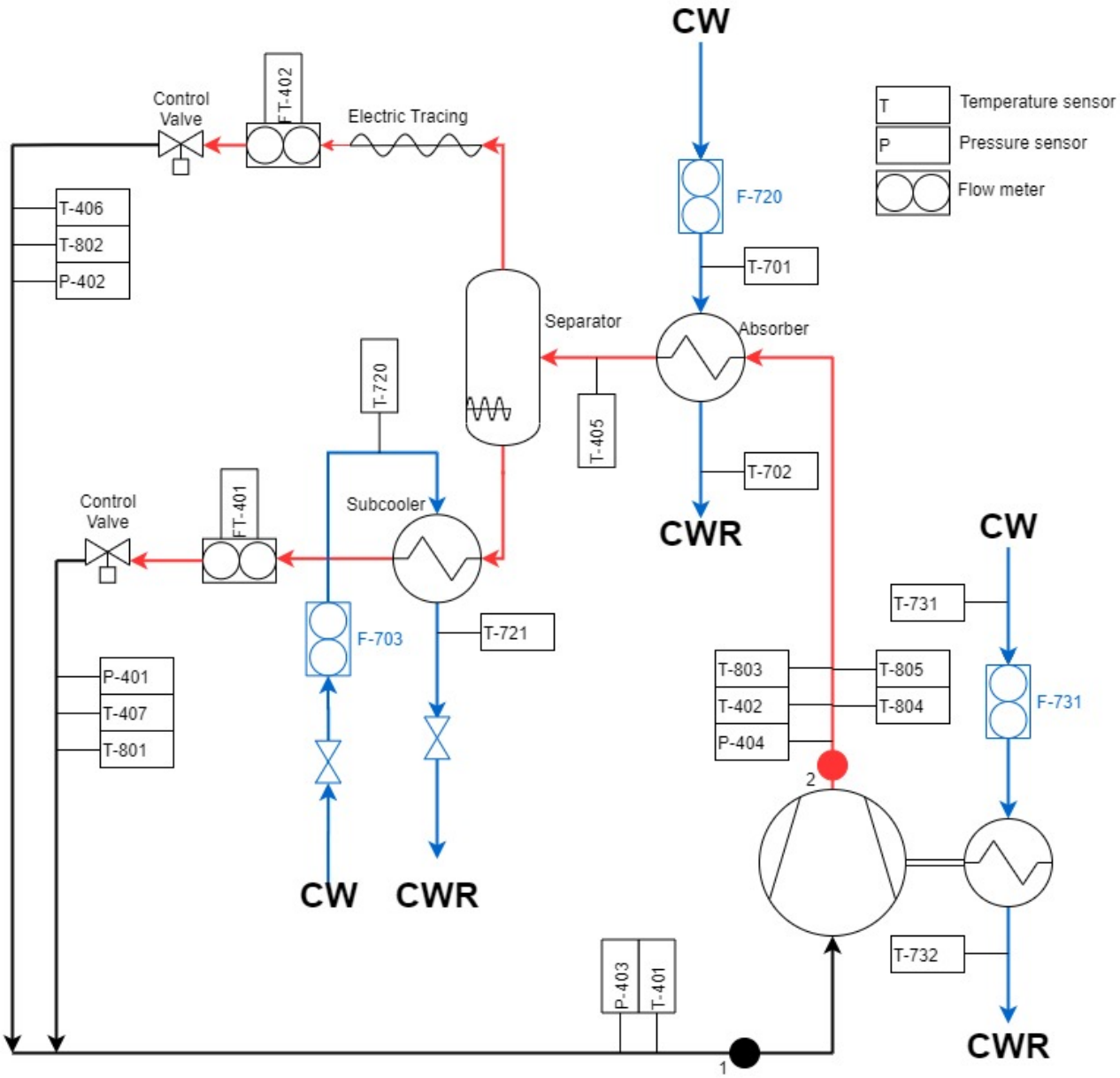

Figure 3.1: Process and Instrumentation Diagram of the experimental set-up at TU Delft. The blue lines represent the cooling water lines. The red line represent the high pressure side and black line represent the low pressure side.

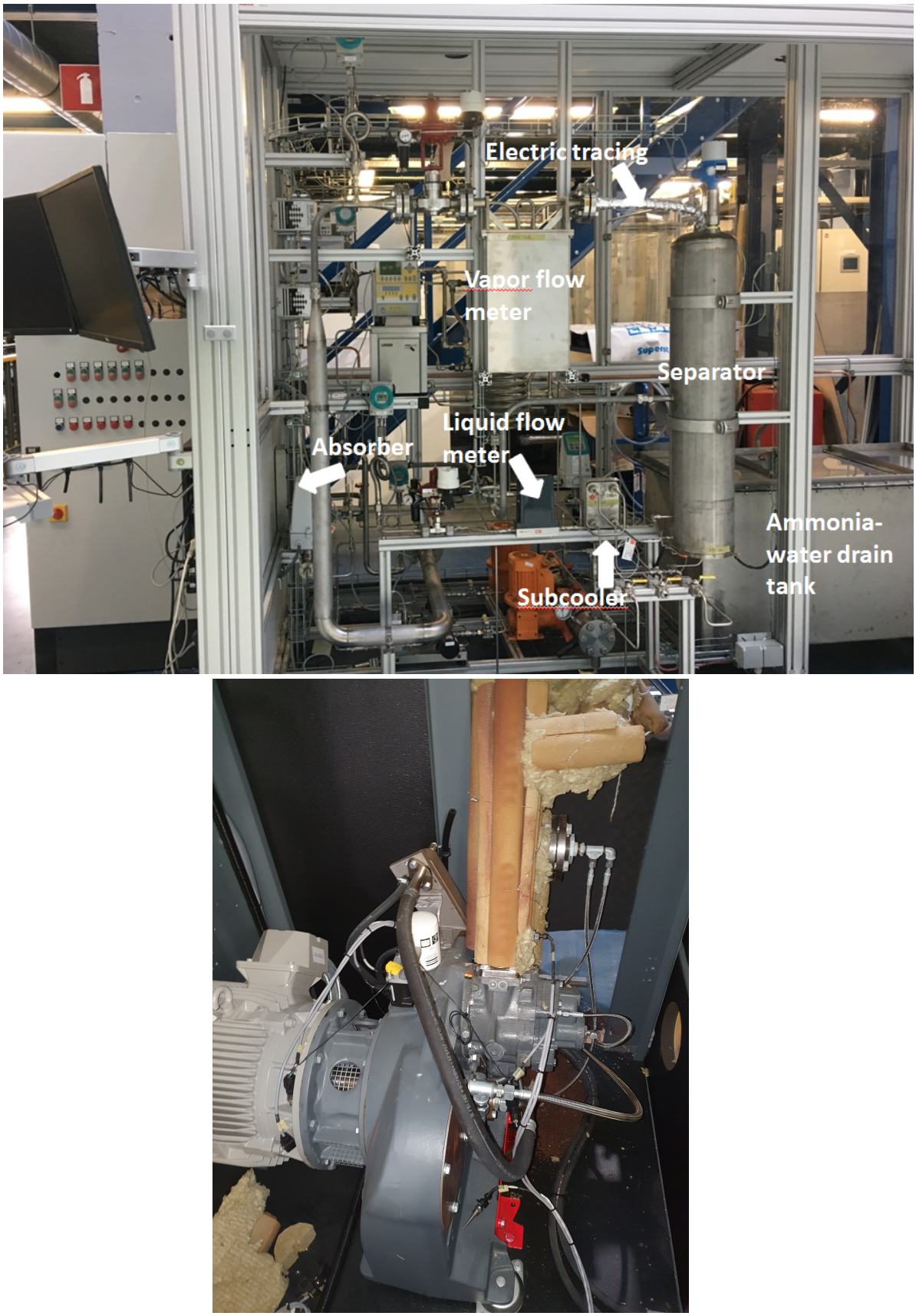

Figure 3.2: Photograph of the experimental setup. The picture on the top shows the main components of the setup except the compressor prototype which is shown on the bottom.

3.2. Preparation

To increase the accuracy and precision of the experimental data, new temperature sensors have been added to the setup. Since the setup already contained ammonia-water, the setup was drained before installing the sensors in. After the sensors had been connected, the entire system was pressure-tested before adding ammonia-water. Nitrogen was pumped into the system and kept at 11 bar. Using leaking spray, the leaks were noticed and closed. The system was then kept under pressure for approximately 60 hours. A 0.1 bar/hour pressure drop was observed. It was then deemed as acceptable. The nitrogen was then removed from the system. The setup was vacuumed and ammonia-water was pumped in keeping the ammonia concentration at 30 weight%.

New temperature sensors were added at the inlet and the outlet of the compressor for additional data accuracy. Three new sensors at the outlet and two new sensors at the inlet were added. At the outlet, there are now sensors from the top, bottom and either sides. On the inlet side, one new sensor is placed on the vapour side and liquid side. In addition to this, the outlet sensor from the top was replaced. A list of the new temperature sensors is shown in Table 3.3.

These sensors from TC Direct (the manufacturer) have been calibrated at the factory but still needed to be rechecked. The accuracy of the new temperature sensors needs to be ±0.06 K. A thermostatic bath was used to test these sensors against the readings of a precision thermometer. The precision thermometer has an accuracy of ±0.01 K. Temperatures from all new sensors and the thermometer were recorded from different set temperatures of the thermostatic bath. At each temperature level, three sets of readings were taken.

The thermostatic bath was set to 50°C, 75°C, 100°C, 125°C and 150°C. The thermostatic bath has four sensor input slots. Here three temperature sensors were fed into the slots at one time. The last slot was connected to the precision thermometer to validate the set temperatures.

Table 3.3: New Temperature Sensors Installed in the System

Sensor #	Location	Average Difference °C	Maximum Difference °C
801	Suction: Liquid phase	0.061	0.130
802	Suction: Vapour phase	0.040	0.130
803	Compressor Discharge	0.035	0.110
804	Compressor Discharge	0.061	0.120
805	Compressor Discharge	0.115	0.180
402	Compressor Discharge	0.004	0.070

At the compressor discharge, the accuracy of temperature sensor T-402 is much higher compared to the other sensors at the same location. Hence, for the discharge, only temperature sensor T-402 is considered. After validating the calibration done by the manufacturer, the setup is now ready to use. Before starting the compressor, the separator must be heated up to 110°C to allow the vapour to flow and the pressure in the system must be at least above atmospheric pressure.

3.3. Experimental Procedure

Once the separator is sufficiently heated up and the pressures are above the atmospheric pressure level, the compressor can be started gradually from lower speeds to desired speeds. Experiments

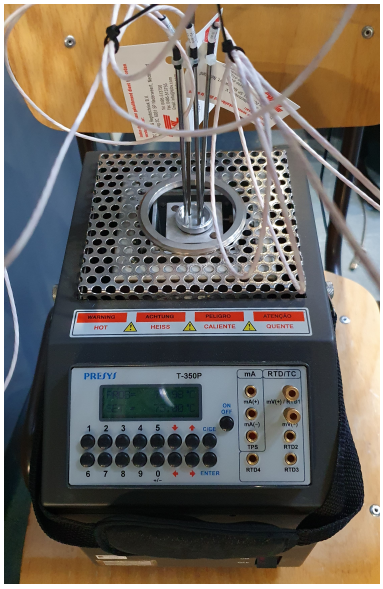

Figure 3.3: The thermostatic bath used for temperature calibration (left). The precision thermometer used for temperature calibration (right). This was used to validate the set temperature in the thermostatic bath

were carried out for increasing rotational speeds starting from 10320 rpm till 15500 rpm. The speed was controlled using SIEMENS SIMATIC software. The vapour quality at the inlet was varied by controlling the flows. Steady state was obtained at the desired vapour qualities by primarily tweaking the cooling water flows. Each steady state was maintained for approximately 30-45 minutes and data was recorded.

There are certain constraints which need to be taken into account while using the setup. One major constraint is the cooling water return temperature from the absorber (T-702). This temperature cannot be above 100°C for two reasons. Firstly, higher temperatures may lead to clogging in the heat exchanger. Secondly, there is no water treatment for the returning cooling water which may lead to lower cooling water flows which means less cooling (or absorption) and then at some point higher rotational speeds of the compressor might not be possible. The liquid line temperature after the subcooler should be between 70°C and 75°C to protect the electronics of the flow sensor. The temperature difference for the cooling water used to cool the oil is maintained between 4-5 K. Discharge temperatures must also be controlled.

3.4. Post-processing and Data Analysis

Once an experimental run is completed, the raw data is obtained as an Excel Comma Separated Value (CSV) file. This file is then analysed using MATLAB where the isentropic and volumetric efficiencies are calculated.

3.4.1. Homogeneous Calculation Scheme for Efficiency

The temperature and pressure inside the separator are used to determine the ammonia concentration in the vapour and liquid phase in the ammonia-water solution. Equilibrium is maintained between the liquid and vapour in the separator. These ammonia concentrations are found using the solution properties described in section 2.2.1 developed by Ziegler and Trepp (1984).

REFPROP is used to find property values like enthalpy, entropy and density (Lemmon et al., 2018). The ammonia concentrations are found based on the thermodynamic model by Ziegler and Trepp (1984). The temperature and pressure for the liquid line and vapour line are given in Appendix B.1. Appendix B.2 contains the experimental values of the temperature at the suction, discharge, and the

temperature lift across the compressor. Appendix B.3 contains the experimental values of the pressure at the suction and discharge. Appendix B.5 can be consulted for the experimental mass flows for the liquid, the vapour and cooling water.

$$w_{\mathrm{L}} = f(T_{405}, p_{404}, q = 0) \tag{3.1}$$

$$w_{\mathrm{v}} = f(T_{405}, p_{404}, q = 1.0) \tag{3.2}$$

Here the subscripts refer to the corresponding sensors at the respective points in Figure 3.1. The temperature (T_{405}) is the temperature sensor located after the absorber. The pressure (p_{404}) refers to the discharge pressure. The enthalpy of the liquid and vapour after expansion are given by Equation 3.3 and 3.4 respectively.

There are two additional temperature sensors on the vapour and liquid line. However, these temperature values are not considered to calculate the liquid and vapour enthalpies. This is because temperature sensors T-801 and T-802 are situated much closer to the compressor suction line whereas sensors T-406 and T-407 are situated immediately after the control valves. A temperature difference of approximately 9 K was seen in between the two sensors in the vapour line and 3 K between the two sensors on the liquid line. If suction sensor values, that is, T-401 and P-403, which are closest to the suction of the compressor, are considered while calculating the vapour and liquid enthalpy, there is seen a significant drop in the isentropic enthalpy at the discharge. The temperature measured at the suction is higher than the temperatures at the ends of the liquid and vapour lines. A pressure drop is also seen between the ends of the liquid (P-401) and vapour (P-402) lines and the suction (P-403). As a result, the enthalpy at the inlet (h_1) increases, reducing the efficiency. It was observed that the temperature at the suction is higher because there is already a small percentage of vapour at the end of the liquid line. Hence, the exact amount of liquid entering the compressor is unknown. In order to be as accurate as possible, temperature sensors T-801 and T-802 have been considered to calculate liquid and vapour enthalpies at the inlet before mixing of the flows.

Moreover, at the ammonia concentration in the liquid phase calculated using Equation 3.1, the quality is, in fact, non-zero. Throughout the datasets, on average a vapour quality (at the start of the liquid line) of 3% is seen. Due to this discrepancy in the thermodynamic model for ammonia-water, the ammonia concentration in the liquid phase was corrected via REFPROP by iterating the quality until it was ±0.0001 of a complete liquid state (that is, q = 0). The quality at the end of the liquid line is found at temperature and pressure from sensors T-801 and P-401 to check again for any presence of vapour (Appendix B.4). This is found to be within acceptable limits. Subsequently, the enthalpy of the liquid is found by Equation 3.3.

The vapour quality found by validating the ammonia concentration in vapour phase was within this limit (Appendix B.4). Hence, the thermodynamic model developed by Ziegler and Trepp (1984) was used to calculate w_{v}. Subsequently, the vapour enthalpy can be found using Equation 3.4.

$$h_{\mathrm{L}} = f(T_{801}, p_{401}, w_{\mathrm{L}}) \tag{3.3}$$

$$h_{\mathrm{v}} = f(T_{802}, p_{402}, w_{\mathrm{v}}) \tag{3.4}$$

Furthermore, a subcooler cools the liquid flow so that the liquid passing through the flowmeter has a temperature within acceptable range so as to preserve the electronics of the flowmeter (FT-401). The enthalpy of the liquid flow entering the subcooler in given by Equation 3.5. The amount of cooling done by the subcooler is given by Equation 3.6.

$$h_{\mathrm{in,sub}} = f(T_{405}, p_{404}, w_{\mathrm{L}}) \tag{3.5}$$

$$\dot{Q}_{\text{cw,sub}} = \dot{m}_{\text{cw,sub}} C_{\text{p,cw}} (T_{721} - T_{720}) \tag{3.6}$$

From energy balance, the enthalpy of the liquid flow coming out of the subcooler can be found using Equation 3.7.

$$h_{\text{out,sub}} = h_{\text{in,sub}} - \frac{\dot{Q}_{\text{cw,sub}}}{\dot{m}_{\text{L}}} \tag{3.7}$$

Using REFPROP, the temperature at this point can be calculated:

$$T_{\text{out,sub}} = f(p_{404}, h_{\text{out,sub}}, w_{\text{L}}) \tag{3.8}$$

Appendix B.9 gives the values used and obtained from the energy balance across the subcooler. On average, a 17 K heat loss is observed between the outlet of the subcooler and the end of the liquid line (T-801).

Now the enthalpy and solution concentration at the inlet of the compressor can be found using Equations 3.9 and 3.10 respectively. Appendix B.12 and B.11 contain all the experimental data for the enthalpies and concentrations respectively.

$$h_1 = \frac{\dot{m}_{\text{L}} h_{\text{L}} + \dot{m}_{\text{v}} h_{\text{v}}}{\dot{m}_{\text{flow}}} \tag{3.9}$$

$$w_1 = \frac{\dot{m}_{\text{L}} w_{\text{L}} + \dot{m}_{\text{v}} w_{\text{v}}}{\dot{m}_{\text{flow}}} \tag{3.10}$$

where

$$\dot{m}_{\text{flow}} = \dot{m}_{\text{L}} + \dot{m}_{\text{v}} \tag{3.11}$$

Here, the liquid mass flow rate is measured by flow meter FT-401 and vapour mass flow rate is measured by flow meter FT-402. The vapour quality at inlet is given by Equation 3.12. Appendix B.4 contains the experimental values for the inlet vapour quality.

$$q_1 = \frac{h_1 - h_{\text{L}}}{h_{\text{v}} - h_{\text{L}}} \tag{3.12}$$

Assuming homogeneous flow through the compressor, the concentration of ammonia remains constant throughout the compression process (Equation 3.13). State point 2 refers to the discharge conditions of the compressor while state point 1 refers to the suction conditions of the compressor as shown in Figure 3.1.

$$w_1 = w_2 \tag{3.13}$$

Now, the isentropic discharge enthalpy must be found.

$$s_1 = f(T_{401}, p_{403}, w_1) \tag{3.14}$$

$$h_{2,\text{is}} = f(s_2 = s_1, p_{404}, w_1) \tag{3.15}$$

The total isentropic efficiency including mechanical, motor and inverter losses is obtained from Equation 3.16.

$$\eta_{\text{total}} = \frac{(h_{2,\text{is}} - h_1)\dot{m}_{\text{flow}}}{\dot{W}_{\text{elec}}} \tag{3.16}$$

The motor loss is taken as 5% of the power and inverter loss is taken as 2%. This gives the power input to the compressor.

$$\dot{W}_{\text{in}} = 0.95 \cdot 0.98 \cdot \dot{W}_{\text{elec}} \tag{3.17}$$

The heat removed by the oil is given in Equation 3.18. This is assumed to be partially contributed by mechanical losses which take place outside the compression process (heat originated in the gearbox and bearings).

$$\dot{Q}_{\text{cw}} = \dot{m}_{\text{cw,oil}} C_{\text{p,cw}} (T_{\text{cw,out}} - T_{\text{cw,in}}) \tag{3.18}$$

Here, $T_{\text{cw,in}}$ refers to temperature sensor T-731 and $T_{\text{cw,out}}$ refers to temperature sensor T-732. Some of the heat removed by the oil comes from the process side (the compression process is non-adiabatic). The compressor rotors are heated by the compressed gas and the liquid droplets entering the compressor hit the rotors and cool them down. This is given by Equation 3.19. Appendix B.15 contains the experimental data of the removed heat (losses) of the system.

$$\dot{Q}_{\text{oil,process}} = U_{\text{rotor}} A_{\text{rotor}} (T_{402} - T_{401}) \tag{3.19}$$

Here, the overall heat transfer coefficient between the droplets and rotor is assumed to be high (10 $\text{kW/m}^2 - \text{K}$). The port area is the cross flow area for the droplets entering the compressor which is approximately 1600 mm^2 (Gudjonsdottir et al., 2020). Hence, the power required by the compressor for the compression process is given by Equation 3.20. Appendix B.10 contains the experimental data for the compressor power consumption.

$$\dot{W}_{\text{comp}} = \dot{W}_{\text{in}} - \dot{Q}_{\text{cw}} + \dot{Q}_{\text{oil,process}} \tag{3.20}$$

Hence, the isentropic efficiency of the compressor can be given by Equation 3.21. Appendix B.12 contains the isentropic efficiencies calculated using the experimental data.

$$\eta_{\text{is}} = \frac{(h_{2,\text{is}} - h_1)\dot{m}_{\text{flow}}}{\dot{W}_{\text{comp}}} \tag{3.21}$$

The outlet enthalpy based on the power added to the process flow can then be obtained from Equation 3.22.

$$h_2 = h_1 + \frac{\dot{W}_{\text{comp}}}{\dot{m}_{\text{flow}}} \tag{3.22}$$

The mechanical efficiency, excluding electrical motor losses, is obtained from Equation 3.23. Appendix B.13 contains the mechanical efficiency calculated using the experimental data.

$$\eta_{\text{mech}} = \frac{\eta_{\text{total}}}{\eta_{\text{is}}} \tag{3.23}$$

The liquid and vapour densities at the inlet are given by Equations 3.24 and 3.25 respectively.

$$\rho_{\text{L}} = f(p_{403}, q = 0, w_{\text{L}}) \tag{3.24}$$

$$\rho_{\text{v}} = f(p_{403}, q = 1, w_{\text{v}}) \tag{3.25}$$

Hence, the suction density is given by Equation 3.26.

$$\rho_1 = \frac{1}{\frac{1}{\rho_{\text{L}}}(1 - q_1) + \frac{1}{\rho_{\text{v}}} q_1} \tag{3.26}$$

The volumetric efficiency of the compressor is obtained from Equation 3.29 with ω the rotational speed of the male rotor in s^{-1}, z_1 is the number of male rotor lobes and r_{evap} is the percentage of the liquid flow which evaporates at the compressor inlet. $\dot{W}_{evap}$ refers to the latent heat of evaporation of ammonia-water.

$$\dot{Q}_{evap} = \dot{m}_L(h_v - h_L) \tag{3.27}$$

$$r_{evap} = \frac{\dot{Q}_{oil,process}}{\dot{Q}_{evap}} \tag{3.28}$$

$$\eta_{vol,evap} = \frac{\dot{m}_v + r_{evap}\dot{m}_L}{\rho_v \cdot V_{max} \cdot \omega \cdot z_1} \tag{3.29}$$

Appendix B.14 contains the volumetric efficiencies calculated using the experimental data.

For error propagation the method described by Taylor (1997) is used, where the uncertainty, *u*, of a function, *f*, can be described in general as given in Equation 3.30.

$$u_f = \sqrt{\left(\frac{\partial f}{\partial x}u_x\right)^2 + \ldots + \left(\frac{\partial f}{\partial z}u_z\right)^2} \tag{3.30}$$

where x,...,z are measured variables with uncertainties $u_x \ldots u_z$. If the relationship of the function is unknown then the uncertainty can be calculated by Equation 3.31.

$$u_f = \sqrt{(f(x,\ldots,z+u_x) - f(x,\ldots,z))^2 + \ldots + (f(x,\ldots,z+u_z) - f(x,\ldots,z))^2} \tag{3.31}$$

Appendix A contains all the equations used to determine the error propagation.

3.4.2. Heterogeneous Calculation Scheme

An alternative calculation scheme was also implemented. An assumption is made in the previous scheme that a homogeneous flow exists across the compressor and a fraction of the liquid evaporates. Tian et al. (2017) use a heterogeneous scheme wherein the vapour and liquid are treated separately. Here, we consider only the vapour being compressed. The liquid passes through the compressor exchanging heat with the vapour.

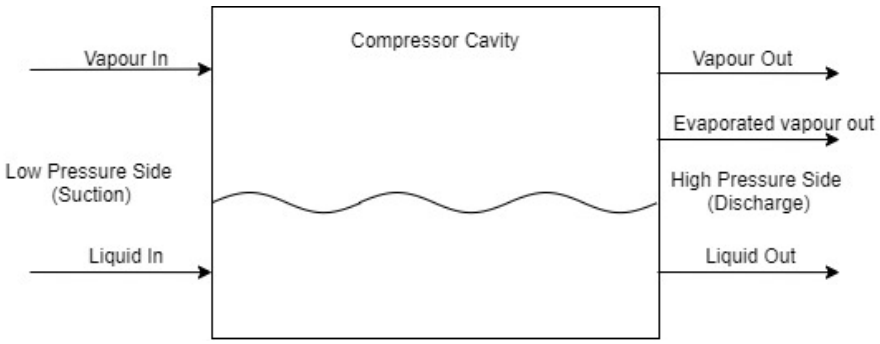

Figure 3.4: Schematic for the alternative approach to find the outlet enthalpy. A part of the liquid evaporates on touching the rotors cooling them down. This evaporated vapour adds to the ammonia concentration in the vapour.

The concentration of ammonia which has evaporated is given by Equation 3.32.

$$w_{vL} = f(T_{402}, p_{404}, q = 1) \tag{3.32}$$

The concentration of ammonia still in the liquid state is:

$$w_{\mathrm{LL}} = f(T_{402}, p_{404}, q = 0) \tag{3.33}$$

These concentrations are found using the thermodynamic properties given by Ziegler and Trepp (1984) for ammonia-water. The fraction of liquid which evaporated can be found using Equation 3.34.

$$q_{\mathrm{vL}} = \frac{w_{\mathrm{L}} - w_{\mathrm{LL}}}{w_{\mathrm{vL}} - w_{\mathrm{LL}}} \tag{3.34}$$

Now the concentration of ammonia in the vapour at the discharge is calculated using Equation 3.35.

$$w_{\mathrm{v,out}} = \frac{\dot{m}_{\mathrm{v}} w_{\mathrm{v}} + q_{\mathrm{vL}} \dot{m}_{\mathrm{L}} w_{\mathrm{vL}}}{\dot{m}_{\mathrm{v}} + q_{\mathrm{vL}} \dot{m}_{\mathrm{L}}} \tag{3.35}$$

The concentration of ammonia in the liquid can also be calculated via species balance.

$$w_{\mathrm{L,out}} = \frac{w_{\mathrm{L}} - q_{\mathrm{vL}} w_{\mathrm{vL}}}{1 - q_{\mathrm{vL}}} \tag{3.36}$$

The enthalpies of the vapour and liquid phases at the discharge are given by Equations 3.37 and 3.38 respectively.

$$h_{\mathrm{v,out}} = f(T_{402}, p_{404}, w_{\mathrm{v,out}}) \tag{3.37}$$

$$h_{\mathrm{L,out}} = f(T_{402}, p_{404}, w_{\mathrm{L,out}}) \tag{3.38}$$

Hence, now the overall enthalpy and concentration of the ammonia-water solution at the discharge is calculated using Equation 3.39 and 3.40 respectively.

$$h_{2,\mathrm{het}} = \frac{(\dot{m}_{\mathrm{v}} + q_{\mathrm{vL}} \dot{m}_{\mathrm{L}}) h_{\mathrm{v,out}} + (1 - q_{\mathrm{vL}}) \dot{m}_{\mathrm{L}} h_{\mathrm{L,out}}}{\dot{m}_{\mathrm{flow}}} \tag{3.39}$$

$$w_{2,\mathrm{het}} = \frac{(\dot{m}_{\mathrm{v}} + q_{\mathrm{vL}} \dot{m}_{\mathrm{L}}) w_{\mathrm{v,out}} + (1 - q_{\mathrm{vL}}) \dot{m}_{\mathrm{L}} w_{\mathrm{L,out}}}{\dot{m}_{\mathrm{flow}}} \tag{3.40}$$

Hence, the power required for the compression process is given by Equation 3.41. This is the actual power provided to the compression process. $h_{2,\mathrm{het}}$ accounts for the difference in concentrations and flows between the vapour and liquid phases.

$$\dot{W}_{\mathrm{comp,het}} = \dot{m}_{\mathrm{flow}} (h_{2,\mathrm{het}} - h_1) + \dot{Q}_{\mathrm{oil,process}} \tag{3.41}$$

The compression power required is on average 9.75 kW less than what is required assuming a homogeneous flow. The calculated values for the heterogeneous scheme are given in Appendix C.

As said above, the liquid extracts heat from the rotors and evaporates into vapour. Since this process happens at the beginning of suction, the newly formed vapour ($q_{\mathrm{vL}} \dot{m}_{\mathrm{L}}$ kg/s) also undergoes compression. The isentropic discharge enthalpy can be calculated using REFPROP. This enthalpy is calculated using the overall vapour outlet concentration $w_{\mathrm{v,out}}$.

$$s_{1,\mathrm{het}} = f(T_{401}, p_{403}, w_{\mathrm{v}}) \tag{3.42}$$

$$h_{2,\mathrm{is,het}} = f(s_{2,\mathrm{het}} = s_{1,\mathrm{het}}, p_{404}, w_{\mathrm{v,out}}) \tag{3.43}$$

And the isentropic efficiency then becomes:

$$\eta_{\text{is,het}} = \frac{(h_{2,\text{is,het}} - h_{\text{v}})(\dot{m}_{\text{v}} + q_{\text{vL}}\dot{m}_{\text{L}})}{\dot{W}_{\text{comp,het}}} \tag{3.44}$$

The total isentropic efficiency is given by Equation 3.45 and the mechanical efficiency for the heterogeneous approach is given by Equation 3.46.

$$\eta_{\text{total,het}} = \frac{(h_{2,\text{is,het}} - h_{\text{v}})(\dot{m}_{\text{v}} + q_{\text{vL}}\dot{m}_{\text{L}})}{\dot{W}_{\text{elec}}} \tag{3.45}$$

$$\eta_{\text{mech,het}} = \frac{\eta_{\text{total,het}}}{\eta_{\text{is,het}}} \tag{3.46}$$

Table 3.4 gives an overview of the accuracy of different relevant variables.

Table 3.4: Average Accuracy of the Parameters for 38 datasets

Parameter		Accuracy	Unit
Vapour Quality	q_1	±0.006900	kg/kg
Pressure Ratio	Pr	±0.02450	
Ammonia Concentration	w_1	±0.005700	kg/kg
Electric Power	$\dot{W}_{\text{elec}}$	±500.0	W
Heat removed by oil	$\dot{Q}_{\text{cw}}$	±92.35	W
Process Heat removed by oil	$\dot{Q}_{\text{oil process}}$	±1.357	W
Power given to the compressor	$\dot{W}_{\text{in}}$	±465.5	W
Power required by compressor	$\dot{W}_{\text{comp}}$	±474.8	W
Fraction of evapouration	r_{evap}	$\pm 1.010 \cdot 10^{-04}$	
Total Isentropic Efficiency	$\eta_{\text{is,total}}$	±0.02820	
Isentropic Efficiency	η_{is}	±0.03830	
Mechanical Efficiency	η_{mech}	±0.1933	
Volumetric Efficiency	$\eta_{\text{vol,evap}}$	±0.005300	
Power required by compressor (het.)	$\dot{W}_{\text{comp,het}}$	±509.9	W
Total Isentropic Efficiency (het.)	$\eta_{\text{total,het}}$	±0.007700	
Isentropic Efficiency (het.)	$\eta_{\text{is,het}}$	±0.04070	
Mechanical Efficiency (het.)	$\eta_{\text{mech,het}}$	±0.03570	

3.5. Experimental Results: Homogeneous Calculation Scheme

The experimental results using the procedure in 3.4.1 are shown and discussed here.

3.5.1. Pressure Ratio and Vapour Quality

The pressure ratio is calculated between the discharge (p_{404}) and suction pressures (p_{403}). Figure 3.5 shows the operating points of the experimental runs. Steady state at these rotational speeds and corresponding pressure ratios was achieved. Attaining steady state for higher vapour qualities at higher rotational speeds was difficult. 38 datasets were recorded. Figure 3.6 shows that with lower vapour qualities, that is, higher amount of liquid in the ammonia-water solution at the inlet of the compressor, higher pressure ratios can be attained for the same rotational speed. This is an advantage of operating the compressor in the wet compressor regime. Higher rotational speeds can also lead to higher pressure ratios.

$$Pr = \frac{p_{404}}{p_{403}} \tag{3.47}$$

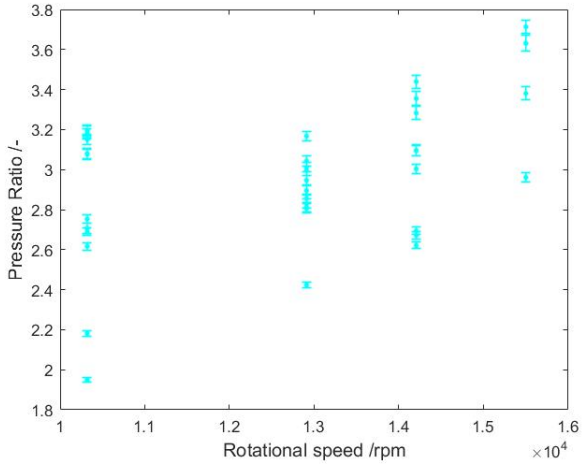

Figure 3.5: Pressure ratios for different rotational speeds. These points represent at which pressure ratios the experiments were carried out, that is, the pressure ratios where steady state was attainable.

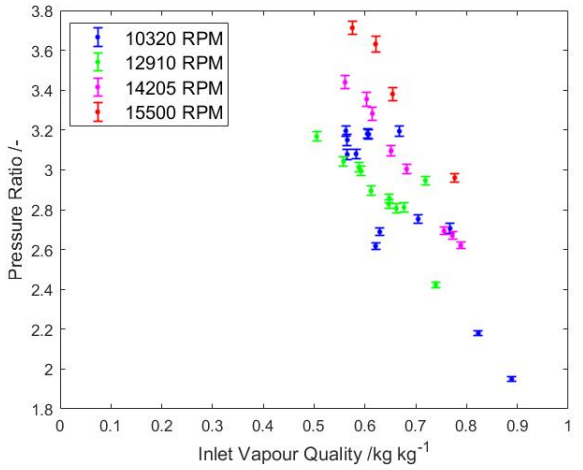

Figure 3.6: Pressure ratio as a function of vapour quality at the inlet of the compressor for different rotational speeds. This graph shows the rotational speeds, the pressure ratios and the vapour qualities at which steady state was achieved.

3.5.2. Temperature Lift

The temperature lift across the compressor is given in 3.48. Figure 3.7 (left) shows the temperature lifts that were attained from the experimental runs for different rotational speeds. Higher temperature lifts can be attained for higher rotational speeds.The compressor discharge temperature was maintained in the range 110 °C to 120 °C to prevent rapid increase of the water side fouling of the absorber. The suction temperature resulted indirectly from the outlet conditions after the absorber. Figure 3.7 (right) shows that higher temperature lifts are possible for higher amounts of liquid at the inlet of the compressor. This could be related to attaining higher pressure ratio for the same conditions.

$$T_{\text{lift}} = T_{402} - T_{401} \tag{3.48}$$

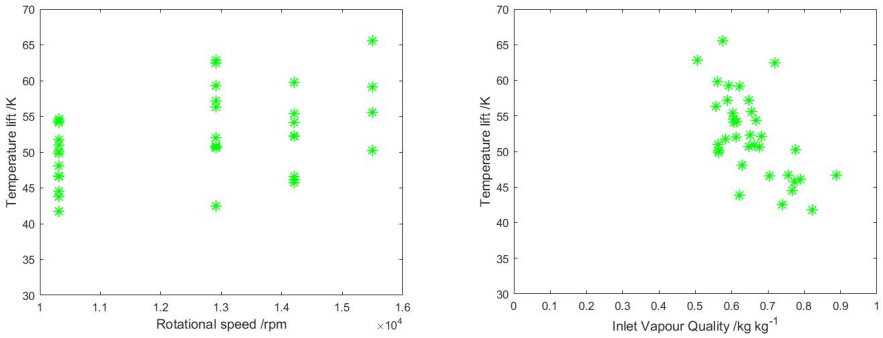

Figure 3.7: Left: Temperature lift as a function of rotational speeds; Right: Temperature lift as a function of vapour quality at the inlet of the compressor.

3.5.3. Power Consumption and Losses

From Figure 3.8 is it clear that as the rotational speed increases, the compressor requires more power. The amount of losses (Figure 3.9) (left) increases as the rotational speed is increased. The heat removed by the oil from the process side and from the mechanical losses such as bearings, gearbox is shown here. The mechanical loss is the difference between the heat removed by the cooling water and the heat lost from the process side. Also, for higher rotational speeds, the mechanical losses show a significant increase whereas the process side losses show almost no change. As a result, the compressor requires more power input from the electric motor for higher speeds (Figure 3.9 right).

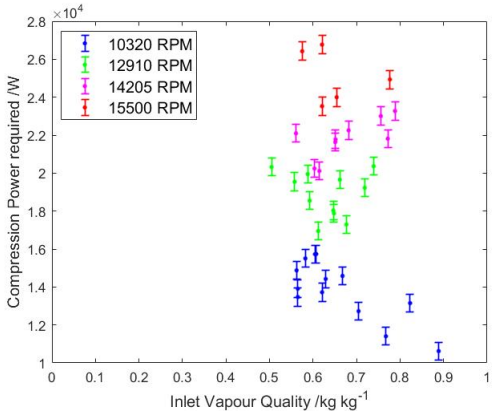

Figure 3.8: Power required by the compressor ($\dot{W}_{\text{comp}}$) for the compression process as a function of vapour quality for different rotational speeds

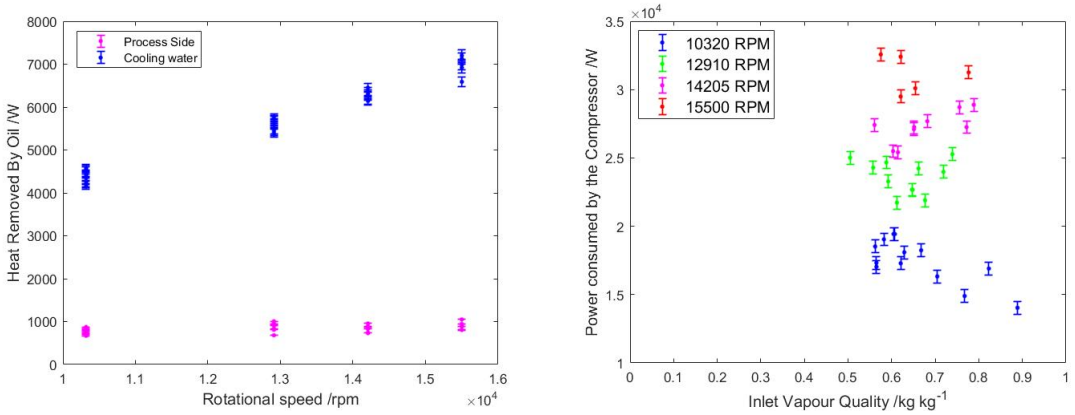

Figure 3.9: Power input to the compressor ($\dot{W}_{\text{in}}$) as a function of vapour quality for different rotational speeds

3.5.4. Isentropic Efficiency

The total isentropic efficiency includes all the losses and hence, is smaller than the isentropic efficiency. Figure 3.10 and 3.11 show the total isentropic efficiency and isentropic efficiency for different rotational speeds as a function of the inlet vapour quality respectively. The figures seems to indicate that, generally, the isentropic efficiency reduces when the amount of liquid in the flow is reduced (vapour quality increases). At these rotational speeds the liquid seems to seal part of the leakage paths increasing the isentropic efficiency. It also shows that for higher rotational speed the isentropic efficiency is practically independent of the inlet vapour quality. Figure 3.11 also seems to indicate that the isentropic efficiency reduces with increasing rotational speed. Displacing the incompressible liquid seems to create a large amount of additional isentropic losses. From Figure 3.11, the highest isentropic efficiency attained is 0.4413 (dataset 7) and the lowest is 0.07791 (dataset 11) for rotational speed of 10320 rpm and an inlet vapour quality of about 0.56 (dataset 7) and 0.88 (dataset 11).

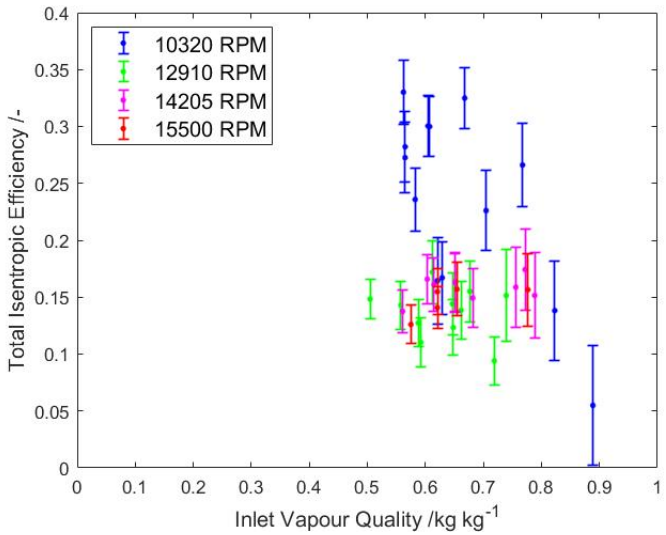

Figure 3.10: Total isentropic efficiency as a function of vapour quality at the inlet of the compressor for different rotational speeds

Gudjonsdottir et al. (2020) have done a detailed analysis to study this behaviour for the datasets with the highest and lowest isentropic efficiencies. They show that the vapour leaving the compressor is superheated. The temperature measured by the sensors at the outlet of the compressor is, most probably, the liquid temperature only. While in dataset 7 the liquid removes 5.2 kW from the vapour flow, in dataset 11 only 1.7 kW are removed so that the gas temperature can rise significantly. Also the

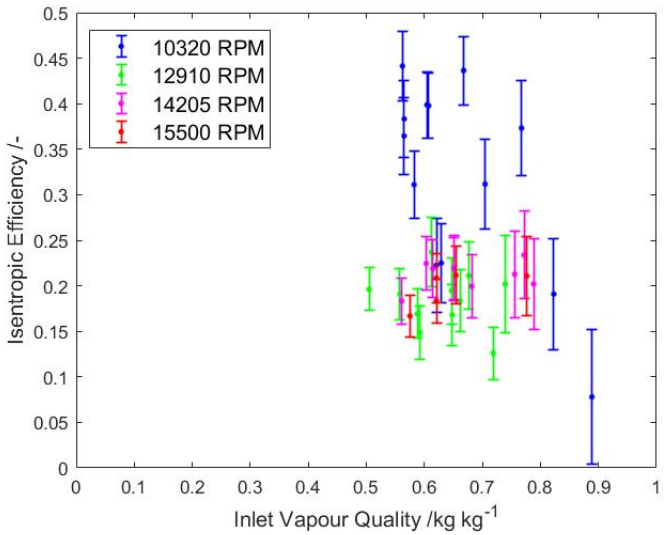

Figure 3.11: Isentropic efficiency as a function of vapour quality at the inlet of the compressor for different rotational speeds

pressure ratio is smaller for dataset 11 so that also a smaller isentropic efficiency would be expected. A superheating of 123 K is seen for dataset 11 indicating that the vapour leaves the compressor at 230°C what must have a large impact on the compressor bearings and shaft seals on the discharge side of the compressor.

Furthermore, for dataset 40 (15500 rpm, q_1 = 0.57), the efficiency is 0.1667. Gudjonsdottir et al. (2020) compare this to dataset 7, which has a similar inlet vapour quality. The superheating for dataset 7 (high efficiency) is small (about 25 K) while the superheating for dataset 40 (low efficiency) is large (about 161 K). In this case the vapour temperature attains an extremely high value of 284°C, very harsh conditions. The liquid / vapour mixture still travels for about 1 m through the discharge line making possible that the four sensors installed in the discharge line measure a lower (liquid) temperature. At higher rotational speeds, more vapour is being compressed while a similar amount of liquid is brought to discharge conditions. The data does not directly indicate that a lower efficiency would be expected at higher rotational speeds. The significantly higher discharge temperature remains hidden because the temperature sensors at the outlet of the compressor just measure the liquid temperature.

The effect of pressure ratio on the isentropic efficiency can be seen in Figure 3.12. For a rotational speed of 10320 rpm, the isentropic efficiency increases linearly with the pressure ratio up to a pressure ratio of 3.2. For higher rotational speeds, the isentropic efficiency seems to be independent of the pressure ratio in the range of pressure ratios 2.5 to 3.8. This might be related to the limits of operation of the absorber in relation to deposition of fouling on its water side at elevated temperatures. The absorber is cooled by untreated cooling tower water and high outlet temperatures lead to a high rate of deposition of $CaCO_3$ on the heat exchanger surface. The ammonia concentration at the compressor inlet increases with the pressure ratio. Additionally it seems that at higher rotational speed the superheating of the vapour at the outlet of the compressor becomes extremely high. It seems that, to obtain acceptable isentropic efficiencies, operating conditions for which superheating of the vapour may occur must be prevented.

The isentropic efficiency forms a downward parabola trend with the pressure ratio. The built-in volume ratio for this setup is 2.45. This gives a built-in pressure ratio of the system to be approximately 3.0. From the figures, it can be seen that at this pressure ratio, the isentropic efficiency tends to be at its peak.

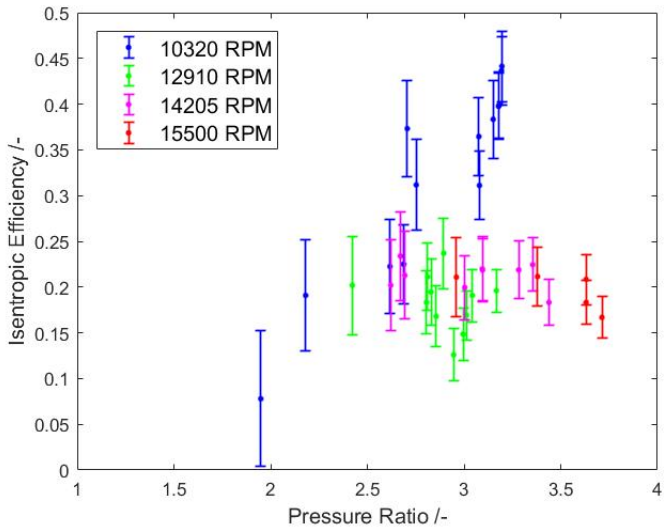

Figure 3.12: Isentropic efficiency as a function of pressure ratio for different rotational speeds

3.5.5. Mechanical Efficiency

Figure 3.13 shows how the mechanical efficiency varies with the rotational speed of the compressor in the range 10320 to 15500 rpm. The mechanical efficiency seems, in the range of the experiments, to be practically independent of the rotational speed. The experimental data indicates that the lower the quality, the higher the mechanical efficiency. The mechanical efficiency is slightly dependent on the assumptions made that some heat is lost from the process side as well. Considering this assumption, the mechanical efficiency has an average value of 0.7406. The lowest value is 0.7047 (dataset 11) while the highest value is 0.7689 (dataset 37).

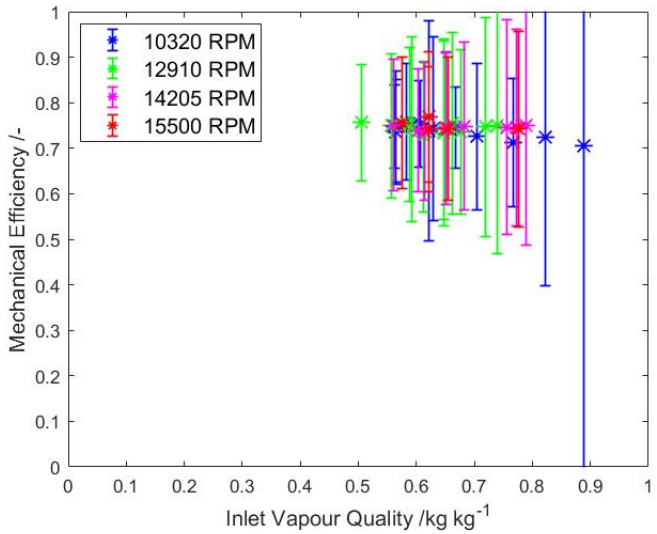

Figure 3.13: Mechanical efficiency as a function of vapour quality at the inlet of the compressor for different rotational speeds

Moreover, Figure 3.14 shows how the mechanical efficiency depends on the pressure ratio. Higher rotational speed is required to attain higher pressure ratios. In the investigated range, the mechanical efficiency is practically independent of the pressure ratio.

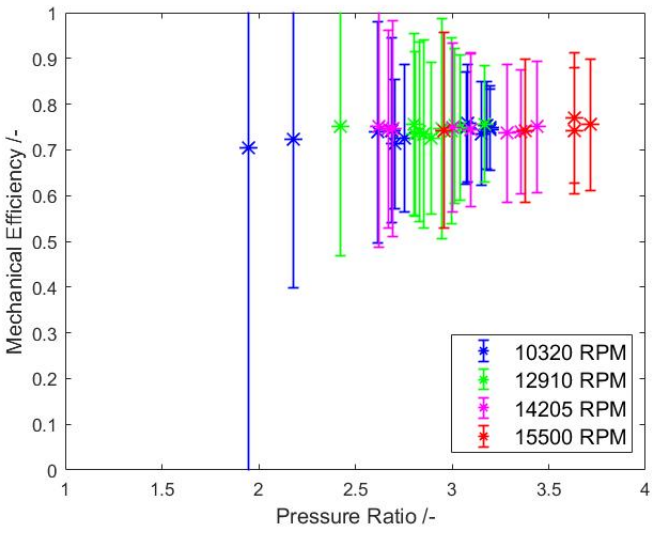

Figure 3.14: Mechanical efficiency as a function of pressure ratio for different rotational speeds

3.5.6. Volumetric Efficiency

Figure 3.15 shows how the volumetric efficiency changes with the vapour quality and rotational speed. The highest amount of liquid evaporation is 2.721% (dataset 18) while the lowest is 0.9769% (dataset 23). Dataset 39 shows the the highest volumetric efficiencies (0.4372) while dataset 12 shows the lowest (0.2397).

It can be seen that generally the volumetric efficiency decreases with an increase in liquid amount at the compressor inlet. Direct contact between the relatively cold liquid droplets and the hot rotors may lead to the evaporation of some of the liquid, partially filling the suction cavity. Also the liquid shall reduce the cavity size. Since pressure ratio increases at lower qualities, leakages losses may contribute to the large spread of the volumetric efficiency. This also might explain why, at lower inlet vapour qualities, the volumetric efficiency reduces with an increase in rotational speed.

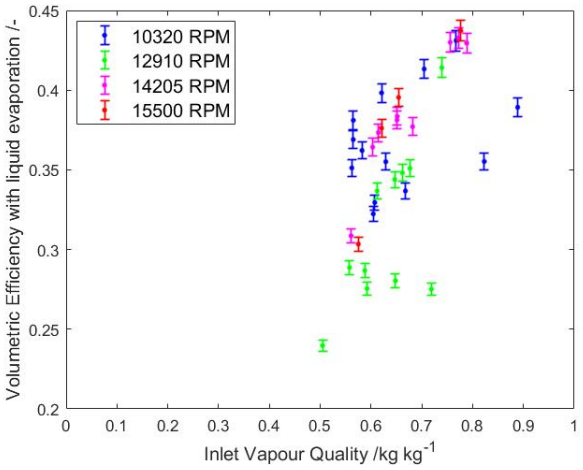

Figure 3.15: Volumetric efficiency as a function of vapour quality at the inlet of the compressor for different rotational speeds.

The effect of pressure ratios on the volumetric efficiency can be seen in Figure 3.16. The volumetric efficiency seems to depend significantly on the pressure ratio. The volumetric efficiency drops from 0.4141 at a pressure ratio of 2.42 to 0.239 at a pressure ratio of 3.16 for 12910 rpm, The volumetric

efficiency is approximately in the same range for 10320 rpm, 14205 rpm and 15500 rpm, that is, from 0.3 to 0.45.

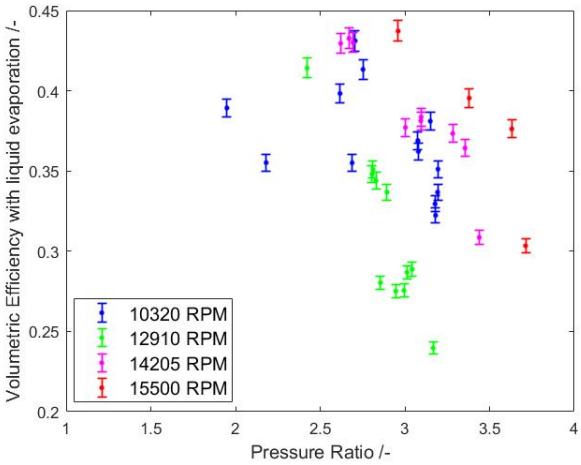

Figure 3.16: Volumetric efficiency as a function of pressure ratio for different rotational speeds considering partial liquid evapouration.

3.6. Reproducibility of experimental results

Based on the results for the isentropic, mechanical and volumetric efficiencies using the homogeneous calculation scheme, it was decided to perform additional experiments to confirm the reproducibility of the experiments. At a rotational speed of 7740 rpm it was not possible to operate the system at steady state conditions. The lowest rotational speed for which it was possible to run under steady state conditions was 9030 rpm. At this rotational speed the performance of the compressor is comparable to the behavior at 10320 rpm. Hence, these experiments were performed at 10320 rpm and 9030 rpm. These experiments were performed after approximately two months from when the previous 10320 rpm runs were performed. In these two months, the experimental runs for the other rotational speeds were performed. The data is saved in datasets 42 to 49 (10320 rpm) and 50 to 51 (9030 rpm). It seems that after 38 runs in approximately two months the performance of the compressor did not show any degradation. A lower rotational speed cannot maintain steady state conditions indicating that the volumetric efficiency becomes too low at this speed. Figure 3.18 shows that the volumetric efficiency did not change during this period.

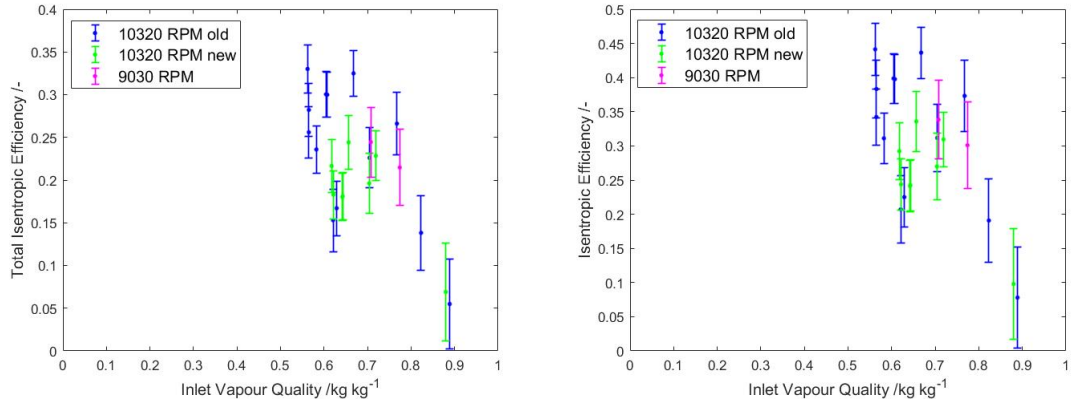

Figure 3.17: Isentropic efficiency as a function of vapour quality at the compressor inlet for different rotational speeds comparing the new experimental runs with the older runs.

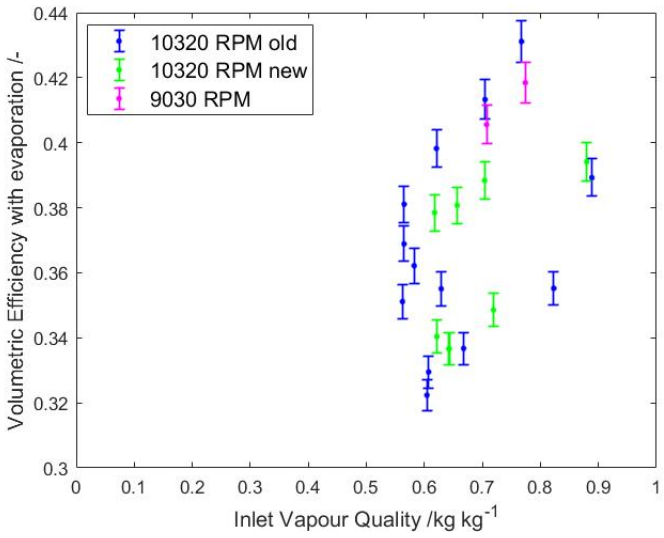

Figure 3.18: Volumetric efficiency as a function of vapour quality at the compressor inlet for different rotational speeds considering partial liquid evapouration comparing the new experimental runs with the older runs.

3.7. Experimental Results: Heterogeneous Calculation Scheme

In section 3.4.2, the discharge enthalpy was found by the treating the vapour and liquid separately. Subsequently, the required compression power and isentropic efficiency are calculated.

3.7.1. Required Compression Power

As can be seen from Figure 3.19, the compressor requires much less power as compared to the homogeneous scheme since we only consider the vapour compression. The compression power reduces as the amount of liquid in the compressor reduces. The power needed to undergo compression increases as the we increase the rotational speed. The average power needed for the compression process is 7.800 kW.

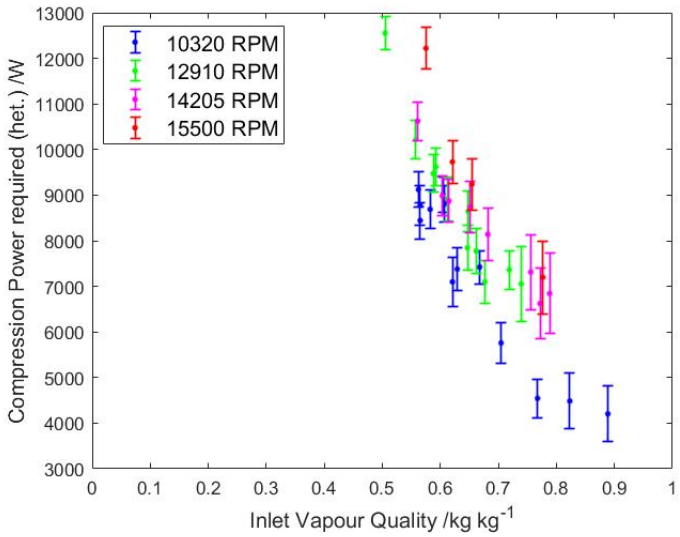

Figure 3.19: Power required for the compression process as a function of the vapour quality at the inlet of the compressor for different rotational speeds using a heterogeneous calculation scheme

3.7.2. Isentropic Efficiency

Higher values of isentropic efficiencies are achieved using a heterogeneous calculation scheme as seen in Figure 3.20. The highest efficiency is seen for dataset 26 (0.7523) and lowest for dataset 11 (0.1733). On average, the isentropic efficiency is 46.25% . For 10320 rpm, the isentropic efficiency first increases till q_1 = 0.76 then falls down. For higher rotational speeds, the isentropic efficiency increases with decrease with the amount of liquid at the inlet of the compressor. For 10320 rpm, the isentropic efficiency still increases with pressure ratio. For higher rotational speeds, the isentropic efficiency decreases as the pressure ratio increases.

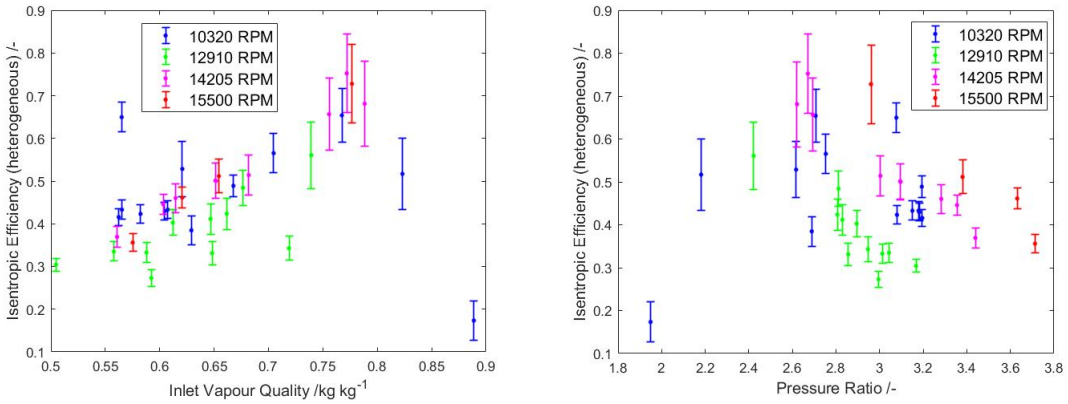

Figure 3.20: Isentropic efficiency as a function of vapour quality at the inlet of the compressor (left) and pressure ratio (right) for different rotational speeds using a heterogeneous calculation scheme

In section 3.5.4, it was found that the vapour was superheated for datasets 7, 11 and 40. The vapour enthalpy given in Equation 3.37 is now calculated considering this superheating. Subsequently, its effect on the isentropic efficiency can be seen in Table 3.5. Due to the superheat, $h_{2,\text{het}}$ increases. Consequently, the compression power ($\dot{W}_{\text{comp,het}}$) increases and reduces the efficiency.

Table 3.5: Effect of Vapour Superheating at the Discharge on Isentropic Efficiency

Dataset	Superheat [K]	$\dot{W}_{\text{comp,het}}$ [kW]	$\eta_{\text{is,het}}$
7	25	10.89	0.3759
11	123	10.80	0.06740
40	161	19.91	0.2185

The total isentropic efficiency is calculated without accounting for any losses. It is found with respect to the power provided to the compressor by the electric motor. The heterogeneous total isentropic efficiency for the experimental runs is shown in Figure 3.21 (left) as a function of the inlet vapour quality and as a function of the pressure ratio in Figure 3.21 (right). The total isentropic efficiency is considerably lower that the isentropic efficiency due to these unaccounted losses.

The mechanical efficiency is the ratio of the total isentropic efficiency to the isentropic efficiency. Figure 3.22 shows how the mechanical efficiency varies as as function of the inlet vapour quality and the pressure ratio. From the Figure, it can be seen that the mechanical efficiency reduces with an increase in vapour quality and increases with higher pressure ratios for all rotational speeds.

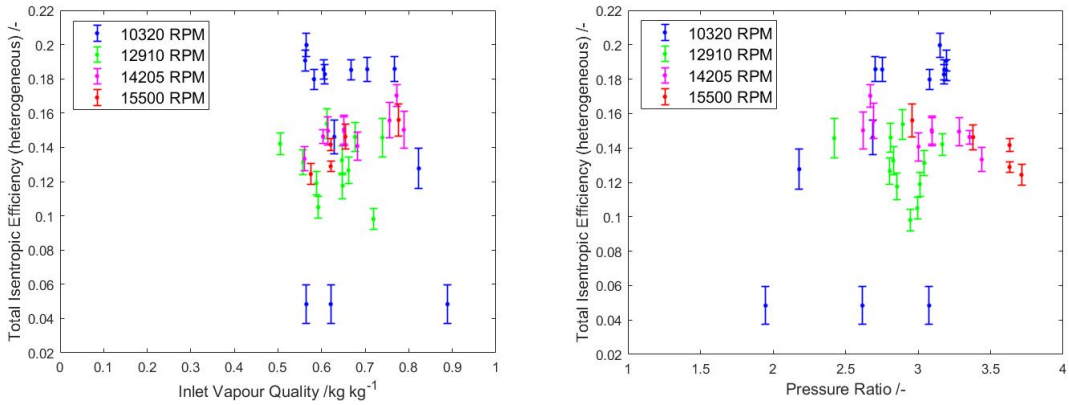

Figure 3.21: Total Isentropic efficiency as a function of vapour quality at the inlet of the compressor (left) and pressure ratio (right) for different rotational speeds using a heterogeneous calculation scheme

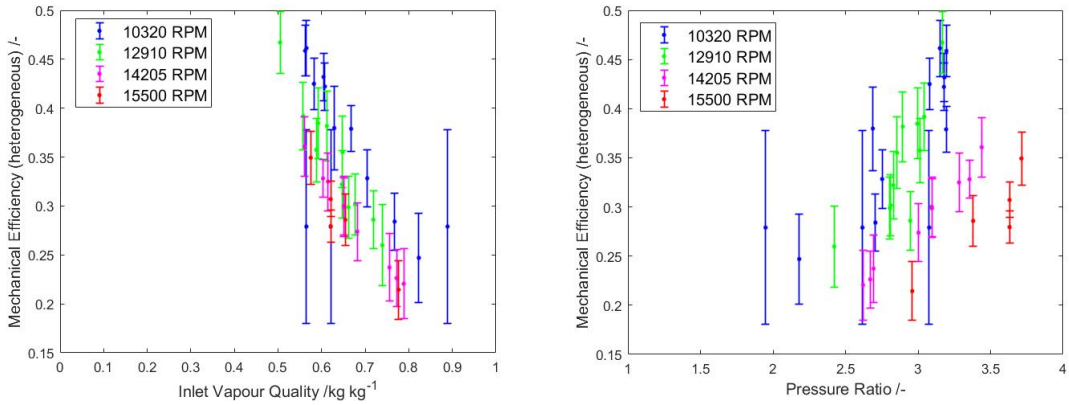

Figure 3.22: Mechanical efficiency as a function of vapour quality at the inlet of the compressor (left) and pressure ratio (right) for different rotational speeds using a heterogeneous calculation scheme

3.7.3. Reproducibility of Results

Figure 3.23 shows that the isentropic efficiency does not change drastically after two months of operation. It shows an upward going trend with pressure ratio. The isentropic efficiency drops after reaching a vapour quality of 0.76. From these graphs it can be seen that the performance of the compressor at 9030 rpm is similar to that at 10320 rpm.

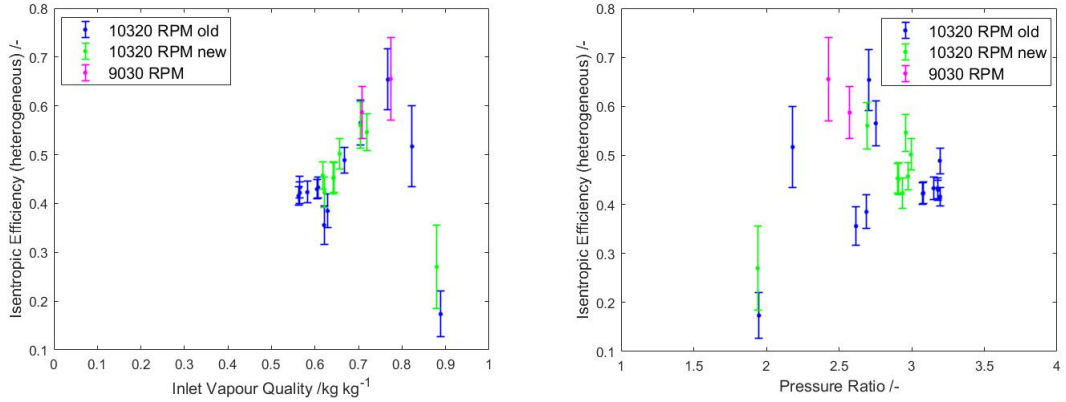

Figure 3.23: Isentropic efficiency as a function of vapour quality at the inlet of the compressor (left) and pressure ratio (right) for different rotational speeds using a heterogeneous calculation scheme comparing the new experimental runs with the older runs

Figure 3.24 shows the heterogeneous total isentropic efficiency after two months of operation. The new experiments fill in the gap to get a complete trend line. The total isentropic efficiency increases with pressure ratio and decrease with a reduction in the amount of liquid in the working fluid. It can also be seen that the total isentropic efficiency remains almost unchanged between a pressure ratio 2.9 to 3.2 and a vapour quality of 0.56 to 0.62.

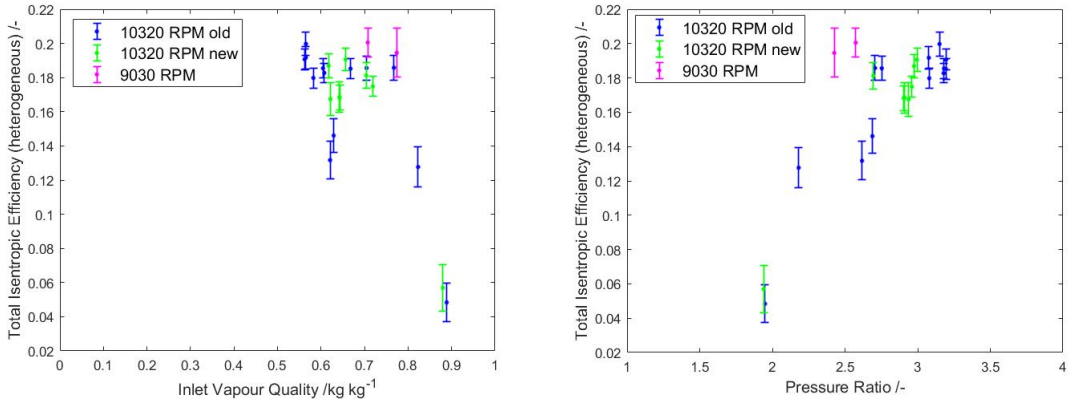

Figure 3.24: Total Isentropic efficiency as a function of vapour quality at the inlet of the compressor (left) and pressure ratio (right) for different rotational speeds using a heterogeneous calculation scheme comparing the new experimental runs with the older runs

Figure 3.25 shows the mechanical efficiency after two months of operation. The mechanical efficiency trends of the new experiments are also similar to that of the old experiments.

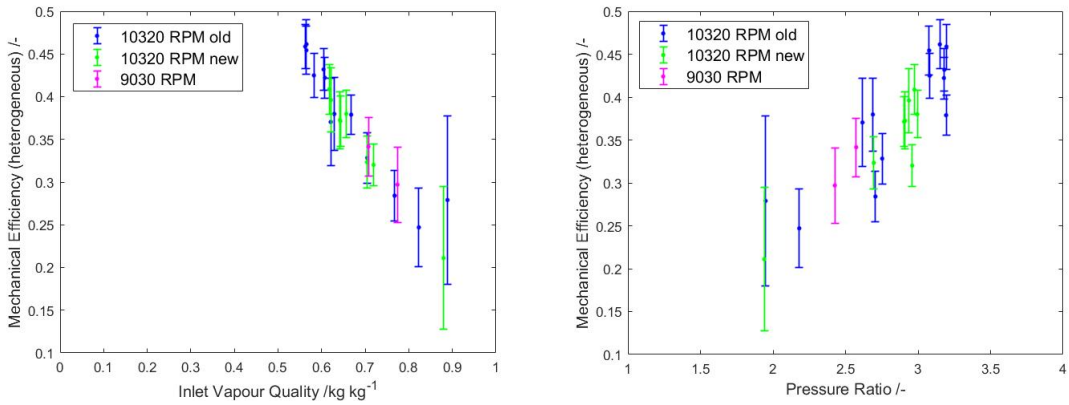

Figure 3.25: Mechanical efficiency as a function of vapour quality at the inlet of the compressor (left) and pressure ratio (right) for different rotational speeds using a heterogeneous calculation scheme comparing the new experimental runs with the older runs

3.8. Optimum Working Domain of the Compressor

Based on the results of the homogeneous and heterogeneous calculation schemes, optimum working domains for both the schemes are obtained given in Table 3.6. This ranges have been determined from the figures given in the previous sections. The volumetric efficiency increases until an inlet vapour quality of 0.8. However, the isentropic efficiency reduces above q_1 = 0.7. For the heterogeneous model, mechanical efficiency is higher for inlet vapour qualities < 0.6. While determining the optimum working domains, greater importance is given to isentropic efficiency while determining the working domains as maximizing η_{is} is the primary objective. Between an inlet vapour quality of 0.6-0.7 and pressure ratios between 2.5-3.2, both approaches seem to maximize the isentropic efficiency.

Table 3.6: Working Domains for the Twin-Screw Compressor utilizing Wet Compression

Parameter	Homogeneous Scheme	Heterogeneous Scheme
Inlet Vapour Quality	0.5-0.7	0.6-0.76
Pressure Ratio	2.75-3.25	2.5-3.2

4

Modelling

We are kept from our Goal not by obstacles, but by a clear path to a lesser Goal

Bhagavad Gita

Guðmundsdóttir (2018) developed a simplified model for the twin-screw compressor. However, several changes were made known only during this thesis and hence the model needed to be modified as well. The volume curve and compressor port locations and sizes were based on work done by Zaytsev (2003) and Tang (1995). The leakage locations and sizes were also based on the work done by these authors. Guðmundsdóttir (2018) estimated the maximum cavity volume by using an approximation of the volumetric flowrate at a particular rotational speed. Now, the maximum volume in a cavity is known. However, the exact locations and sizes of the compressor ports as well as the leakage paths as functions of the male rotor angle for one compression cycle are still not exactly known.

In order to accurately validate the model for the twin-screw compressor, another similar compressor was used to estimate the various port sizes and locations. This compressor has five male rotor lobes and six female rotor lobes. The compressor used for experimentation has the same amount of female rotor lobes but four male rotor lobes. Since the curves are developed using the rotation angle of the driving rotor, that is, the male rotor, the compressor port locations and sizes were noted for the female rotor lobe and then converted to the corresponding male rotor lobes using Equation 4.1.

$$\frac{\varphi_2}{\varphi_1} = \frac{z_1}{z_2} \tag{4.1}$$

Once the compressor geometry along with the leakage paths are known, the homogeneous experimental results are compared with the homogeneous model results. Fleming and Tang (1995) identified three leakage paths that have the most significant impact on the indicated (here, isentropic) and volumetric efficiency of the compressor: leakage through the contact line, the sealing line and through the housing cusp blow hole. The sizes of these leakages are varied to see their effect. An average clearance is assumed for the twin-screw compressor. However, after months of operation, this clearance may increase. Hence, the impact of different clearances is also discussed.

The mass flow rate inside the compressor is calculated as shown in Equation 4.2.

$$\dot{m}_{\text{flow}} = z_1 \frac{n}{60} \int \frac{\partial m}{\partial \varphi} d\varphi \tag{4.2}$$

While calculating the mass flow rate, an empirical flow correction coefficient is required to account for non-isentropic effects. Prins and Infante Ferreira (2000) obtained the flow coefficients experimentally by getting the best fit of the analytical results to the experimental results for particular operating

conditions. Screw compressor isentropic and volumetric efficiencies go down with increasing clearances. The coefficients depend on the geometry of the compressor and the process medium (Zaytsev, 2003). Coefficients for the leakage flow, the suction flow and discharge flow have also be varied to study their effect on the efficiencies and the mass flow rate of the compressor.

4.1. Geometrical Characteristics of the Compressor

Certain characteristics of the twin screw compressor are required in the model. These are the compressor cavity volume, the suction and discharge port areas and the leakage paths. It is convenient to express these geometrical characteristics as a function of the male rotor angle. In this section, the work of two researchers regarding compressor geometry are discussed, namely Zaytsev (2003) and Tang (1995). Table 4.1 and Table 4.2 list the geometrical characteristics of the compressors used by each of the researchers respectively. Tang (1995) developed a global program to describe and calculate the geometrical characteristics of a compressor having any rotor end profile. However, the author uses a SRM-D standard profile to demonstrate the geometrical features.

The inflow and outflow flow rate of the working medium is influenced by the shape (size) and location of the suction and discharge ports. The ammonia-water enters the compressor working cavity through the suction port and leaves through the discharge port at higher pressure. One lobe in the female rotor was marked (in black). This lobe and the corresponding cavity are taken as reference.

Table 4.1: Geometrical Characteristics used by Zaytsev (2003) for Compressor Development

Distance between rotor axes (mm)	77.07
Diameter of male rotor (mm)	104.9
Diameter of female rotor (mm)	80
Number of male rotor lobes	5
Number of female rotor lobes	6
Length of the rotors (mm)	172.6
Wrap angle of the male rotor (°)	313.7
Maximum Volume/cavity (mm^3)	135000

Table 4.2: Geometrical Characteristics used by Tang (1995) for Compressor Development

SRM D standard Profile	
Bore diameters (equal) (mm)	204
Number of male rotor lobes	4
Number of female rotor lobes	6
Length/diameter ratio	1.65
Length of the rotors (mm)	336.6
Wrap angle of the male rotor (°)	300
Maximum Volume/cavity (mm^3)	1600000

4.1.1. Compressor Cavity Volume

As the two rotors mesh into each other, a cavity is formed between the meshing surfaces and the compressor housing. This cavity volume changes during an entire compression process as the driven (male) rotor turns. This is the control volume used in the thermodynamic model of the compressor. Hence, a volume curve can be developed which is simply the relation between this compressor cavity and the male rotor angle.

On turning the compressor for one complete cycle, that is, suction then compression followed by discharge, it was observed that the cycle takes 852°of the male rotor angle. Hence, the volume curve (Figure 4.1) was developed using the known maximum volume of a cavity.

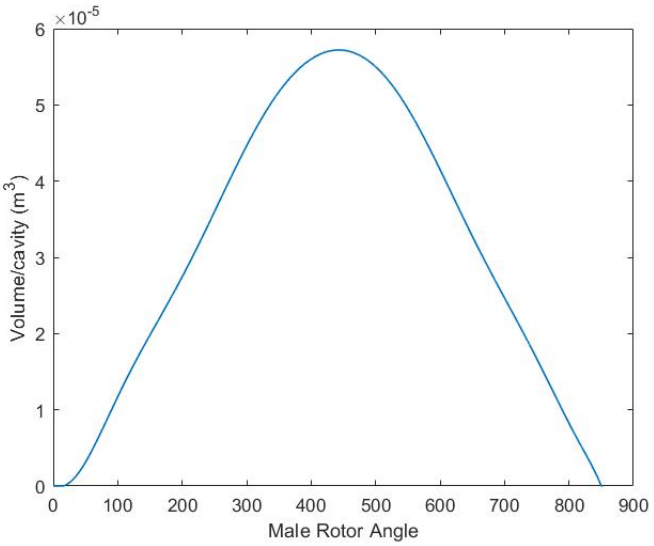

Figure 4.1: Volume Curve developed in this study. It takes 852°for a complete compression cycle during which a maximum volume of 57200 mm^3 is reached.

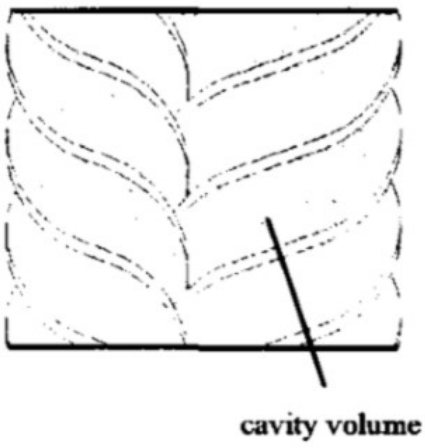

Figure 4.2: Compressor Cavity formed by the meshing surfaces of the male and female rotors (Zaytsev, 2003).

Figure 4.3 shows the volume curves developed by Zaytsev (2003), Tang (1995) and the curve developed in this study. Zaytsev (2003) based it on an analytical relation between the volume *V* and the boundary surface *S* given in Equation 4.3 where $\vec{n}$ is the unit vector and $\vec{r}$ is the vector from coordinate origin to the surface. Tang (1995) uses the integral of the cross-sectional area to calculate the cavity volume. The cross-sectional area is the area bound by the rotor ends and the housing bores. There can be seen a peak in the curve. This maximum of the volume curve is the maximal volume of the compressor cavity (V_{max}). The volume curve developed by Tang (1995) is much larger than those developed in this study and by Zaytsev (2003).

$$V = \frac{1}{3} \oint_S \vec{n} \cdot \vec{r} dS \tag{4.3}$$

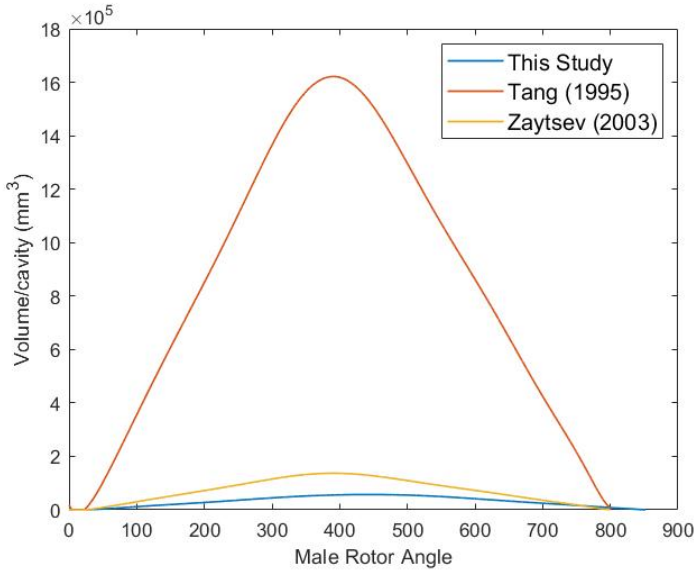

Figure 4.3: Volume Curve developed by Zaytsev (2003), Tang (1995) and in this study. The maximum volume in a cavity for the study done by Tang (1995) is much larger in comparison to the other two curves.

4.1.2. Suction Phase

The compressor has two major ports: Suction and Discharge. The working fluid enters the compressor cavity through the suction port and leaves through the discharge port. The port areas fluctuate as a function of the male rotor angle. The areas of these ports, along with their positions determine the suction and discharge phase in the compression process and also influence the flow rate of the working fluid. Hence, this impacts the efficiency of the compressor.

The suction port usually consists of an axial port and a radial port. Adding the radial port to the suction port greatly increases the port area and reduces flow losses (Zaytsev, 2003). Usually the discharge port has a radial port only for compressors with small or medium built-in volume ratios.

Figure 4.5 shows the position of the rotors at the start of the suction phase. The reference female lobe is at an angle of -45°.

Figure 4.6 shows the position of the rotor when the compressor cavity is open to the endplate. This is at an angle of +205°. Now the compressor starts reaching its maximum volume which it will reach an angle of +239°. This is when the reference rotor lobe is aligned with the rotor axis line.

Figure 4.7 shows the position of the rotor when the compressor cavity is no longer open to the endplate on the suction side. From the figure on the right, the reference lobe cannot be seen since it

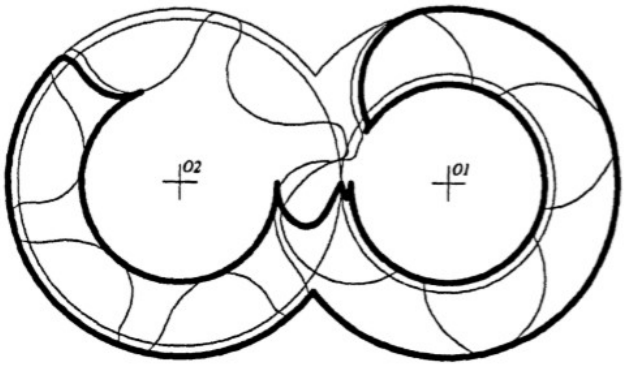

Figure 4.4: An axial suction port is highlighted for a 6-4 twin-screw compressor used by Tang (1995)

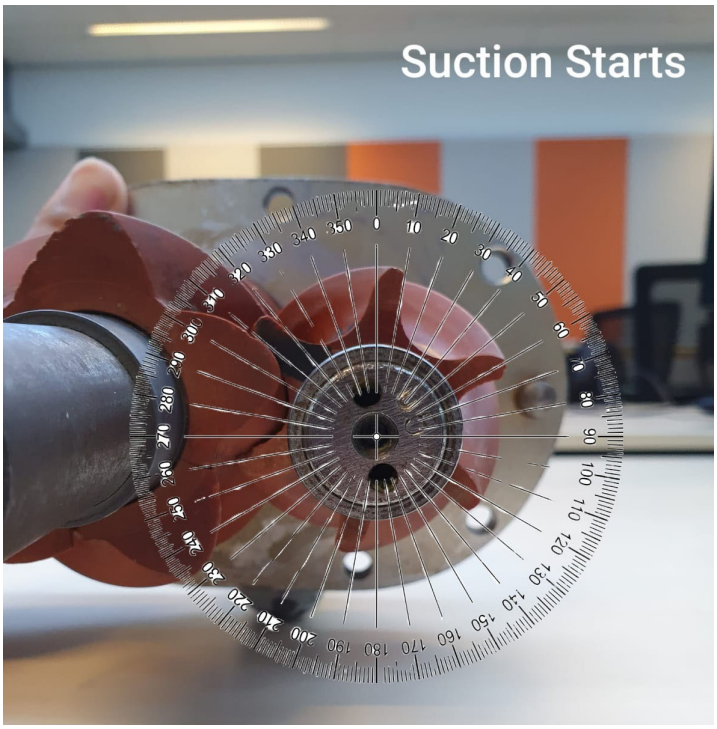

Figure 4.5: The rotation position of the female rotor as the suction phase begins.

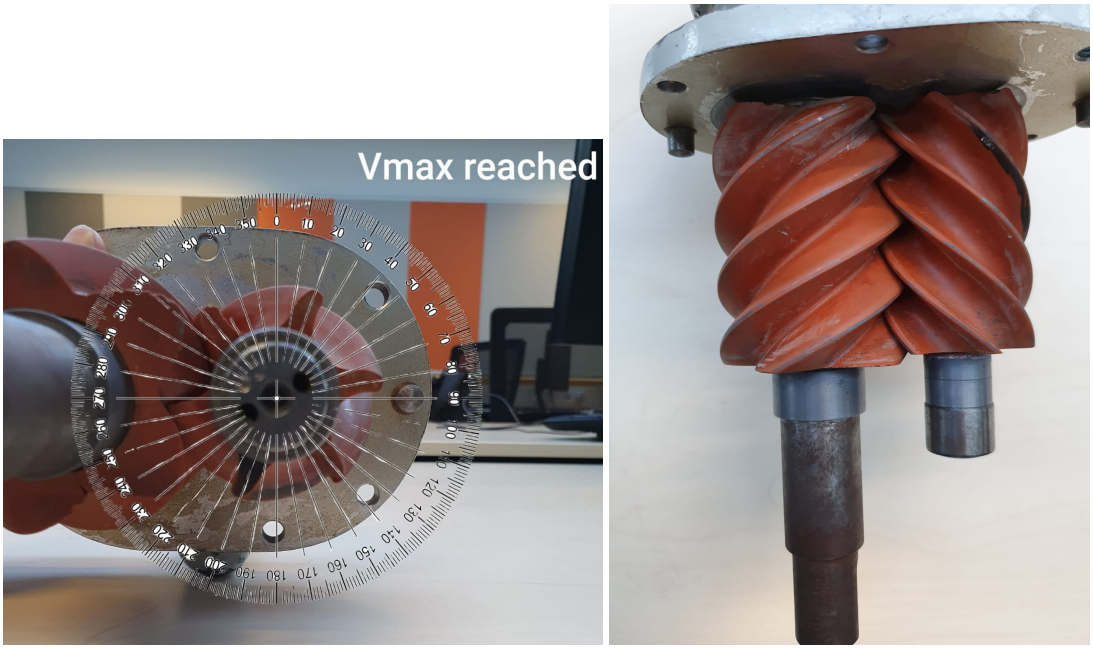

Figure 4.6: The rotation position of the female rotor the cavity is open to the endplate.

has turned to the discharge side of the endplate. The maximum volume of the compressor cavity is completely lost to the suction side. This is seen when the following lobe of the cavity has crossed the centre line of the rotor. The female rotor angle is then +295°. This marks the end of the suction phase.

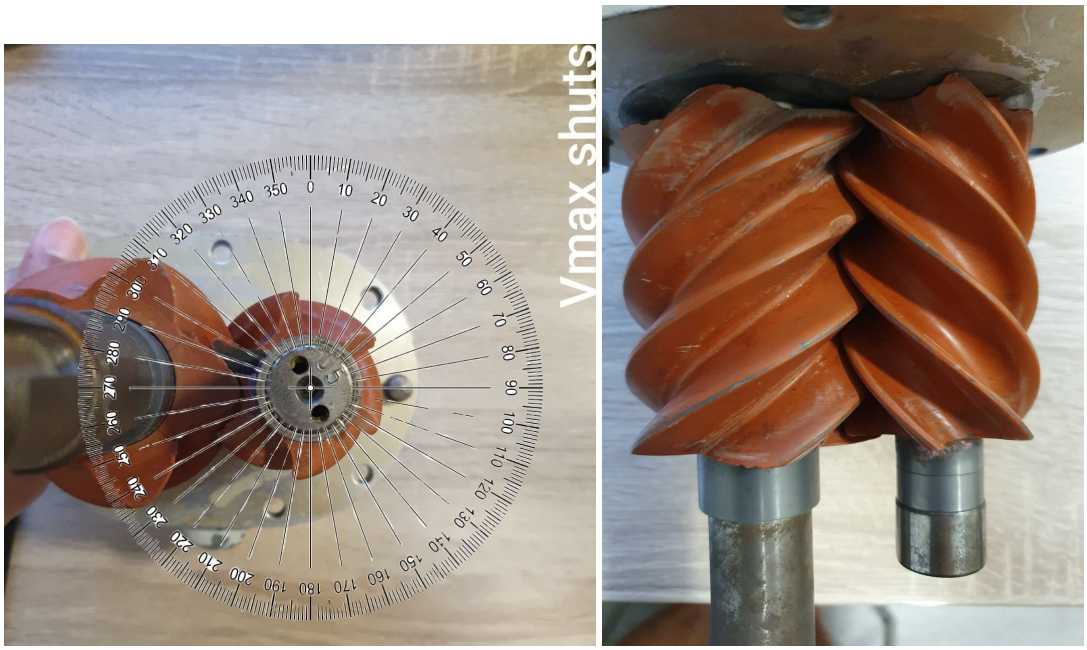

Figure 4.7: The rotation position of the female rotor when the compressor cavity has crossed the suction side.

Table 4.3 gives a summary of the suction phase location.

Table 4.3: Corresponding male rotor angle for suction phase

Event	Measured Female Rotor Angle	Female Rotor Angle	Male Rotor Angle
Suction starts	-45°	0°	0°
Cavity open to endplate	+205°	250°	375°
V_{max}	+239°	284°	426°
Cavity closed to endplate on suction side	+295°	340°	510°

There are two suction ports in the twin-screw compressor: the axial suction port and the radial suction port. Figure 4.8 describes the size and location of the two suction ports. The size of the suction ports has been taken from Zaytsev (2003) and Tang (1995). The radial suction port is open until an angle of 510°of the male rotor.

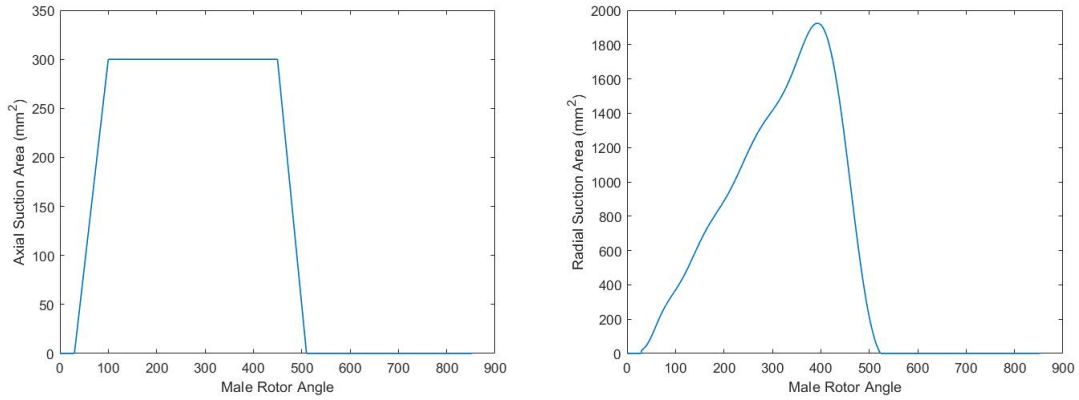

Figure 4.8: Suction Ports Size and Location. Axial Suction Port (Left), Radial Suction Port (Right)

The axial port areas (suction and discharge) connected to the cavity are found by integrating the contour along the port and cavity boundaries (Zaytsev, 2003).

Theoretically, there exists only one suction stop angle on the female rotor side given by equation 4.4. If the suction stop angle is larger or smaller than this angle, it could result in a slight loss in the indicated and volumetric efficiencies (Tang, 1995).

$$\varphi_{2,suc} = \varphi_{1,suc}\frac{z_1}{z_2} + \frac{360^\circ}{z_2} \tag{4.4}$$

Figure 4.9 and Figure 4.10 show the comparison of the axial and radial suction port sizes as a function of the male rotor angle respectively. The relative axial suction port size is larger than the axial suction port size used by Zaytsev (2003) and Tang (1995). However, the relative radial suction port size used in this study is equal to the port size used by Tang (1995) whereas the port size used by Zaytsev (2003) is much larger.

4.1.3. Compression Phase

Table 4.4 shows the location of the compression phase. The compression phase starts when the following lobe has crossed the center line of the rotor, that is, the compression cavity is no longer on the

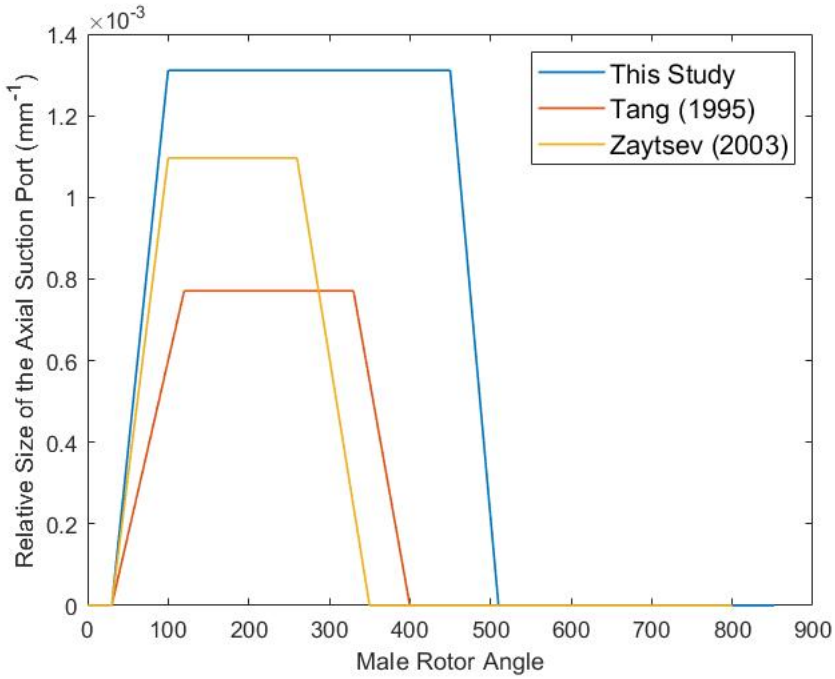

Figure 4.9: The relative axial suction port size for the current study compared with the work done by Tang (1995) and Zaytsev (2003) as a function of their respective male rotor angles. The axial suction port area in each study is divided by its respective total volume (maximum volume times the number of male rotor lobes)

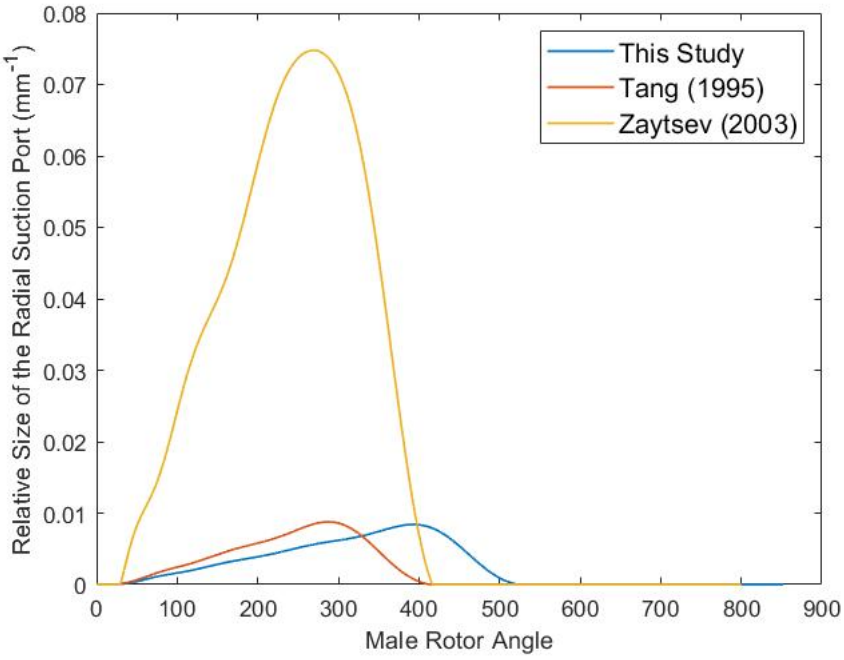

Figure 4.10: The relative radial suction port size for the current study compared with the work done by Tang (1995) and Zaytsev (2003) as a function of their respective male rotor angles. The radial suction port area in each study is divided by its respective total volume

suction side of the compressor. The compression phase ends when the considered lobe (marked in black) just reaches the discharge port.

Table 4.4: Corresponding male rotor angle for compression phase

Event	Measured Female Rotor Angle	Female Rotor Angle	Male Rotor Angle
Compression starts	+295°	340°	510°
Compression ends	+433°	478°	717°

4.1.4. Discharge Port

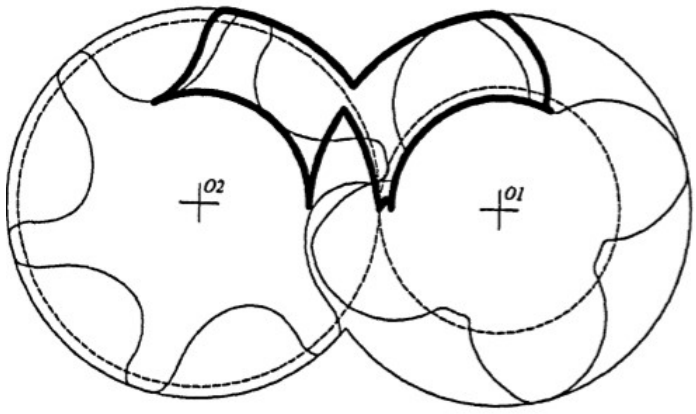

Figure 4.11: Example of an Axial Discharge Port (Tang, 1995).

Figure 4.12 describes the discharge port opening. As can be seen from the figure on the right, the reference lobe just reaches the discharge port opening of the compressor. The discharge port opens at +73°of the female rotor. One complete rotation has already been completed. Hence, the female rotor angle at which the discharge port opens is +433°.

Figure 4.13 shows the rotor position when the discharge port shuts completely. This occurs when the entire compressor cavity which is considered has been shut off to the discharge port by the following compressor cavity. This occurs at a measured angle +163°of the female rotor, that is, +523°from the reference position.

Table 4.5 summarizes the discharge phase of the compression cycle.

Table 4.5: Corresponding male rotor angle for discharge phase

Event	Measured Female Rotor Angle	Female Rotor Angle	Male Rotor Angle
Discharge starts	+433°	478°	717°
Discharge ends	+523°	568°	852°

The discharge port size has been measured physically on the compressor. The compressor has one axial discharge port and no radial discharge port. The port size is approximately 416 mm^2. Figure

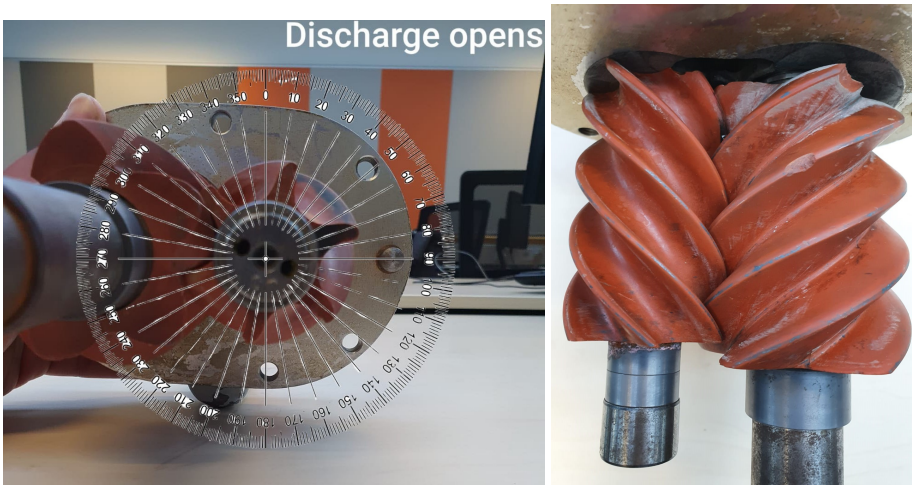

Figure 4.12: Left: The rotation angle of the female rotor when the discharge port opens. Right: The considered lobe just touches the discharge port. It may appear that the lobe is a few degrees ahead of the port, but the rotor tip being chipped has been taken into consideration.

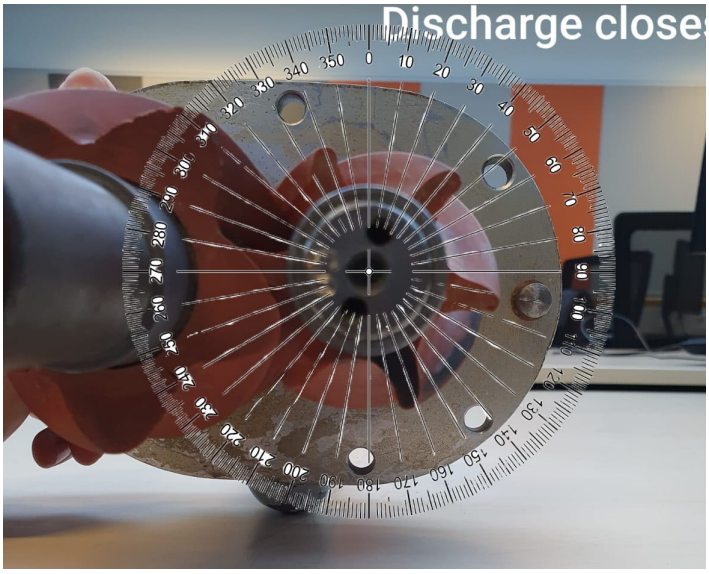

Figure 4.13: The rotor position when the discharge port closes.

4.14 shows the discharge port size and location.

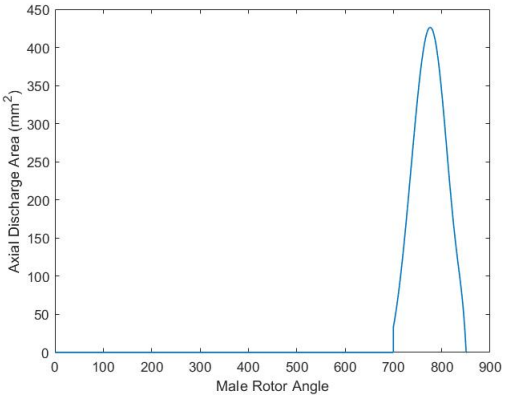

Figure 4.14: Discharge port curve showing the location and size of the port.

The axial suction port area is much larger than the axial discharge port area. This reduces suction resistance and is further reduced by a radial suction port since its area is approximately one order of magnitude larger than that of the axial suction port. Discharge port resistance can be reduced by a radial discharge port. For refrigeration, slide values are added to the compressors to adjust the capacity. Hence, the shape and subsequently the area of the radial discharge port can be adjusted according to the load requirements. Figure 4.15 shows the relative axial discharge port sizes of the three studies as a function of the respective male rotor angles.

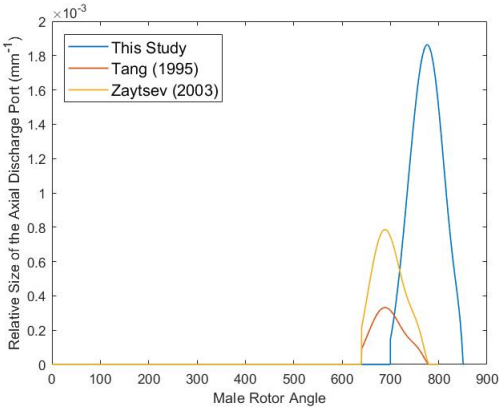

Figure 4.15: The relative axial discharge port size for the current study compared with the work done by Tang (1995) and Zaytsev (2003) as a function of their respective male rotor angles. The axial discharge port area in each study is divided by its respective total volume

4.1.5. Leakage Path Estimation

Clearances must be maintained between the rotor grooves and the compressor housing to compensate for thermal expansion, force deflection and machining tolerance. Although the clearances are small, the working fluid may still leak out. This affects the efficiency of the compressor (Chamoun et al., 2013).

Fleming and Tang (1995) identified six leakage paths present in twin screw compressors when considering a cavity volume:

1. The contact line between the male and female rotors. The working fluid leaks to the suction cavity from compression cavity across the contact line.

2. The sealing line between the rotor tips and housing bores. The working fluid leaks from the considered cavity across the sealing line to the trailing cavity at suction pressure. It also leaks from the discharge region (leading cavity) to the considered cavity across the tip-to-bore sealing line.

3. The cusp blow hole. The working fluid leaks to suction pressure (trailing cavity) from the considered cavity. It can also leak from the leading cavity to the cavity under consideration.

4. The compression-start blow hole. This blow hole exists at the beginning of compression for about 30°- 40°of the male rotor. The working fluid leaks from the cavity just starting compression to the cavity at suction pressure.

5. The clearance between the end plate and rotor end face at the suction end. During the early stages of the compression process, the working fluid leaks to the suction pressure.

6. The clearance between the end plate and rotor end face at the discharge end. The working fluid leaks to the trailing cavity from the considered cavity. Also, during the end of the compression process and during the discharge process the working fluid can leak to suction pressure directly.

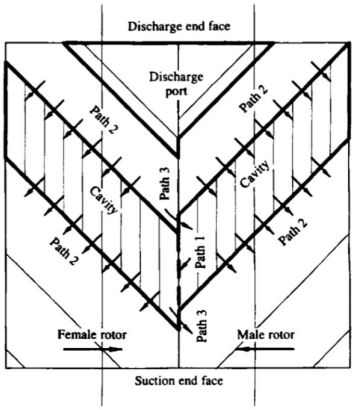

Figure 4.16: View of the leakage paths from the high pressure side. Here, the leakage through the contact line, sealing line and housing cusp blow hole is illustrated (Paths 1,2 and 3) (Fleming and Tang, 1995)

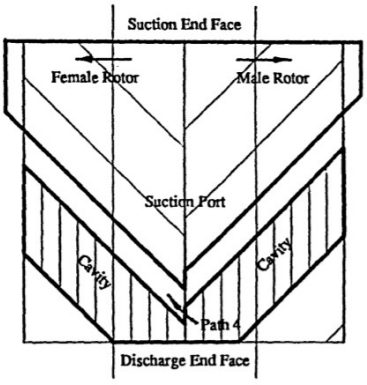

Figure 4.17: View of the leakage paths from the low pressure side. Here, the leakage through the compression start blow hole is illustrated (Path 4) (Tang, 1995)

The leakage size and locations used in the model are given in this section. Zaytsev (2003) and Tang (1995) estimated the leakage area for compressors which were considerably larger in volume and size. Hence, Guðmundsdóttir (2018) used scale factors for each leakage path. Table 4.6 shows

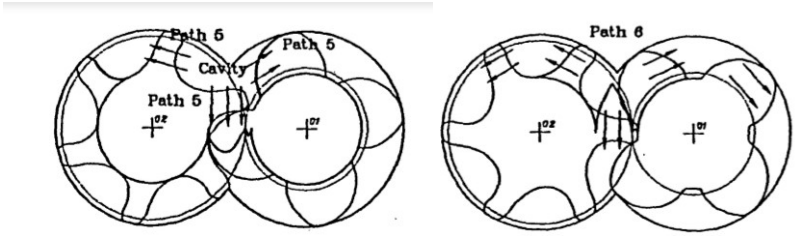

Figure 4.18: Left: View of the leakage paths from the suction end illustrating the leakage from Path 5. Right: View of the leakage paths from the discharge end illustrating the leakage from Path 6 (Tang, 1995)

the leakage scale factors used for each leakage path.

Table 4.6: Scale Factors used for Leakages

Leakage Path	Scale Factor
Contact Line	0.3
Sealing Line (Male Rotor Tip)	0.08
Sealing Line (Female Rotor Tip)	0.08
Housing Cusp Blow Hole	0.5
Compression Start Blow Hole	2
Rotor End Face Sealing Line	4

4.1.6. Contact Line

Path 1: Leakage through the contact line is a major path of leakage. This leakage area is calculated by multiplying the contact line length with the clearance between rotors. Figure 4.19 (left) shows the contact line leakage length for the twin-screw compressor. Leakage through the contact line can occur throughout the compression process, however it is assumed here that only at an angle 350°of the male rotor, enough driving force (pressure gradient) is generated for any noticeable leakage. A contact line length of 32 mm was measured on the twin-screw compressor.

Furthermore, in order to compare the size of the leakage through the contact line between the three studies, the length of the contact line is divided by its respective rotor length. Figure 4.19 (left) shows this comparison. Here, the dimensionless contact line length of this study is smallest in comparison to the one used in Tang (1995) and Zaytsev (2003). By comparison, Tang (1995) has the largest contact line length while Zaytsev (2003) is closer to this study.

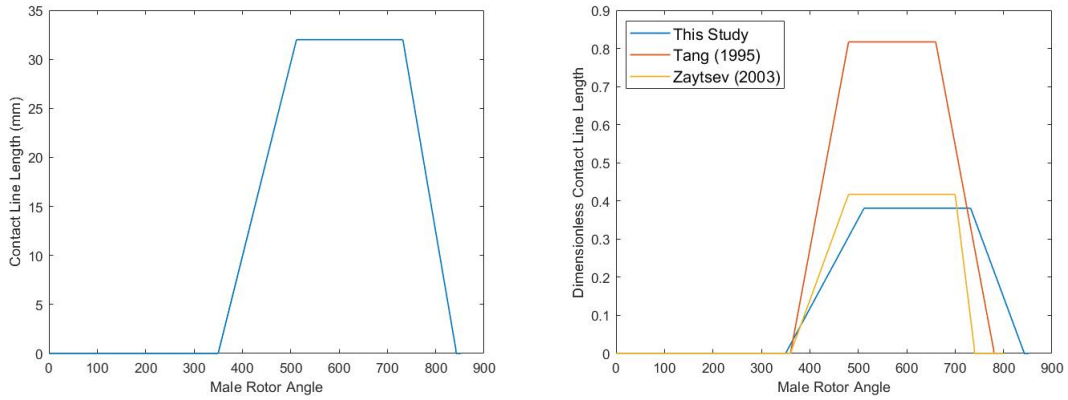

Figure 4.19: Left: Path 1: Contact Line Length as a function of the male rotor angle; Right: Non-Dimensional Contact Line Length for the current study compared to the studies done by Zaytsev (2003) and Tang (1995). As can be seen from the figure, the dimensionless contact line length for Tang (1995) is largest among the three.

4.1.7. Sealing Line

Path 2: The sealing line leakage area can be calculated multiplying the sealing line length with the clearance. Both the rotors have sealing lines with different lengths due to the difference in size and number of lobes. Figure 4.20 shows the leakage area developed as a result of the leakages across these sealing lines. The maximum leakage is taken until 426°, that is, until the maximum volume in the cavity is reached. As the rotor turns, the volume decreases and so does the sealing line leakage.

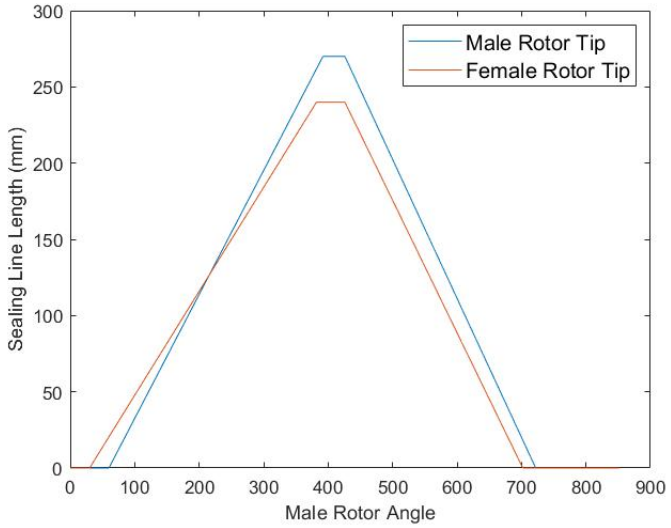

Figure 4.20: Path 2: Sealing Line Length as a function of the male rotor angle.

The considered cavity is bound by four sealing lines : the trailing cavity's sealing line and the leading cavity's sealing line for both the rotors (Zaytsev, 2003). On comparing the sealing line lengths between the three studies as shown in Figure 4.21, we can see that Tang (1995) has a smaller leakage length whereas the leakage length for the current study and Zaytsev (2003) are comparable.

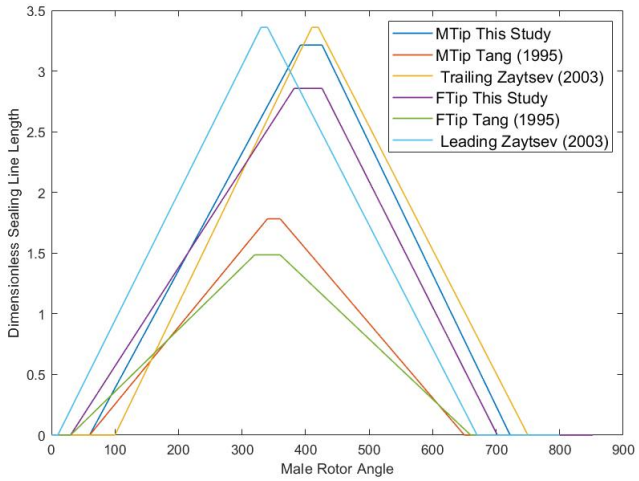

Figure 4.21: Sealing Line lengths divided by the respective rotor length as a function of the male rotor angle for the three different studies. Here, *MTip* and *FTip* refer to the sealing lines at the male and female rotor tips.

4.1.8. Blow Holes

Paths 3 & 4: Blow holes are triangular shaped 3-D surfaces (Figure 4.22). They are bound by the rotor surface adjacent to the rotor tips and by the compressor housing cusp. The blow holes at the high pressure side are called cusp blow holes. The blow holes at the low pressure side are called the compression-start blow holes. According to Tang (1995), for a SRM-D standard profile with a wrap angle of 300°, the compression-start blow hole causes the volumetric efficiency to reduce by 1%. Figure 4.23 (left) shows the housing cusp blow hole leakage area. This blow hole connects neighbouring cavities throughout the compression process. However, it is assumed that the driving force for the leakage via the housing cusp is only attained at 400°and leakage then occurs until the end of the compression process.

The compression start blow hole exists during the suction phase and continues until the early stage of compression (Zaytsev, 2003). During suction, the neighbouring cavities have a very small pressure gradient. Hence, leakage would be negligible. A noticeable leakage flow only exists at the beginning of the compression phase, hence the name. Figure 4.23 (right) shows the compression start blow hole leakage area.

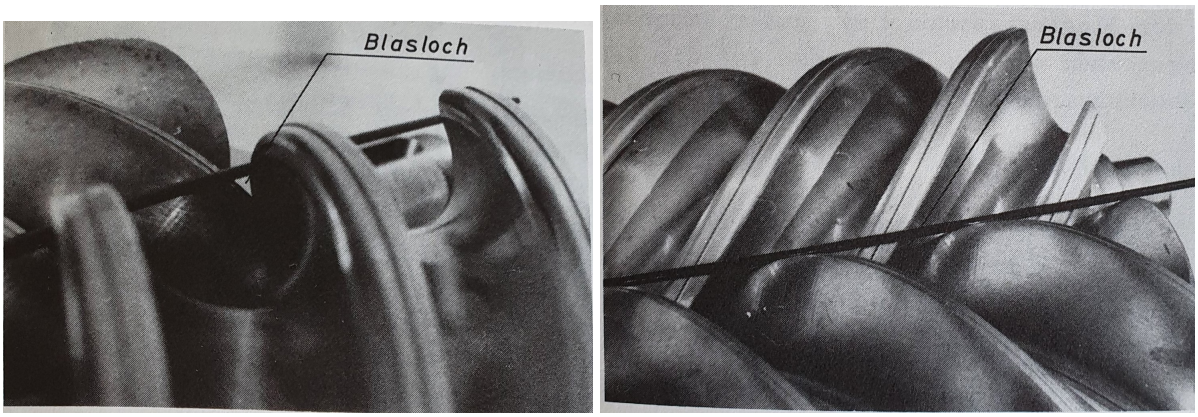

Figure 4.22: Left: Blow Hole on the discharge side; Right: Blow Hole on the suction side of the twin-screw compressor (Rinder, 1979)

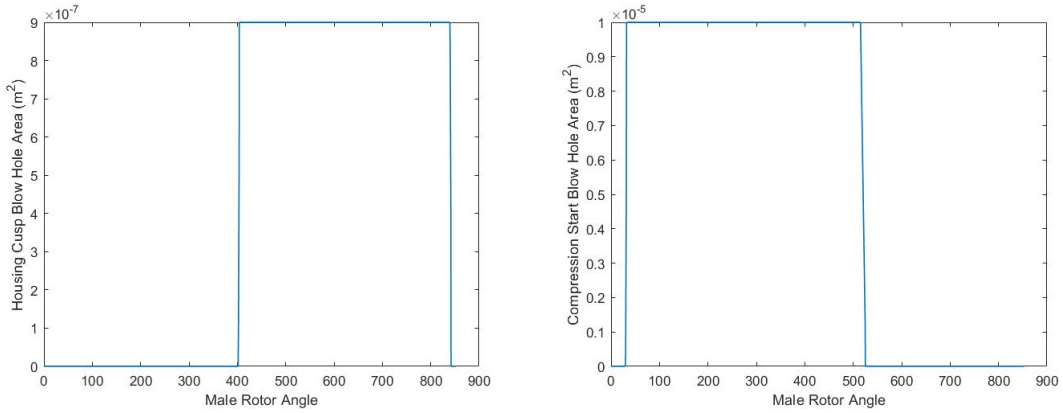

Figure 4.23: Left: Housing Cusp Blow Hole Leakage Area as a function of the male rotor angle; Right: Compression Start Blow Hole Leakage Area as a function of the male rotor angle.

Figure 4.24 shows a comparison between the blow hole leakage areas for the three studies. In comparison, this study has the largest housing cusp blow hole area while Tang (1995) has the smallest. The comparative compression start blow hole area for Zaytsev (2003) is the largest among the three.

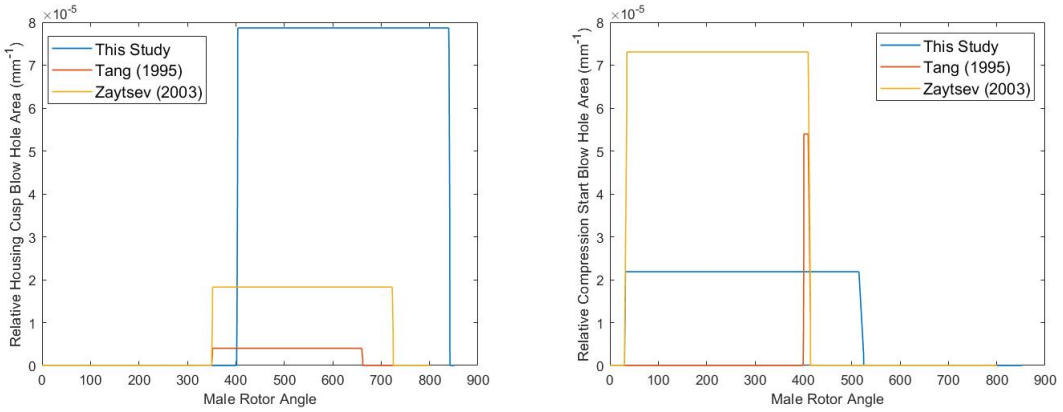

Figure 4.24: The Relative Housing Cusp Blow Hole (left) and Compression Start Blow Hole (right) Leakage Areas as a function of the male rotor angles for the three studies. The blow hole areas have been divided by the total volume for the three studies respectively.

4.1.9. Rotor End Face Sealing Line at the Discharge End

Path 5 & 6: Leakages through the suction and discharge end clearances. Zaytsev (2003) ignores the leakage through the suction end clearance due to the small pressure difference between cavities which are connected to the suction end. Figure 4.25 shows the leakage paths through the discharge end clearances. The white arrows show the leakage from the leading cavity to the trailing cavity while the black arrows show the leakage from the cavity where discharge is taking place directly to the suction cavity.

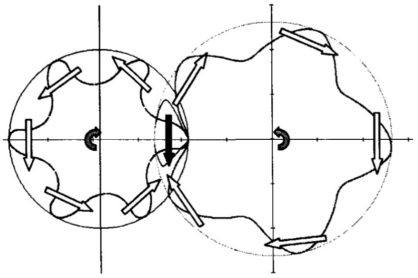

Figure 4.25: Leakage paths of the discharge end clearance (Zaytsev, 2003)

The compressed process medium (ammonia-water) leaks from the leading cavity to the trailing cavity at the discharge end. The leakage area formed is shown in Figure 4.26 (left) as a function of the male rotor angle. The length of the sealing line was measured in the available compressor to be 26 mm.

Furthermore, the process medium also leaks from the considered compressor cavity volume undergoing discharge directly to suction pressure. The length of the sealing line between the discharge and suction ends of the compressor was measured to be 13 mm. The leakage area formed due to this leak is shown in Figure 4.26 (right) as a function of the male rotor angle.

In order to compare the leakages at the discharge end, the leakage lengths have been made dimensionless by dividing them with the respective rotor diameters of the three studies. Figure 4.27 (left) shows this comparison for the leak from the leading to the trailing cavity while Figure 4.27 (right) is for the leak from the high pressure (discharge end) directly to the low pressure side (suction end).

Wang et al. (2019) also analyzed the leakages in a water lubricated twin-screw air compressor. They developed a model of the working process which calculated the effects of the various leakage paths on the compressor performance. The six paths of leakages are compared here. The volumetric efficiency reduces as the rotation speed increases for each leakage path. It is concluded that leak-

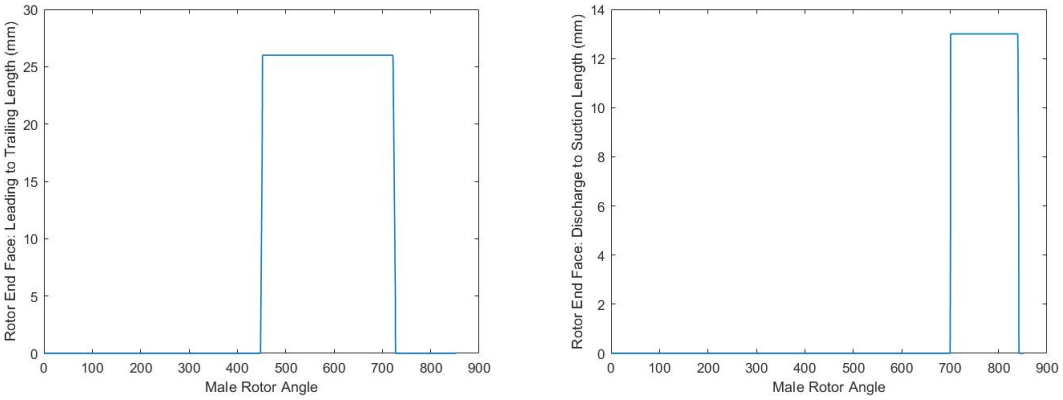

Figure 4.26: Left: Leakage Area for the leak from the leading cavity to the trailing cavity; Right: Leakage from the cavity volume in Discharge phase to the Suction phase directly

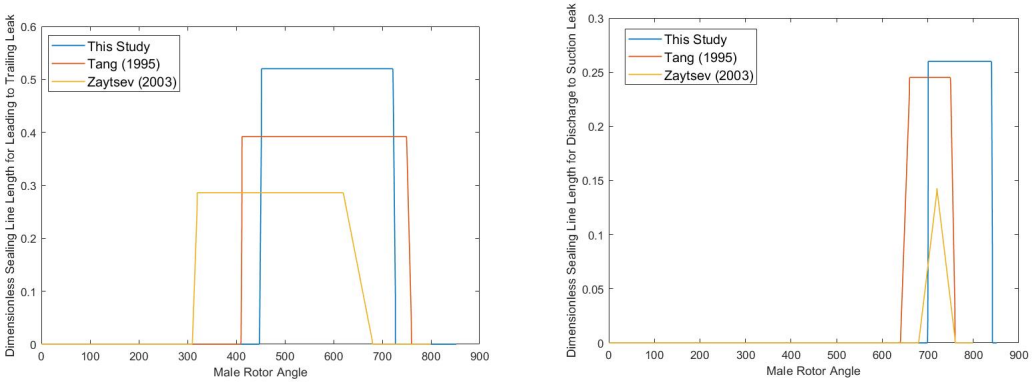

Figure 4.27: Left: End plane clearance lines lengths for the discharge side for the leak from the leading to the trailing cavity as a function of the male rotor angle; Right: End plane clearance lines lengths for the discharge side for the leak from the discharge to the suction end as a function of the male rotor angle

ages through the discharge end-face clearance and rotor tip clearance have a significant impact on the performance of the compressor while the effect of the other leakage paths can be neglected. Also, increasing the rotation speed is an effective way to reduce the leakages.

4.2. Model Results

In order to systematically observe the effect of various parameters on the isentropic and volumetric efficiencies of the compressor, a base case is developed. The parameters for this base case are given in Table 4.7. The efficiencies achieved from the model for all datasets using this base case are given in Appendix D. Here, *MTip* and *FTip* refers to the male and female rotor tip sealing lines respectively.

Four rotational speeds are under study: 10320 rpm, 12910 rpm, 14205 rpm and 15500 rpm. For each rotational speed, datasets with the highest and lowest value of the isentropic efficiency for the base case are chosen to be evaluated further since they represent the trend of all other datasets in their respective rotational speed. As can be seen from Table D.1, for 10320 rpm, dataset 11 has the lowest isentropic efficiency (0.5762) while dataset 25 has the highest (0.6861). For 12910 rpm, dataset 23 has the lowest efficiency (0.6856) while dataset 12 has the highest efficiency (0.7325). For 14205 rpm, dataset 33 has the lowest efficiency (0.7065) while dataset 31 has the highest efficiency (0.7350). For 15500 rpm, dataset 39 has the lowest efficiency (0.7302) and dataset 40 has the highest efficiency (0.7399).

Table 4.7: Parameters of the Compressor Model that form the Base Case

Parameter		Value
Clearance (mm)	C	0.05
Flow Coefficient for Leakages	C_{fl}	1.2
Flow Coefficient for Suction	C_{fs}	0.9
Flow Coefficient for Discharge	C_{fd}	0.5
Contact Line Length (mm)	C_{line}	32
Sealing Line Length (mm)	*MTip* *FTip*	270 240
Housing Cusp Blow Hole Area (mm^2)	*HBHole*	18

4.2.1. Effect of Clearance

Three clearance values are evaluated: 0.05 mm (base case), 0.1 mm, 0.15 mm. The isentropic and volumetric efficiencies from these simulations can be found in Appendix D. Figure 4.28 shows the effect of clearances on the isentropic efficiency. The line with dots is for the runs with the lowest value of efficiency while the line with stars as data-points are for runs with the highest value of efficiency for a particular rotational speed. As can be expected, the larger the clearance, the greater the leakages and hence efficiency drops. The efficiency drops almost linearly for all datasets. The slope for dataset 11 (10320 rpm, lowest efficiency) reduces showing a reduced decrease when the clearance is increased from 0.1 mm to 0.15 mm. An 11% drop is seen when the clearance is increased to 0.1 mm and a 21% drop in isentropic efficiency is seen when the clearance increases to 0.15 mm from 0.05 mm.

Figure 4.29 shows the effect of increasing clearances on the volumetric efficiency. A similar trend is seen here. However, the volumetric efficiency reduces quicker for few datasets between clearance 0.1 mm and 0.15 mm than between 0.05 mm and 0.1 mm. The volumetric efficiency, on average,

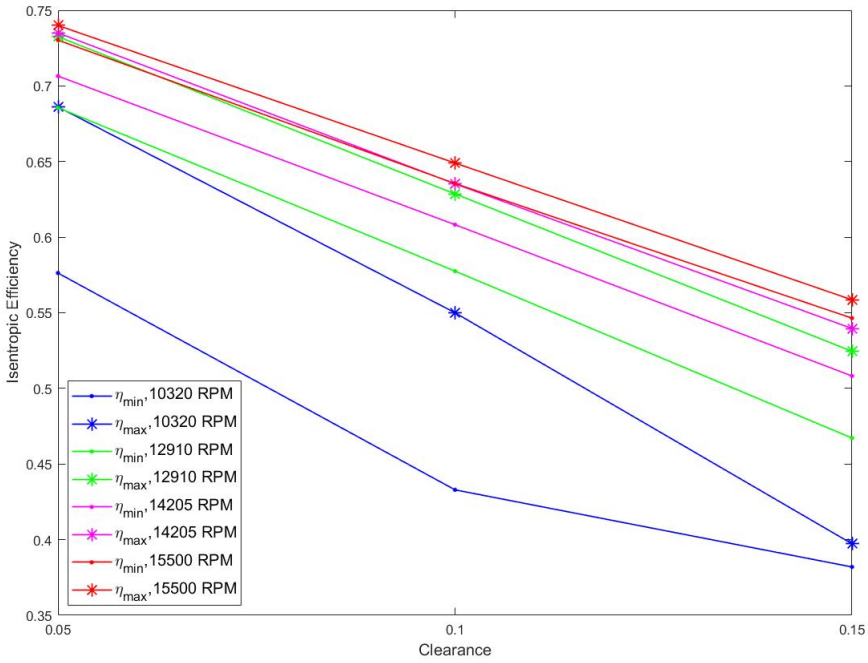

Figure 4.28: Effect of clearances on the isentropic efficiency of the compressor. An almost linear decrease in the isentropic efficiency is seen with increasing clearance.

drops 1.8% when the clearance is increased to 0.1 mm and 4.2% when it is increased to 0.15 mm. The effect of clearance on the volumetric efficiency is much smaller compared to its effect on the isentropic efficiency. The corresponding data is given in Appendix D.

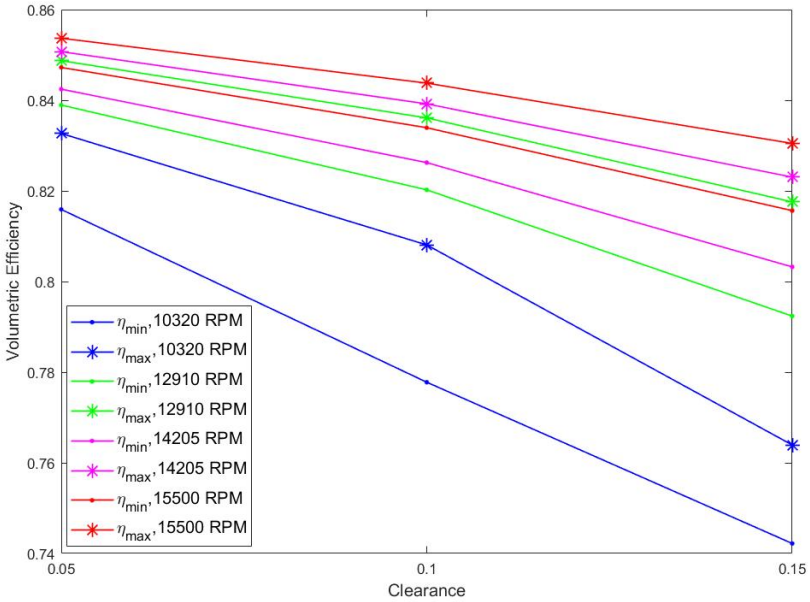

Figure 4.29: Effect of clearances on the volumetric efficiency of the compressor. The volumetric efficiency decreases as the clearance is increased.

4.2.2. Effect of Flow Coefficient for Leakages

The flow coefficient for leakages influences the mass flow rate through the leakage paths. Initially, this coefficient was set to 1.2. In this study, the effect of increasing the flow coefficient is seen. In Figures 4.30 and 4.31 the isentropic and volumetric efficiencies are plotted as functions of the flow coefficient of leakages varying it from 1.2 to 2.0 respectively. As is expected, greater leakage leads to lesser efficiencies. A decrease in the isentropic and volumetric efficiencies can be seen as the amount of ammonia-water lost due to leakages increases. However, this decrease is more significant in lower rotational speeds. The isentropic efficiency drops approximately 11.5% and the volumetric efficiency drops approximately 5% when the flow coefficient for leakages is increased from 1.2 to 2.0.

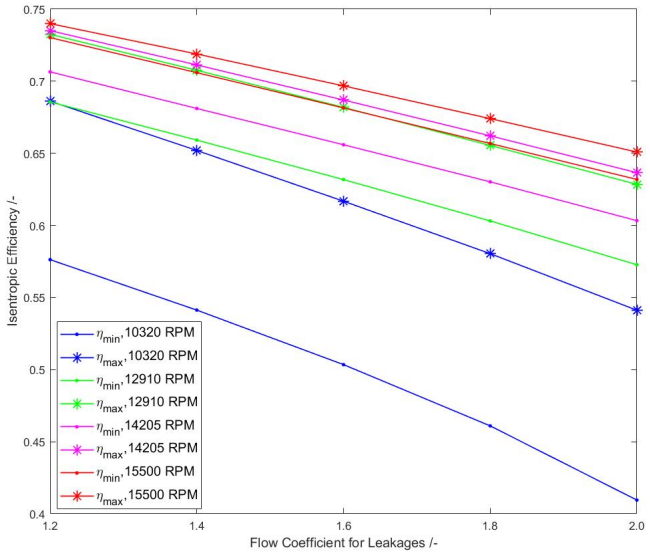

Figure 4.30: Effect of varying the flow coefficient for leakages on the isentropic efficiency of the compressor. Increasing the flow coefficient for leakages increases the mass flow rate of through the leakage and reduces the isentropic efficiency.

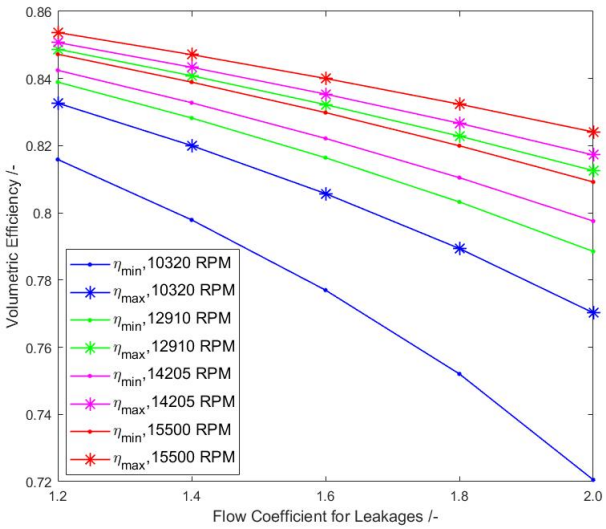

Figure 4.31: Effect of varying the flow coefficient for leakages on the volumetric efficiency of the compressor. The volumetric efficiency decreases as the flow coefficient for leakages increases.

4.2.3. Effect of Flow Coefficient for Discharge

The flow coefficient of discharge affects the amount of process medium flowing out of the compressor. Initially, it was set to 0.5. In this study, the flow coefficient is varied from 0.5 to 0.1. Figures 4.32 and 4.33 show the effect of varying this coefficient on the isentropic and volumetric efficiencies respectively.

In Figure 4.32, for the dataset with 10320 rpm and lowest efficiency (blue with dots), the isentropic efficiency first reduces on increasing the flow coefficient until 0.3, and then increases. A similar trend is seen for datasets with lowest efficiencies for 12910 rpm and 14205 rpm. For 15500 rpm, the isentropic efficiency first increases slightly when the flow coefficient is 0.2 and subsequently shows only slight variation. The volumetric efficiency remains unchanged with respect to the flow coefficient of discharge since it only depends on the suction mass flow rate.

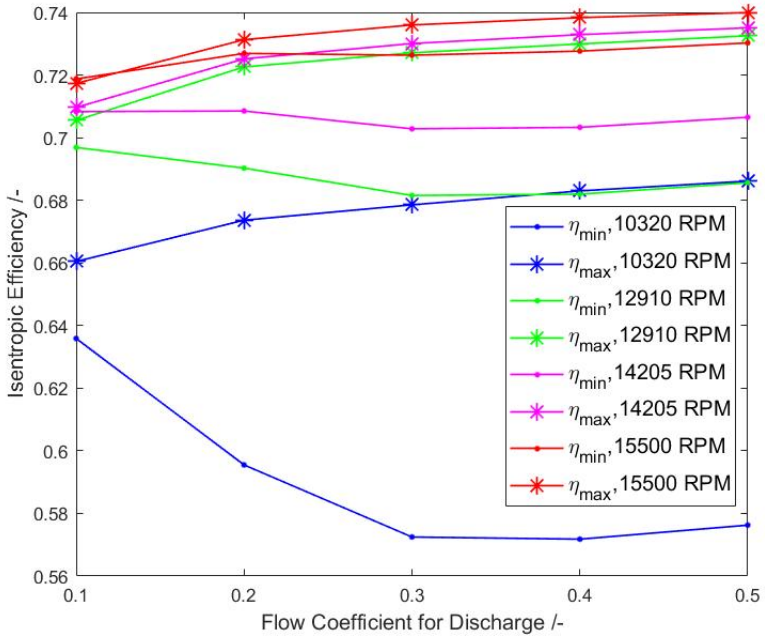

Figure 4.32: Effect of varying the flow coefficient for discharge on the isentropic efficiency of the compressor

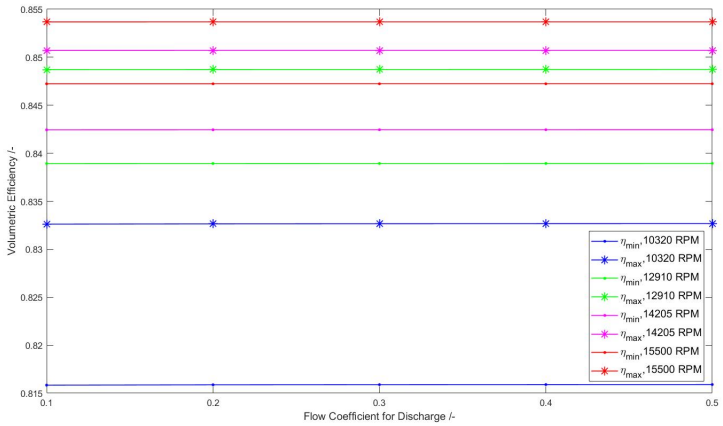

Figure 4.33: Effect of varying the flow coefficient for discharge on the volumetric efficiency of the compressor. The volumetric efficiency remains constant with respect to the flow coefficient for discharge.

4.2.4. Effect of Flow Coefficient for Suction

The flow coefficient of suction affects the amount of process medium flowing into the compressor rotor housing. Initially, this coefficient was set to 0.9. The flow coefficient has been varied from 0.1-0.9. In Figure 4.34, the isentropic efficiency increases from C_{fs} = 0.1 to 0.3 and then shows only slight increase until C_{fs} = 0.9. Figure 4.35 shows the volumetric efficiency of the compressor as a function of the flow coefficient for suction. The volumetric efficiency shows a greater increase from C_{fs} = 0.1 to 0.3 than from C_{fs} = 0.3 to 0.9. The isentropic efficiency drops approximately 5.5% and the volumetric efficiency drops approximately 2% when the flow coefficient for suction is reduced from 0.9 to 0.1.

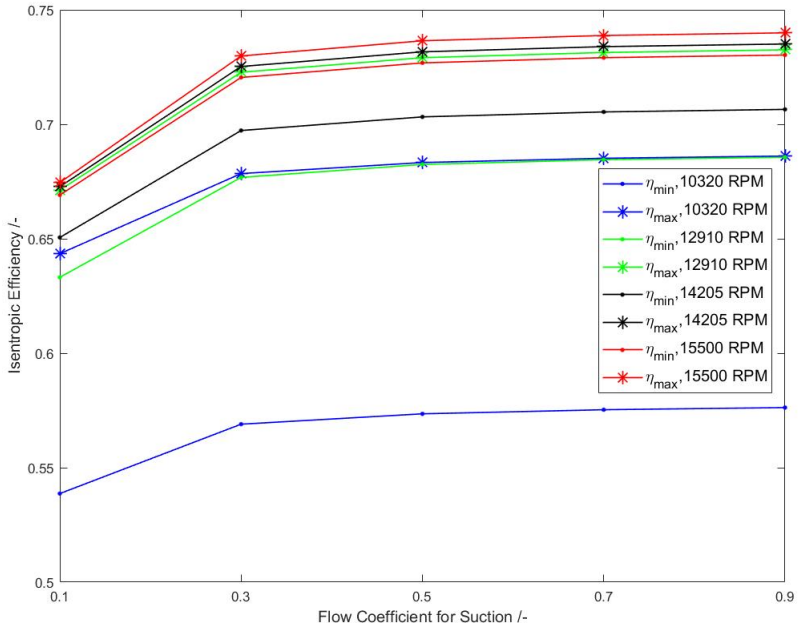

Figure 4.34: Effect of varying the flow coefficient for suction on the isentropic efficiency of the compressor. The isentropic efficiency decreases as a lower empirical flow coefficient for suction is used.

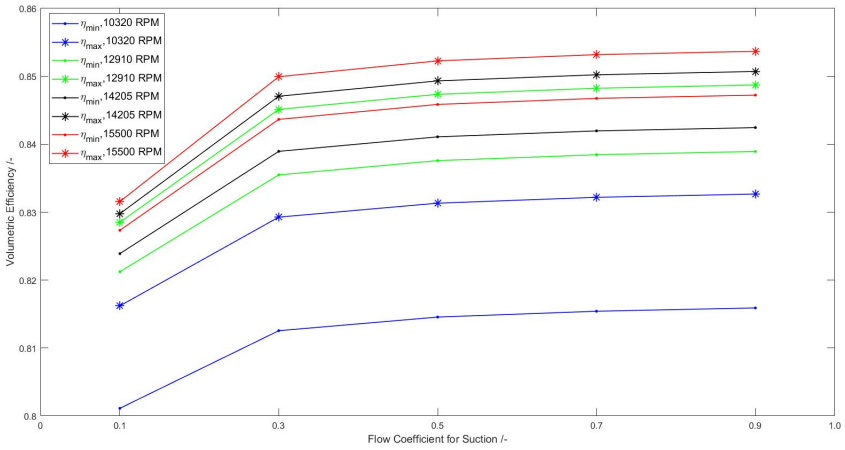

Figure 4.35: Effect of varying the flow coefficient for suction on the volumetric efficiency of the compressor. The volumetric efficiency decreases as a lower empirical flow coefficient for suction is used.

4.2.5. Effect of the Contact Line Length

The contact line length is one of the most significant leakage paths in the twin-screw compressor. For the base case, a measured length of 32 mm was used. In this section, the effect of varying the contact line from 20-70 mm on the efficiencies of the compressor is discussed. From Figure 4.36, it can be seen that the isentropic efficiency decreases as the contact line length increases due to greater leakage through this path. The same trend can also be seen for the volumetric efficiency in Figure 4.37. The isentropic efficiency drops approximately 1% and the volumetric efficiency drops approximately 0.13% when the contact line length is increased from 32 mm (base case) to 70 mm.

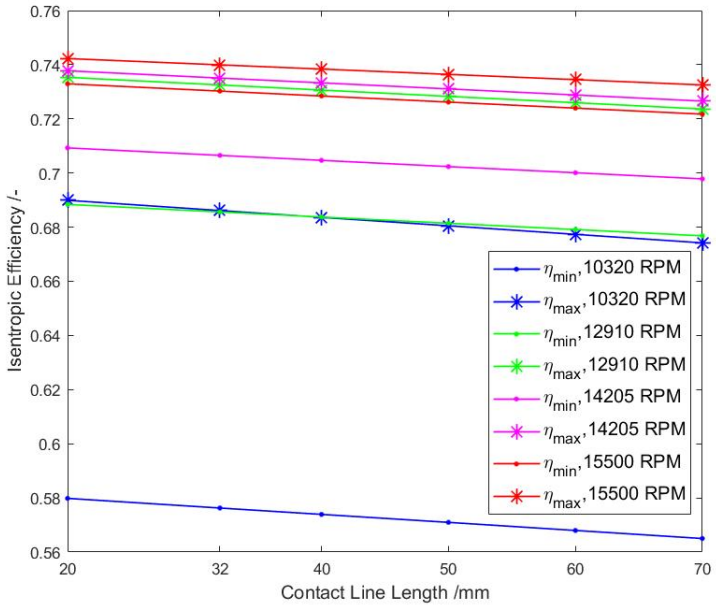

Figure 4.36: Effect of varying the contact line length on the isentropic efficiency of the compressor. The isentropic efficiency decreases as the contact line length is made larger.

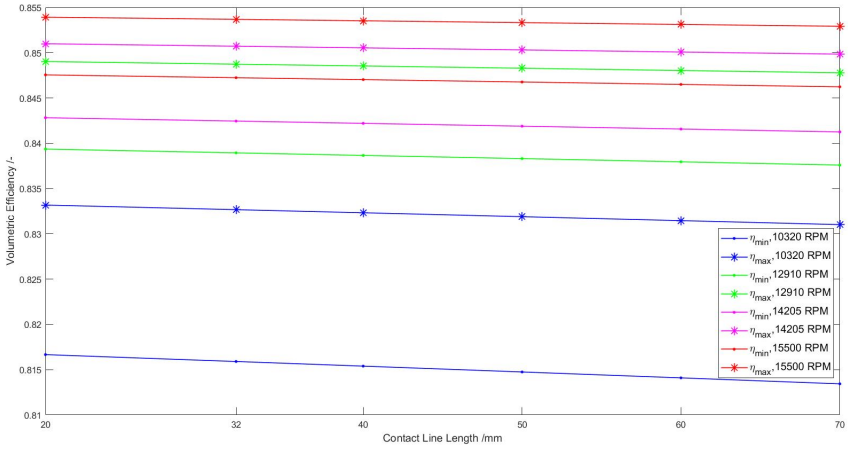

Figure 4.37: Effect of varying the contact line length on the volumetric efficiency of the compressor. The volumetric efficiency reduces slightly as the contact line length is made larger.

4.2.6. Effect of the Sealing Line Length

The rotor tip sealing lines lengths are between the tip of the male and female rotor and the housing bore. The male rotor tip sealing line length was varied from 160 mm - 320 mm and the female rotor tip sealing line length was varied from 120 mm - 280 mm. Both, the isentropic and volumetric efficiencies reduce as the clearance between the tip of the rotors and the housing bore increases as can be seen from Figures 4.38 and 4.39. The isentropic efficiency drops approximately 0.3% and the volumetric efficiency drops approximately 0.13% when the sealing line length is increased from 270 mm for the male rotor tip length and 240 mm for the female rotor tip length (base case) to 320 mm and 280 mm respectively.

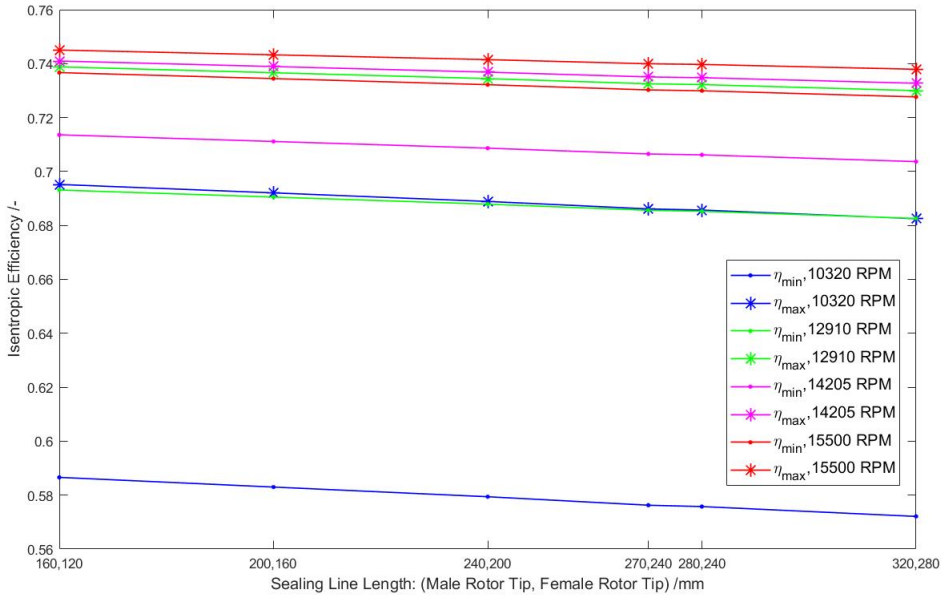

Figure 4.38: Effect of varying the sealing line lengths on the isentropic efficiency of the compressor. The isentropic efficiency decreases as the sealing line lengths are made larger.

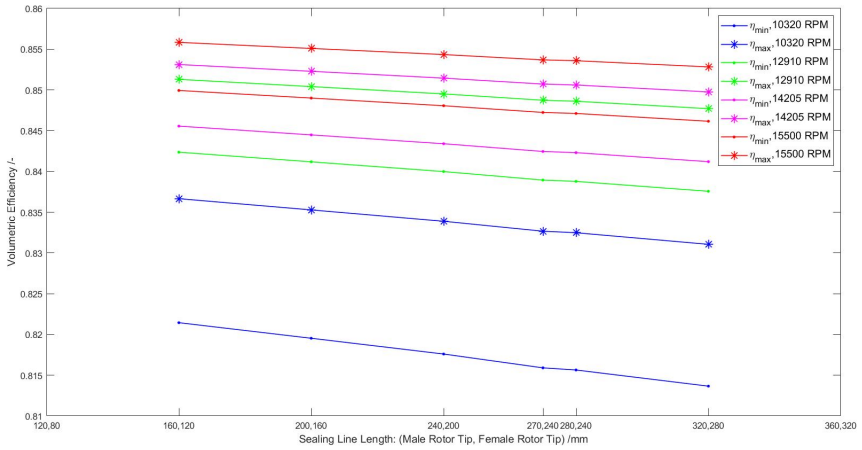

Figure 4.39: Effect of varying the sealing line lengths on the volumetric efficiency of the compressor. The volumetric efficiency decreases as the sealing line lengths are made larger.

4.2.7. Effect of the Housing Cusp Blow Hole Area

The housing cusp blow hole is another significant leakage path having a direct effect on the compressor performance. The blow hole area was varied between 10-40 mm^2. Figures 4.40 and 4.41 show that the isentropic and volumetric efficiencies decrease with increasing blow hole area. The isentropic efficiency drops approximately 1.8% and the volumetric efficiency drops approximately 0.4% when the housing cusp blow hole area is increased from 18 mm^2 (base case) to 40 mm^2.

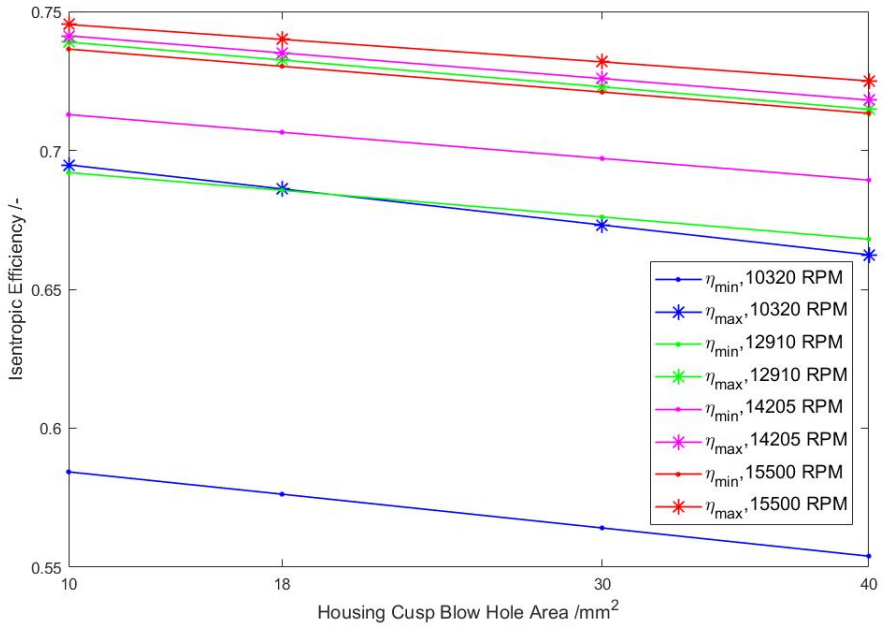

Figure 4.40: Effect of varying the housing cusp blow hole area on the isentropic efficiency of the compressor. The isentropic efficiency decreases as the blow holes area is made larger.

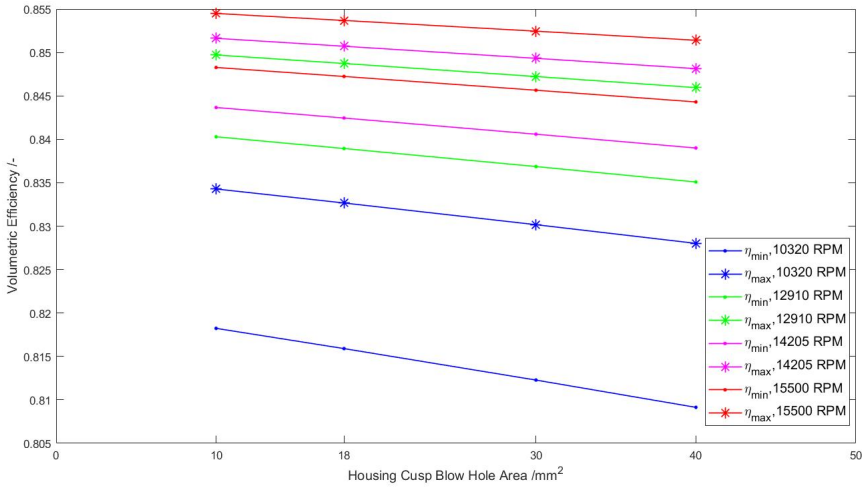

Figure 4.41: Effect of varying the housing cusp blow hole area on the volumetric efficiency of the compressor. The volumetric efficiency decreases as the blow holes area is made larger.

4.3. Validation

Now that the effect of all individual factors on the performance of the twin-screw compressor is noted, the next step is to see how this factors contribute together to the performance. Ideally, the efficiencies achieved with the model must be equal to the efficiencies achieved from experimentation. As can be seen from the graphs above, the model predicts higher efficiencies of the compressor. Hence, the first step in validation would be to observe the lowest possible efficiency from the model. This is done by using the values of the contributing factors at which the lowest efficiency for a dataset is achieved.

Figure 4.42 shows how the lowest efficiencies achieved by the model compare with the experimental efficiencies for a clearance of 0.05 mm (base case). The dotted line represents the ideal scenario in which $\eta_{\text{is,exp}} = \eta_{\text{is,model}}$. Above the dotted line is the area where $\eta_{\text{is,exp}} > \eta_{\text{is,model}}$ and below the dotted line is the region where $\eta_{\text{is,exp}} < \eta_{\text{is,model}}$. For the base case clearance and the lowest efficiency values of the other contributing factors, we see that only one dataset (# 25) is close to ideality, whereas the rest are below the dotted line. Taking a average of the datasets considered here, the model isentropic efficiency is approximately 23% higher than the experimental isentropic efficiency and 38% for the volumetric efficiency. This means that the lowest efficiency achieved from the simulations is still not low enough.

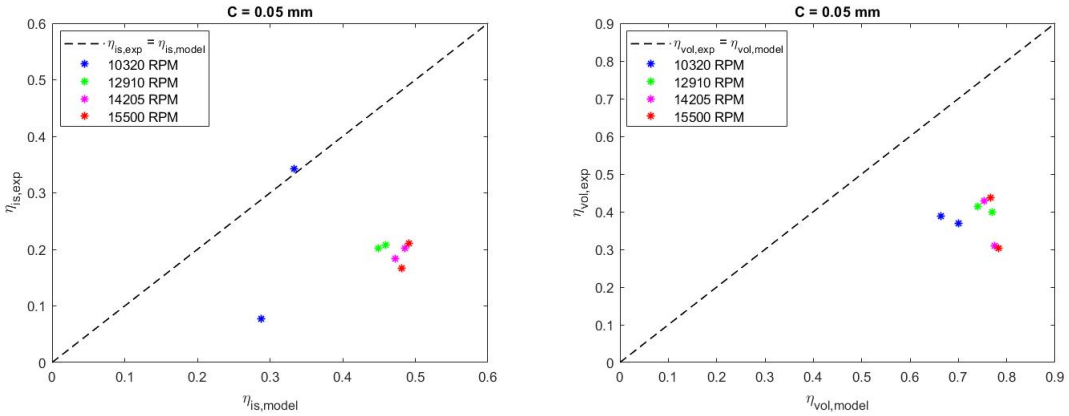

Figure 4.42: Left: Experimental Isentropic Efficiency versus the Isentropic Efficiency achieved from Simulations; Right: Experimental Volumetric Efficiency versus the Volumetric Efficiency achieved from Simulations, for a clearance of 0.05 mm

For dataset 25, the $\eta_{\text{is,exp}} \approx \eta_{\text{is,model}}$. This dataset was obtained at 10320 rpm, with an inlet vapour quality of 0.56 and pressure ratio of 3.08. These values are within the determined optimum working range of the compressor. For the same rotational speed, dataset 11 is still far from ideality. This dataset has an inlet vapour quality of 0.88 and a pressure ratio of 1.95, clearly out of the determined optimum working domain of the compressor.

From the figures above we see that at a clearance of C = 0.05 mm, there exists a difference between the two efficiencies (experimental and model). Hence, the next step would be to increase the clearance and suitably optimize the other contributing factors to fit to the ideal linear line of the graph. The largest clearance (C = 0.15 mm) studied is chosen to check how close we can get to the equality between the experimental and modelled efficiencies. Figure 4.43 shows the results. An additional dataset for each rotational speed was also considered for better understanding.

As can be seen from the figure, the isentropic efficiency is much closer the ideal line. For 10320 rpm, datasets 7 and 25 are close to ideality whereas dataset 11 is still far. Dataset 7 has an inlet vapour quality of 0.56 and a pressure ratio of 3.19. For 12910 rpm, dataset 23, is close to the ideal line. It has an inlet vapour quality of 0.74 and pressure ratio of 2.422. Dataset 33 is close to the ideal line at 14205 rpm, with an inlet vapour quality of 0.78 and a pressure ratio of 2.62. For 15500 rpm, dataset 39 is close to ideality. It has an inlet vapour quality of 0.78 and pressure ratio of 2.96. However, certain datasets are still far from ideality. These largely include datasets at higher rotational speeds. The

average difference in isentropic efficiency is 6.3%. The volumetric efficiency from the simulations is still much higher than the experimentally derived η_{vol}. The difference between the experimental and simulated volumetric efficiency, on average, is 31%.

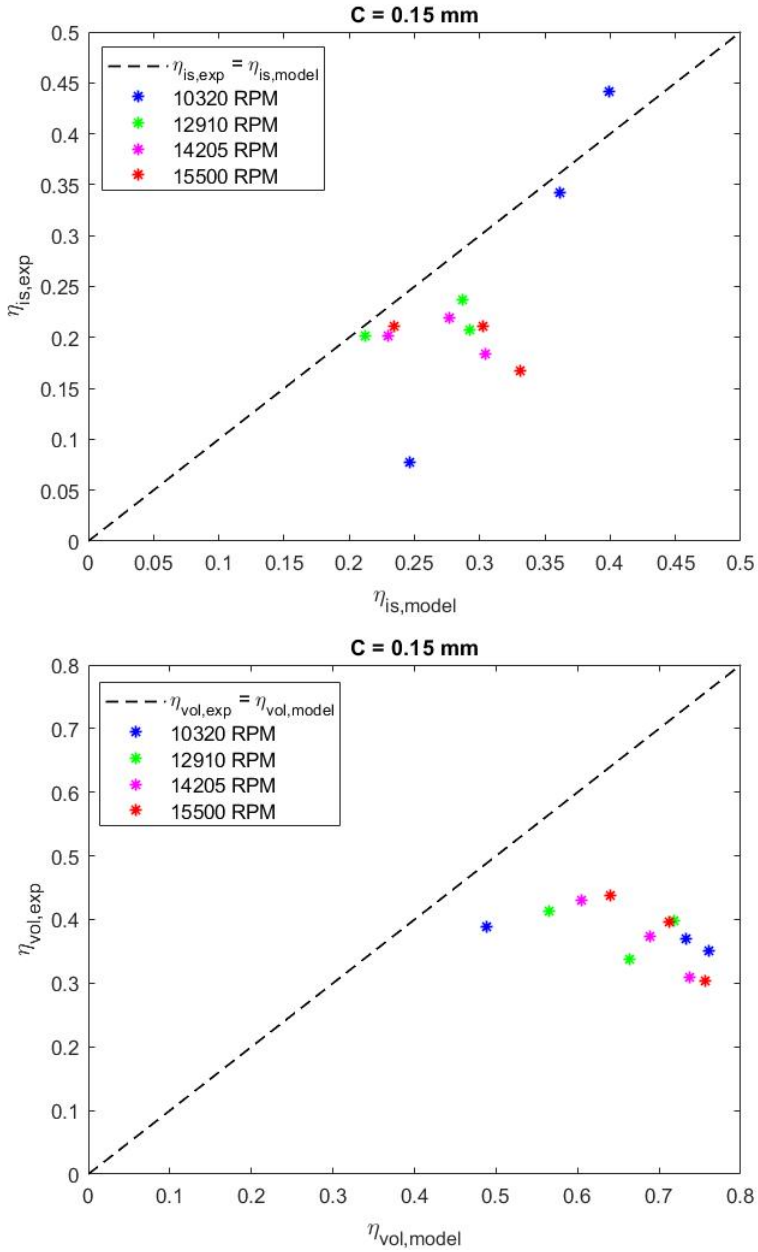

Figure 4.43: Top: Experimental Isentropic Efficiency versus the Isentropic Efficiency achieved from Simulations; Bottom: Experimental Volumetric Efficiency versus the Volumetric Efficiency achieved from Simulations, for a clearance of 0.15 mm

Only the homogeneous experimental results are validated against the model since the model developed is also homogeneous. A heterogeneous model could not be developed in the time allotted for this study. However, Zaytsev (2003) has developed a heterogeneous model in which the liquid and vapour phases are not in equilibrium. This could provide a stepping stone to a complete heterogeneous model implementation further in this project.

5

Conclusions and Recommendations

If you want a happy ending, that depends, of course, on where you stop your story

Orsen Welles

In this chapter, the most significant conclusions and recommendations are mentioned. The main objective of this study was to experimentally validate the compressor model to try to reach an isentropic efficiency of 70% of the compressor. The experimental set-up consists of a separator, absorber, the compressor itself, heat exchangers, sensors, tubing and valves. Using the separator, the amount of liquid entering the compressor can be controlled which is sprayed into the vapour line before the inlet of the compressor. While performing the experiments, it is crucial to take the system constraints into account. Two approaches are considered here: the homogeneous approach and the heterogeneous approach. In the homogeneous approach, the concentration of ammonia is constant across the compressor and the two phase process medium is treated as a single entity. In the heterogeneous approach, an assumption is made: only the vapour is compressed whereas the liquid exchanges heat with the vapour leading to partial evaporation. The isentropic, mechanical and volumetric efficiencies from both approaches are noted. Reproducibility of the experimental results is checked after a gap of two months. The model used in this study was initially developed by Guðmundsdóttir (2018) based on scaling the geometry used by Tang (1995) and Zaytsev (2003). The compressor port locations (described by the rotation angle of the male rotor) are measured using a similar twin-screw compressor and subsequently updated in the model. The leakage locations and sizes are also measured and updated wherever possible. The isentropic and volumetric efficiencies achieved from the model are noted. Validation is subsequently carried out by plotting together the efficiencies achieved from experimentation and modelling.

5.1. Conclusions

- This study focuses on the experimental validation of wet compression. In Chapter 2, an extensive background on wet compression is provided. It is mentioned that wet compression can lead to a gain in performance but is offset by the technological challenges and the irreversibilities in the system. In this study, it was determined that at higher amounts of liquid in the process medium (that is, lower vapour qualities), steady states at higher pressure ratios could be obtained (Figure 3.6). This led to higher isentropic efficiencies for experimental runs at 10320 rpm (Figure 3.12) showing the advantage of wet compression.

- There are several constraints of the experimental setup. To avoid clogging in the absorber, the return water temperature cannot exceed 100°C. It was found that the set-up is sensitive to this temperature which is in turn controlled by the amount of cooling water provided. The compressor discharge temperature is kept between 110°C and 120°C. The liquid line temperature has to be maintained between 70-75°C. The cooling water which removes heat from the oil circulating

around the compressor housing must have a temperature difference of at most 5 K for optimum performance. Keeping all these constraints in mind, obtaining a steady state for 30 minutes becomes challenging.

- For the homogeneous experimental calculation scheme, the compression power required increases with rotational speed. For higher rotational speeds, it is practically independent of the inlet vapour quality whereas for 10320 rpm, it decreases with an increase in the inlet vapour quality. The isentropic efficiency seems to reduce with an increasing amount of vapour in the system. The liquid partially seals the leakage paths, increasing the efficiency. The isentropic efficiency increases with the pressure ratio for 10320 rpm. As the rotational speed increases, the efficiency becomes independent of the vapour quality and pressure ratio. Superheating of the vapour leaving the compressor is observed. It is also possible that at the discharge only the liquid temperature is measured.
- The mechanical efficiency seems to be independent of the rotational speed. It is slightly higher for lower vapour qualities and independent of the pressure ratio. The volumetric efficiency is lower for higher liquid amounts at the compressor inlet. For the same vapour quality (0.5-0.6), it can be seen from Figure 3.15 that the volumetric efficiency decreases with higher rotational speeds.
- From the figures in Chapter 3, it can be seen that keeping certain vapour qualities and pressure ratios constant, experiments at different rotational speeds yield different efficiencies. This can be attributed to the amount of losses each run sustains. The heat removed from the process side is practically independent of the rotational speed. The heat removed by the cooling water increases with the rotational speed. Therefore the mechanical losses increase with the rotational speed.
- For the heterogeneous calculation scheme, the required compression power decreases with an increase in vapour quality. Here, this compression power is, on average, 9.755 kW lesser than what is required by the homogeneous calculation scheme. It can be seen that, this approach is much closer to the 70% threshold. In some cases, this threshold is reached and crossed. This leads to the conclusion that this approach might provide more accurate results. The isentropic efficiency increases until a vapour quality of 0.767 then falls down. Higher values of efficiencies are also achieved using the heterogeneous approach. This, in turn, leads to lower mechanical efficiencies. The mechanical efficiency reduces with a decrease in the amount of liquid at the inlet of the compressor and increases with an increase in the pressure ratio.
- Reproducibility of the experimental results is checked for 10320 rpm after two months of operation at higher rotational speeds. Also, experiments at 9030 rpm are carried out. They have a similar behaviour to the experiments at 10320 rpm. As can be seen from the figures, the new and old experimental results seem to be in agreement. It is concluded that after two months, the efficiency of the compressor did not deteriorate.
- The compressor model developed by Guðmundsdóttir (2018) had certain assumptions. Updated knowledge and measurements have been incorporated into the compressor model to provide results with greater accuracy. By establishing a base case, impact of key factors like the clearance, significant leakage paths and flow coefficients on the isentropic and volumetric efficiencies have been noted in Chapter 4. The clearance is the most significant factor causing the greatest (21%) drop in isentropic efficiency of the compressor when increased to 0.15 mm from 0.05 mm. The clearance also causes the greatest drop in volumetric efficiency of the compressor when increased to 0.15 mm (4.2%).
- Subsequently, validation of the experimental performance is carried out at the base case clearance. It is seen that the despite choosing the values of the contributing factors which cause the lowest efficiency, the model, on average, still predicts 23% higher isentropic efficiencies and 38% higher volumetric efficiencies. Increasing the clearance to 0.15 mm, the average difference in isentropic efficiency falls down to 6.3% and difference between the experimental and model volumetric efficiency falls down to 31%. After months of operation of the compressor, the clearance can increase. Also, the exact clearance after manufacturing cannot be measured. Hence, an increase in compressor clearance might be a strong explanation of the performance of the compressor. The model is more sensitive to the changes contributing to a change in the isentropic efficiency rather than the volumetric efficiency.

5.2. Recommendations For Future Work

- During experimentation, it is important to keep in mind the constraints of the system. Awareness at all times must be maintained. If the absorber is clogged, it must be unclogged before proceeding further. Clogging of the absorber can be seen by noticing instabilities in the cooling water flow. Videos and manuals have been prepared during this study, which must be followed. It is important that during start-up of the compressor, a pressure greater than the atmospheric pressure is maintained in the system. Adequate noise cancellation devices must be worn by all persons involved during operation as prolonged exposure to the compressor noise can lead to headaches.

- It was determined that the vapour at the discharge is superheated. This, in theory, should not occur with wet compression. This high temperature was masked since the discharge temperature sensors only measured the liquid temperature. These conclusions led to a heterogeneous approach. The heterogeneous approach used in this study, is a simple one based on inlet and outlet conditions. Further investigation into the discharge temperature of the liquid and vapour must be carried out. A detailed heterogeneous model and experimental approach must be carried out possibly using finite control volumes.

- Another possibility could be that the liquid which does not vapourize, only gets heated up. In order to investigate the fraction of evaporation accurately, the model must track the temperature of the liquid in the process medium through the compressor. It must also track the vapour quality of the process medium through the compressor.

- There is still a substantial difference in the accuracy of the temperature sensors at the discharge which is why only T-402 was used in this study. The new, incoming compressor contains pressure sensors. While connecting this to the experimental set-up care must be taken to ensure no ammonia enters the atmosphere while operation. The temperature sensors and their placements could also be investigated and optimized for accuracy. This new compressor will make it possible to get a p-V diagram.

- The compressor model is still primarily based on values from literature and other sources. Accurate compressor port locations and sizing are crucial for validation. Leakage path measurements, if possible, must be carried out. The size of the clearances, if possible, must be measured. This study was a first step for a robust validation. The next step would be to question why is there is discrepancy between the experimental and model results and to subsequently make improvements. In order to execute this process effectively, a policy of open, accurate and timely communication between the compressor manufacturer and the researchers must be adopted. Several aspects of this compressor were made known only during this study which proved challenging to incorporate without a holistic knowledge of the compressor specifications.

- Furthermore, a thermodynamic model with ammonia-carbon dioxide-water has been developed. An experimental study into the performance of a twin-screw compressor with wet compression and a ternary mixture would be an interesting avenue. A heterogeneous compressor model could also be developed based on the phase changes of the three components.

Appendices

A

Error Propagation

Contains formulae used to get the error bars. As per equation, uncertainty analysis is done to check the accuracy of the data. Here, the various error propagation formulae which are used in this uncertainty are listed.

A.1. Error Formulation for the Homogeneous Calculation Scheme for Experimental Data

Temperature value accounting for error:

$$T = T_{\text{sensor}} + T_{\text{err}} \tag{A.1}$$

Pressure value accounting for error:

$$p = p_{\text{sensor}} + p_{\text{err}} p_{\text{sensor}} \tag{A.2}$$

Ammonia concentration value accounting for error:

$$w = w_{\text{calc}} + w_{\text{err}} \tag{A.3}$$

To calculate values of certain properties like enthalpy, entropy, vapour quality and density, temperature, pressure and concentration of ammonia in ammonia-water are used. Here the error propagation is defined as :

$$h_{\text{err}} = \sqrt{(h_{\text{T,err}} - h)^2 + (h_{\text{p,err}} - h)^2 + (\text{h}_{\text{w,err}} - h)^2} \tag{A.4}$$

This equation can be used for any of the above mentioned properties.

Error in the mass flow (vapour and liquid):

$$\dot{m}_{\text{v/L,err}} = \dot{m}_{\text{err}} \dot{m}_{\text{v/L}} \tag{A.5}$$

Hence, the total mass flow error becomes:

$$\dot{m}_{\text{flow,err}} = \sqrt{(\dot{m}_{\text{L,err}})^2 + (\dot{m}_{\text{v,err}})^2} \tag{A.6}$$

Error in the concentration of ammonia at the inlet:

$$w_{1,\mathrm{err}} = \sqrt{\left[-\frac{1}{\dot{m}_{\mathrm{flow}}^2}(\dot{m}_{\mathrm{L}} w_{\mathrm{L}} + \dot{m}_{\mathrm{v}} w_{\mathrm{v}})\dot{m}_{\mathrm{flow,err}}\right]^2 + \left(\frac{w_{\mathrm{L}}}{\dot{m}_{\mathrm{flow}}}\dot{m}_{\mathrm{L,err}}\right)^2 + \left(\frac{\dot{m}_{\mathrm{L}}}{\dot{m}_{\mathrm{flow}}} w_{\mathrm{L,err}}\right)^2 + \left(\frac{w_{\mathrm{v}}}{\dot{m}_{\mathrm{flow}}}\dot{m}_{\mathrm{v,err}}\right)^2 + \left(\frac{m_{\mathrm{v}}}{\dot{m}_{\mathrm{flow}}} w_{\mathrm{v,err}}\right)^2} \tag{A.7}$$

Error in the enthalpy at the inlet of the compressor:

$$h_{1,\mathrm{err}} = \sqrt{\left[-\frac{1}{\dot{m}_{\mathrm{flow}}^2}(\dot{m}_{\mathrm{L}} h_{\mathrm{L}} + \dot{m}_{\mathrm{v}} h_{\mathrm{v}})\dot{m}_{\mathrm{flow,err}}\right]^2 + \left(\frac{h_{\mathrm{L}}}{\dot{m}_{\mathrm{flow}}}\dot{m}_{\mathrm{L,err}}\right)^2 + \left(\frac{\dot{m}_{\mathrm{L}}}{\dot{m}_{\mathrm{flow}}} h_{\mathrm{L,err}}\right)^2 + \left(\frac{h_{\mathrm{v}}}{\dot{m}_{\mathrm{flow}}}\dot{m}_{\mathrm{v,err}}\right)^2 + \left(\frac{m_{\mathrm{v}}}{\dot{m}_{\mathrm{flow}}} h_{\mathrm{v,err}}\right)^2} \tag{A.8}$$

Error in the vapour quality at the inlet of the compressor:

$$q_{1,\mathrm{err}} = \sqrt{\left(\frac{1}{h_{\mathrm{v}} - h_{\mathrm{L}}} h_{1,\mathrm{err}}\right)^2 + \left(\frac{-1}{h_{\mathrm{v}} - h_{\mathrm{L}}} h_{\mathrm{L,err}}\right)^2 + \left[-\frac{h_1 - h_{\mathrm{L}}}{(h_{\mathrm{v}} - h_{\mathrm{L}})^2} h_{\mathrm{v,err}}\right]^2 + \left[\frac{h_1 - h_{\mathrm{v}}}{(h_{\mathrm{v}} - h_{\mathrm{L}})^2} h_{\mathrm{L,err}}\right]^2} \tag{A.9}$$

Error in the total isentropic efficiency:

$$\eta_{\mathrm{total,err}} = \sqrt{\left[-\frac{(h_{2,\mathrm{s}} - h_1)\dot{m}_{\mathrm{flow}}}{\dot{W}_{\mathrm{elec}}^2}\dot{W}_{\mathrm{elec,err}}\right]^2 + \left(\frac{\dot{m}_{\mathrm{flow}}}{\dot{W}_{\mathrm{elec}}} h_{2,\mathrm{s,err}}\right)^2 + \left(-\frac{\dot{m}_{\mathrm{flow}}}{\dot{W}_{\mathrm{elec}}} h_{1,\mathrm{err}}\right)^2 + \left[\frac{h_{2,\mathrm{s}} - h_1}{\dot{W}_{\mathrm{elec}}}\dot{m}_{\mathrm{flow,err}}\right]^2} \tag{A.10}$$

Error in the cooling water loss:

$$\dot{W}_{\mathrm{cw,err}} = \sqrt{\left[\frac{4.18 \cdot 1000}{3600}(T_{\mathrm{cw,out}} - T_{\mathrm{cw,in}})\dot{m}_{\mathrm{cw,err}}\right]^2 + 2\left(\frac{4.18 \cdot 1000}{3600}\dot{m}_{\mathrm{cw}} T_{\mathrm{err}}\right)^2} \tag{A.11}$$

Error in the power fed to the compressor:

$$\dot{W}_{\mathrm{in,err}} = 0.95 \cdot 0.98 \cdot \dot{W}_{\mathrm{elec,err}} \tag{A.12}$$

Error in the heat removed from the rotor by the oil from the process side:

$$\dot{W}_{\mathrm{oil\ process,err}} = \sqrt{2(\mathrm{U_{rotor}A_{rotor}}T_{\mathrm{err}})^2} \tag{A.13}$$

Error in the power required by the compressor for the compression process:

$$\dot{W}_{\mathrm{comp,err}} = \sqrt{(\dot{W}_{\mathrm{elec,err}})^2 + (\dot{W}_{\mathrm{cw,err}})^2 + (\dot{W}_{\mathrm{oil\ process,err}})^2} \tag{A.14}$$

Error in the isentropic efficiency of the compressor:

$$\eta_{\mathrm{is,err}} = \sqrt{\left[\frac{(h_{2,\mathrm{is}} - h_1)}{\dot{W}_{\mathrm{comp}}}\dot{m}_{\mathrm{flow,err}}\right]^2 + \left(\frac{\dot{m}_{\mathrm{flow}}}{\dot{W}_{\mathrm{comp}}} h_{2,\mathrm{is,err}}\right)^2 + \left(-\frac{\dot{m}_{\mathrm{flow}}}{\dot{W}_{\mathrm{comp}}} h_{1,\mathrm{err}}\right)^2 + \left[-\frac{(h_{2,\mathrm{is}} - h_1)\dot{m}_{\mathrm{flow}}}{\dot{W}_{\mathrm{comp}}^2}\dot{W}_{\mathrm{comp,err}}\right]^2} \tag{A.15}$$

Error in the compressor discharge enthalpy:

$$h_2 = \sqrt{(h_{1,\mathrm{err}})^2 + \left(\frac{1}{\dot{m}_{\mathrm{flow}}}\dot{W}_{\mathrm{comp,err}}\right)^2 + \left(-\frac{\dot{W}_{\mathrm{comp}}}{\dot{m}_{\mathrm{flow}}^2}\dot{m}_{\mathrm{flow,err}}\right)^2} \tag{A.16}$$

Error in the mechanical efficiency:

$$\eta_{\mathrm{mech,err}} = \sqrt{\left(\frac{1}{\eta_{\mathrm{is}}}\eta_{\mathrm{total,err}}\right)^2 + \left(-\frac{\eta_{\mathrm{total}}}{\eta_{\mathrm{is}}^2}\eta_{\mathrm{is,err}}\right)^2} \tag{A.17}$$

Error in specific volume:

$$v_{\mathrm{err}} = -\frac{1}{\rho^2}\rho_{\mathrm{err}} \tag{A.18}$$

Error in inlet density:

$$\rho_{1,\mathrm{err}} = \sqrt{\left[\frac{-(v_{\mathrm{L}} - v_{\mathrm{v}})}{((1-q_1)v_{\mathrm{L}} + q_1 v_{\mathrm{v}})^2}q_{1,\mathrm{err}}\right]^2 + \left[\frac{-(1-q_1)}{((1-q_1)v_{\mathrm{L}} + q_1 v_{\mathrm{v}})^2}v_{\mathrm{L,err}}\right]^2 + \left[\frac{-q_1}{((1-q_1)v_{\mathrm{L}} + q_1 v_{\mathrm{v}})^2}v_{\mathrm{v,err}}\right]^2} \tag{A.19}$$

Error in the fraction of liquid evaporation:

$$r_{\mathrm{evap,err}} = \sqrt{\left(-\frac{\dot{W}_{\mathrm{oil\ process}}}{\dot{W}_{\mathrm{evap}}^2}\dot{W}_{\mathrm{evap,err}}\right)^2 + \left(\frac{\dot{W}_{\mathrm{oil\ process,err}}}{\dot{W}_{\mathrm{evap}}}\right)^2} \tag{A.20}$$

Error in the volumetric efficiency considering evaporation:

$$\begin{aligned}\eta_{\mathrm{vol,evap,err}} = \Bigg\{&\left[-\frac{(\dot{m}_{\mathrm{v}} + \mathrm{r}_{\mathrm{evap}}\dot{m}_{\mathrm{L}})}{\rho_{\mathrm{v}}^2 \cdot \mathrm{V}_{\mathrm{max}} \cdot \omega \cdot \mathrm{z}_1}\rho_{\mathrm{v,err}}\right]^2 + \left[\frac{1}{\rho_{\mathrm{v}} \cdot \mathrm{V}_{\mathrm{max}} \cdot \omega \cdot \mathrm{z}_1}\dot{m}_{\mathrm{v,err}}\right]^2 \\ &+ \left[\frac{\mathrm{r}_{\mathrm{evap}}}{\rho_{\mathrm{v}} \cdot \mathrm{V}_{\mathrm{max}} \cdot \omega \cdot \mathrm{z}_1}\dot{m}_{\mathrm{L,err}}\right]^2 + \left[\frac{\dot{m}_{\mathrm{L}}}{\rho_{\mathrm{v}} \cdot \mathrm{V}_{\mathrm{max}} \cdot \omega \cdot \mathrm{z}_1}\mathrm{r}_{\mathrm{evap,err}}\right]^2\Bigg\}^{\frac{1}{2}}\end{aligned} \tag{A.21}$$

A.2. Error Formulation for the Heterogeneous Calculation Scheme for Experimental Data

Error in the fraction of liquid evaporated:

$$x_{\mathrm{vL,err}} = \sqrt{\left(\frac{1}{w_{\mathrm{vL}} - w_{\mathrm{LL}}}w_{\mathrm{L,err}}\right)^2 + \left(\frac{-1}{w_{\mathrm{vL}} - w_{\mathrm{LL}}}w_{\mathrm{LL,err}}\right)^2 + \left[-\frac{w_{\mathrm{L}} - w_{\mathrm{LL}}}{(w_{\mathrm{vL}} - w_{\mathrm{LL}})^2}w_{\mathrm{vL,err}}\right]^2 + \left[\frac{w_1 - w_{\mathrm{vL}}}{(w_{\mathrm{vL}} - w_{\mathrm{LL}})^2}w_{\mathrm{LL,err}}\right]^2} \tag{A.22}$$

Error in the concentration of ammonia in the vapour phase at the outlet of the compressor:

$$w_{\mathrm{v,out,err}} = \sqrt{(w_{\mathrm{v,out,err,1}})^2 + (w_{\mathrm{v,out,err,2}})^2 + (w_{\mathrm{v,out,err,3}})^2 + (w_{\mathrm{v,out,err,4}})^2 + (w_{\mathrm{v,out,err,5}})^2} \tag{A.23}$$

where:

$$w_{\mathrm{v,out,err,1}} = \frac{(\dot{m}_{\mathrm{v}} + x_{\mathrm{vL}}\dot{m}_{\mathrm{L}})w_{\mathrm{v}} - (\dot{m}_{\mathrm{v}}w_{\mathrm{v}} + x_{\mathrm{vL}}\dot{m}_{\mathrm{L}}w_{\mathrm{vL}})}{(\dot{m}_{\mathrm{v}} + x_{\mathrm{vL}}\dot{m}_{\mathrm{L}})^2}\dot{m}_{\mathrm{v,err}} \tag{A.24}$$

$$w_{\mathrm{v,out,err,2}} = \frac{(\dot{m}_{\mathrm{v}} + x_{\mathrm{vL}}\dot{m}_{\mathrm{L}})(\dot{m}_{\mathrm{L}}w_{\mathrm{vL}}) - \dot{m}_{\mathrm{L}}(\dot{m}_{\mathrm{v}} + x_{\mathrm{vL}}\dot{m}_{\mathrm{L}})}{(\dot{m}_{\mathrm{v}} + x_{\mathrm{vL}}\dot{m}_{\mathrm{L}})^2}x_{\mathrm{vL,err}} \tag{A.25}$$

$$w_{\mathrm{v,out,err,3}} = \frac{(\dot{m}_{\mathrm{v}} + x_{\mathrm{vL}}\dot{m}_{\mathrm{L}})(x_{\mathrm{vL}}w_{\mathrm{vL}}) - x_{\mathrm{vL}}(\dot{m}_{\mathrm{v}}w_{\mathrm{v}} + x_{\mathrm{vL}}\dot{m}_{\mathrm{L}}w_{\mathrm{vL}})}{(\dot{m}_{\mathrm{v}} + x_{\mathrm{vL}}\dot{m}_{\mathrm{L}})^2}\dot{m}_{\mathrm{L,err}} \tag{A.26}$$

$$w_{\mathrm{v,out,err,4}} = \frac{\dot{m}_{\mathrm{v}}}{\dot{m}_{\mathrm{v}} + x_{\mathrm{vL}}\dot{m}_{\mathrm{L}}}w_{\mathrm{v,err}} \tag{A.27}$$

$$w_{\mathrm{v,out,err,5}} = \frac{\dot{m}_{\mathrm{L}}x_{\mathrm{vL}}}{\dot{m}_{\mathrm{v}} + x_{\mathrm{vL}}\dot{m}_{\mathrm{L}}}w_{\mathrm{vL,err}} \tag{A.28}$$

Error in the concentration of ammonia in the liquid phase at the outlet of the compressor:

$$w_{\mathrm{L,out,err}} = \sqrt{\left[\frac{1}{1 - x_{\mathrm{vL}}}w_{\mathrm{L,err}}\right]^2 + \left[\frac{-x_{\mathrm{vL}}}{1 - x_{\mathrm{vL}}}w_{\mathrm{vL,err}}\right]^2 + \left[\frac{-w_{\mathrm{vL}}(1 - x_{\mathrm{vL}}) + (w_{\mathrm{L}} - x_{\mathrm{vL}}w_{\mathrm{vL}})}{(1 - x_{\mathrm{vL}})^2}x_{\mathrm{vL,err}}\right]^2} \tag{A.29}$$

Error in the heterogeneous discharge enthalpy:

$$h_{\mathrm{2,het,err}} = \sqrt{(h_{\mathrm{2,het,err,1}})^2 + (h_{\mathrm{2,het,err,2}})^2 + (h_{\mathrm{2,het,err,3}})^2 + (h_{\mathrm{2,het,err,4}})^2 + (h_{\mathrm{2,het,err,5}})^2 + (h_{\mathrm{2,het,err,6}})^2} \tag{A.30}$$

where:

$$h_{\mathrm{2,het,err,1}} = \frac{(\dot{m}_{\mathrm{v}} + x_{\mathrm{vL}}\dot{m}_{\mathrm{L}})h_{\mathrm{v,out}} + (1 - x_{\mathrm{vL}})\dot{m}_{\mathrm{L}}h_{\mathrm{L,out}}}{\dot{m}_{\mathrm{flow}}^2}\dot{m}_{\mathrm{flow,err}} \tag{A.31}$$

$$h_{\mathrm{2,het,err,2}} = \frac{\dot{m}_{\mathrm{v}} + x_{\mathrm{vL}}\dot{m}_{\mathrm{L}}}{\dot{m}_{\mathrm{flow}}}h_{\mathrm{v,out,err}} \tag{A.32}$$

$$h_{\mathrm{2,het,err,3}} = \frac{(1 - x_{\mathrm{vL}})\dot{m}_{\mathrm{L}}}{\dot{m}_{\mathrm{flow}}}h_{\mathrm{L,out,err}} \tag{A.33}$$

$$h_{\mathrm{2,het,err,4}} = \frac{h_{\mathrm{v,out}}}{\dot{m}_{\mathrm{flow}}}\dot{m}_{\mathrm{v,err}} \tag{A.34}$$

$$h_{\mathrm{2,het,err,5}} = \frac{x_{\mathrm{vL}}h_{\mathrm{v,out}} + (1 - x_{\mathrm{vL}})h_{\mathrm{L,out}}}{\dot{m}_{\mathrm{flow}}}\dot{m}_{\mathrm{L,err}} \tag{A.35}$$

$$h_{\mathrm{2,het,err,6}} = \frac{\dot{m}_{\mathrm{L}}h_{\mathrm{v,out}} - \dot{m}_{\mathrm{L}}h_{\mathrm{L,out}}}{\dot{m}_{\mathrm{flow}}}x_{\mathrm{vL,err}} \tag{A.36}$$

Error in the overall ammonia concentration at the discharge of the compressor:

$$w_{\mathrm{2,err}} = \sqrt{(w_{\mathrm{2,err,1}})^2 + (w_{\mathrm{2,err,2}})^2 + (w_{\mathrm{2,err,3}})^2 + (w_{\mathrm{2,err,4}})^2 + (w_{\mathrm{2,err,5}})^2 + (w_{\mathrm{2,err,6}})^2} \tag{A.37}$$

where:

$$w_{2,\mathrm{err},1} = \frac{(\dot{m}_\mathrm{v} + x_\mathrm{vL}\dot{m}_\mathrm{L})w_\mathrm{v,out} + (1 - x_\mathrm{vL})\dot{m}_\mathrm{L}w_\mathrm{L,out}}{\dot{m}_\mathrm{flow}^2}\dot{m}_\mathrm{flow,err} \tag{A.38}$$

$$w_{2,\mathrm{err},2} = \frac{\dot{m}_\mathrm{v} + x_\mathrm{vL}\dot{m}_\mathrm{L}}{\dot{m}_\mathrm{flow}}w_\mathrm{v,out,err} \tag{A.39}$$

$$w_{2,\mathrm{err},3} = \frac{(1 - x_\mathrm{vL})\dot{m}_\mathrm{L}}{\dot{m}_\mathrm{flow}}w_\mathrm{L,out,err} \tag{A.40}$$

$$w_{2,\mathrm{err},4} = \frac{w_\mathrm{v,out}}{\dot{m}_\mathrm{flow}}\dot{m}_\mathrm{v,err} \tag{A.41}$$

$$w_{2,\mathrm{err},5} = \frac{x_\mathrm{vL}w_\mathrm{v,out} + (1 - x_\mathrm{vL})w_\mathrm{L,out}}{\dot{m}_\mathrm{flow}}\dot{m}_\mathrm{L,err} \tag{A.42}$$

$$w_{2,\mathrm{err},6} = \frac{\dot{m}_\mathrm{L}w_\mathrm{v,out} - \dot{m}_\mathrm{L}w_\mathrm{L,out}}{\dot{m}_\mathrm{flow}}x_\mathrm{vL,err} \tag{A.43}$$

Error in the power required for the compression process:

$$\dot{W}_\mathrm{comp,het,err} = \sqrt{[(h_\mathrm{2,het} - h_1)\dot{m}_\mathrm{flow,err}]^2 + (\dot{m}_\mathrm{flow}h_\mathrm{2,het,err})^2 + (-\dot{m}_\mathrm{flow}h_\mathrm{1,err})^2 + (\dot{W}_\mathrm{oil\ process,err})^2} \tag{A.44}$$

Error in the isentropic efficiency obtained from the heterogeneous calculation scheme:

$$\begin{aligned}\eta_\mathrm{is,het,err} = \Bigg\{ &\left[\frac{(h_\mathrm{2,is,het} - h_\mathrm{v})\dot{m}_\mathrm{v,err}}{\dot{W}_\mathrm{comp,het}}\right]^2 + \left[\frac{(h_\mathrm{2,is,het} - h_\mathrm{v})q_\mathrm{vL}\dot{m}_\mathrm{L,err}}{\dot{W}_\mathrm{comp,het}}\right]^2 + \left[\frac{(h_\mathrm{2,is,het} - h_\mathrm{v})\dot{m}_\mathrm{L}q_\mathrm{vL,err}}{\dot{W}_\mathrm{comp,het}}\right]^2 \\ &+ \left[\frac{\dot{m}_\mathrm{v} + q_\mathrm{vL}\dot{m}_\mathrm{L}}{\dot{W}_\mathrm{comp,het}}h_\mathrm{2,is,het,err}\right]^2 + \left[-\frac{\dot{m}_\mathrm{v} + q_\mathrm{vL}\dot{m}_\mathrm{L}}{\dot{W}_\mathrm{comp,het}}h_\mathrm{v,err}\right]^2 \\ &+ \left[\frac{-(h_\mathrm{2,is,het} - h_\mathrm{v})(\dot{m}_\mathrm{v} + q_\mathrm{vL}\dot{m}_\mathrm{L})}{\dot{W}_\mathrm{comp,het}^2}\dot{W}_\mathrm{comp,het,err}\right]^2 \Bigg\}^{\frac{1}{2}}\end{aligned} \tag{A.45}$$

Error in the total isentropic efficiency obtained from the heterogeneous calculation scheme:

$$\begin{aligned}\eta_\mathrm{total,het,err} = \Bigg\{ &\left[\frac{(h_\mathrm{2,is,het} - h_\mathrm{v})\dot{m}_\mathrm{v,err}}{\dot{W}_\mathrm{elec}}\right]^2 + \left[\frac{(h_\mathrm{2,is,het} - h_\mathrm{v})q_\mathrm{vL}\dot{m}_\mathrm{L,err}}{\dot{W}_\mathrm{elec}}\right]^2 + \left[\frac{(h_\mathrm{2,is,het} - h_\mathrm{v})\dot{m}_\mathrm{L}q_\mathrm{vL,err}}{\dot{W}_\mathrm{elec}}\right]^2 \\ &+ \left[\frac{\dot{m}_\mathrm{v} + q_\mathrm{vL}\dot{m}_\mathrm{L}}{\dot{W}_\mathrm{elec}}h_\mathrm{2,is,het,err}\right]^2 + \left[-\frac{\dot{m}_\mathrm{v} + q_\mathrm{vL}\dot{m}_\mathrm{L}}{\dot{W}_\mathrm{elec}}h_\mathrm{v,err}\right]^2 \\ &+ \left[\frac{-(h_\mathrm{2,is,het} - h_\mathrm{v})(\dot{m}_\mathrm{v} + q_\mathrm{vL}\dot{m}_\mathrm{L})}{\dot{W}_\mathrm{elec}^2}\dot{W}_\mathrm{elec,err}\right]^2 \Bigg\}^{\frac{1}{2}}\end{aligned} \tag{A.46}$$

Error in the mechanical efficiency from the heterogeneous calculation scheme:

$$\eta_\mathrm{mech,het,err} = \sqrt{\left(\frac{1}{\eta_\mathrm{is,het}}\eta_\mathrm{total,het,err}\right)^2 + \left(-\frac{\eta_\mathrm{total,het}}{\eta_\mathrm{is,het}^2}\eta_\mathrm{is,het,err}\right)^2} \tag{A.47}$$

B

Experimental Data : Homogeneous Calculation Scheme

In this appendix. the experimental data collected for different rotational speeds of the compressor are given.

B.1. Liquid and Vapour Line Measured Values

The Pressure is given in bara and temperature is °C.

Table B.1: Experimental Data: Vapour Line Sensor Values

Dataset	P − 402	T − 406	T − 802
1	1.6969	69.3539	59.6142
2	1.8705	72.7420	63.2845
3	1.9252	73.1261	63.7900
4	1.8446	74.1212	64.2787
5	1.5408	68.9147	59.1107
6	2.1398	76.9741	68.0536
7	1.7732	73.3397	63.4940
8	1.7575	73.1750	63.1406
9	1.6968	71.8369	61.6175
10	2.7040	80.2397	73.1655
11	2.4375	77.0773	70.2362
12	1.8782	70.6891	62.2777
14	1.8489	75.3709	65.5656
15	1.9024	72.8870	63.6159
16	1.8604	75.2701	66.5252
17	1.8188	74.6382	65.8919
18	1.9293	73.5500	66.2432
19	1.8516	75.3111	66.1494
20	2.0714	76.0087	67.8725
21	1.7334	73.9030	64.6934
22	1.8679	75.0971	65.9399
23	2.5832	82.2024	74.8612
24	2.1036	79.2561	71.1676
25	1.7602	72.6164	63.0335
26	2.1025	79.0151	71.5251
27	1.7893	77.6837	70.5101

28	1.7088	77.2162	69.8428
29	1.7126	77.2098	69.8081
30	1.3752	73.6395	62.6090
31	1.5390	74.6934	64.7247
32	1.4697	75.2458	65.0825
33	2.3689	81.6394	74.9343
34	2.2301	80.8091	74.0719
36	1.5178	76.0437	68.8124
37	1.3335	73.6057	65.2262
38	1.3335	73.6057	65.2262
39	1.9461	79.1586	73.0454
40	1.5511	75.5051	66.1110
42	1.7576	73.0759	63.6334
43	1.9584	75.3630	66.3028
44	1.9692	75.4928	66.5121
45	1.9685	75.4571	66.4667
46	1.6944	72.5685	62.5649
47	1.9167	75.7391	66.4884
48	1.8228	73.3725	64.4406
49	3.1012	84.8624	78.6121
50	2.0870	76.7790	68.3926
51	2.1364	77.4526	69.4156

Table B.2: Experimental Data: Liquid Line Sensor Values

Dataset	**P − 401**	**T − 407**	**T − 801**
1	1.9096	57.1224	54.6128
2	2.2120	60.7458	57.9494
3	2.2739	61.6828	58.9189
4	2.3231	62.4894	59.0810
5	1.6412	53.7506	51.7160
6	2.4927	65.6846	63.3956
7	2.2670	62.8912	59.3385
8	1.9501	58.6911	56.4632
9	2.3325	62.8535	58.3669
10	2.7597	65.4377	64.3859
11	2.4628	55.4019	50.5405
12	2.5343	65.2385	61.0007
14	2.3967	63.3725	59.5721
15	2.3414	62.0588	58.9493
16	2.4302	66.6310	62.7835
17	2.1885	63.8234	61.0374
18	2.0261	60.1347	58.5970
19	2.3259	64.7745	61.3614
20	2.3764	65.1162	62.7174
21	2.0622	61.7290	58.7597
22	2.2293	62.4337	59.6514
23	2.7607	68.9719	68.1993
24	2.4660	67.4422	65.2529
25	2.4099	64.6914	60.1908
26	2.3269	65.8783	63.8384
27	2.2196	64.4909	61.1286
28	2.2673	64.9386	60.7509
29	2.2783	65.1573	60.9637

30	2.0178	63.6135	58.2723
31	2.2111	66.8749	61.7934
32	2.0343	63.1768	58.4550
33	2.4921	67.1280	65.8319
34	2.4300	66.2506	64.7918
36	2.0909	62.5611	57.9321
37	2.0206	61.8806	56.2536
38	2.0206	61.8806	56.2536
39	2.1608	63.9528	61.6957
40	2.2456	64.5800	59.4503
42	2.2101	63.2079	59.8782
43	2.3290	65.0455	62.2118
44	2.2877	64.9238	62.2925
45	2.2775	64.6541	62.0876
46	2.0090	61.1126	58.1328
47	2.1284	63.1649	60.8876
48	1.9699	61.1006	59.0328
49	3.1144	65.2055	60.8078
50	2.2059	62.7385	61.3824
51	2.1956	60.1963	59.8933

B.2. Temperatures

Table B.3: Experimental Data: Temperature in the separator (°C)

Dataset	**Speed [RPM]**	**T – 405**
1	10320	85.9180
2	10320	89.6991
3	10320	91.2888
4	10320	89.3748
5	10320	77.7632
6	10320	91.2985
7	10320	89.2369
8	10320	83.1959
9	10320	87.4070
10	10320	91.5250
11	10320	84.5732
12	12910	90.3922
14	12910	86.2430
15	12910	90.0186
16	12910	91.8185
17	12910	91.1325
18	12910	90.5049
19	12910	88.2152
20	12910	92.6206
21	12910	84.7285
22	12910	86.8531
23	12910	93.4961
24	10320	92.5453
25	10320	88.1150
26	14205	89.1481
27	14205	88.8586
28	14205	88.3964

29	14205	88.4871
30	14205	85.6239
31	14205	92.3395
32	14205	87.0125
33	14205	93.2629
34	14205	91.9707
36	15500	87.0090
37	15500	85.3026
38	15500	85.3026
39	15500	90.6506
40	15500	92.3013
42	10320	87.9169
43	10320	91.5210
44	10320	91.2070
45	10320	91.3563
46	10320	86.8359
47	10320	87.8890
48	10320	89.4107
49	10320	94.8770
50	9030	89.2727
51	9030	88.6608

Table B.4: Experimental Data: Temperatures in °C

Dataset	Speed [RPM]	T_s	T_d	T_{lift}
1	10320	64.2803	118.6621	54.3817
2	10320	65.2235	119.3431	54.1197
3	10320	66.2375	120.8250	54.5875
4	10320	61.9981	113.7053	51.7073
5	10320	57.4265	101.9398	44.5133
6	10320	64.2885	112.3369	48.0484
7	10320	64.5505	115.5123	50.9618
8	10320	59.4802	106.0501	46.5699
9	10320	60.6252	110.4866	49.8614
10	10320	69.0462	110.8043	41.7581
11	10320	62.8929	109.5366	46.6437
12	12910	61.1105	123.9484	62.8379
14	12910	59.2224	111.2032	51.9808
15	12910	59.4140	118.7004	59.2864
16	12910	62.4972	118.7895	56.2923
17	12910	61.8760	119.0496	57.1736
18	12910	60.5345	122.9900	62.4555
19	12910	60.7855	111.4651	50.6796
20	12910	63.4988	120.6666	57.1678
21	12910	58.9573	109.5422	50.5849
22	12910	59.9099	110.8070	50.8970
23	12910	68.6628	111.1740	42.5112
24	10320	65.2791	109.0856	43.8065
25	10320	61.2152	111.3635	50.1484
26	14205	64.1682	109.8845	45.7163
27	14205	60.7981	112.9521	52.1540
28	14205	59.9718	112.2641	52.2923
29	14205	60.0912	112.4154	52.3242
30	14205	56.6796	112.0726	55.3930

31	14205	60.4765	120.2639	59.7873
32	14205	57.5437	111.7368	54.1931
33	14205	66.8960	113.0427	46.1467
34	14205	65.4993	112.1263	46.6270
36	15500	56.9389	112.4877	55.5487
37	15500	54.4182	113.5524	59.1342
38	15500	54.4182	113.5524	59.1342
39	15500	62.4863	112.7187	50.2324
40	15500	58.2693	123.8464	65.5772
42	10320	60.7419	111.3279	50.5860
43	10320	63.5108	116.8046	53.2938
44	10320	63.9487	117.3281	53.3794
45	10320	63.9135	117.3426	53.4290
46	10320	61.1592	111.7593	50.6002
47	10320	62.9213	109.9516	47.0303
48	10320	64.4344	117.6449	53.2105
49	10320	72.7415	108.8318	36.0903
50	9030	65.8042	108.8707	43.0665
51	9030	65.7024	107.2440	41.5416

B.3. Pressures

Table B.5: Experimental Data: Pressures in bara

Dataset	**Speed [RPM]**	**p_s**	**p_d**	**Pressure ratio**
1	10320	1.6704	5.3344	3.1936
2	10320	1.8407	5.8506	3.1785
3	10320	1.8951	6.0293	3.1814
4	10320	1.8133	5.5845	3.0798
5	10320	1.4993	4.0576	2.7064
6	10320	2.0913	5.6229	2.6887
7	10320	1.7266	5.5177	3.1956
8	10320	1.7093	4.7059	2.7531
9	10320	1.6527	5.2069	3.1505
10	10320	2.6496	5.7793	2.1812
11	10320	2.3830	4.6446	1.9491
12	12910	1.8324	5.8038	3.1672
14	12910	1.7990	5.2080	2.8949
15	12910	1.8575	5.5628	2.9948
16	12910	1.8124	5.5153	3.0430
17	12910	1.7725	5.3390	3.0122
18	12910	1.8835	5.5493	2.9463
19	12910	1.8000	5.0924	2.8291
20	12910	2.0233	5.7785	2.8559
21	12910	1.6816	4.7276	2.8114
22	12910	1.8159	5.0959	2.8062
23	12910	2.5105	6.0816	2.4225
24	10320	2.0531	5.3728	2.6170
25	10320	1.7178	5.2854	3.0768
26	14205	2.0334	5.4305	2.6707
27	14205	1.7360	5.2140	3.0035
28	14205	1.6599	5.1393	3.0962
29	14205	1.6629	5.1453	3.0942
30	14205	1.3367	4.4848	3.3551

31	14205	1.4981	5.1525	3.4392
32	14205	1.4253	4.6788	3.2828
33	14205	2.2928	6.0094	2.6210
34	14205	2.1613	5.8217	2.6937
36	15500	1.4668	4.9583	3.3803
37	15500	1.2928	4.6943	3.6312
38	15500	1.2928	4.6943	3.6312
39	15500	1.8729	5.5447	2.9605
40	15500	1.5120	5.6139	3.7128
42	10320	1.7356	5.1631	2.9749
43	10320	1.9299	5.6690	2.9374
44	10320	1.9392	5.6311	2.9038
45	10320	1.9393	5.6443	2.9105
46	10320	1.6706	5.0025	2.9945
47	10320	1.8837	5.0767	2.6950
48	10320	1.7977	5.3211	2.9600
49	10320	3.0441	5.9053	1.9399
50	9030	2.0559	5.2912	2.5737
51	9030	2.1046	5.1062	2.4262

B.4. Quality

The negative value of quality indicates subcooling. The quality is given in kg of ammonia-water in vapour/total kg of ammonia-water.

Table B.6: Experimental Data: Vapour Quality in the liquid line

Dataset	Speed [RPM]	Start q_L	End $q_{L.end}$
1	10320	0.000	0.014
2	10320	0.000	0.005
3	10320	0.000	0.003
4	10320	0.000	0.000
5	10320	0.000	0.014
6	10320	0.000	0.000
7	10320	0.000	0.000
8	10320	0.000	0.011
9	10320	0.000	0.000
10	10320	0.000	0.000
11	10320	0.000	0.000
12	12910	0.000	0.000
14	12910	0.000	0.000
15	12910	0.000	0.000
16	12910	0.000	0.000
17	12910	0.000	0.000
18	12910	0.000	0.009
19	12910	0.000	0.000
20	12910	0.000	0.001
21	12910	0.000	Subcooled
22	12910	0.000	0.000
23	12910	0.000	0.013
24	10320	0.000	0.000
25	10320	0.000	0.000
26	14205	0.000	0.020
27	14205	0.000	0.004
28	14205	0.000	0.000

29	14205	0.000	0.000
30	14205	0.000	0.000
31	14205	0.000	0.000
32	14205	0.000	0.000
33	14205	0.000	0.017
34	14205	0.000	0.016
36	15500	0.000	0.000
37	15500	0.000	0.000
38	15500	0.000	0.000
39	15500	0.000	0.016
40	15500	0.000	0.000
42	10320	0.000	0.000
43	10320	0.000	0.004
44	10320	0.000	0.009
45	10320	0.000	0.008
46	10320	0.000	0.007
47	10320	0.000	0.010
48	10320	0.000	0.015
49	10320	0.000	0.000
50	9030	0.000	0.008
51	9030	0.000	0.000

Table B.7: Experimental Data: Vapour Quality in the vapour line

Dataset	**Speed [RPM]**	**q_v**
1	10320	1.001E+00
2	10320	1.001E+00
3	10320	1.001E+00
4	10320	1.001E+00
5	10320	1.000E+00
6	10320	1.001E+00
7	10320	1.001E+00
8	10320	1.000E+00
9	10320	1.000E+00
10	10320	1.001E+00
11	10320	1.000E+00
12	12910	1.001E+00
14	12910	1.000E+00
15	12910	1.001E+00
16	12910	1.001E+00
17	12910	1.001E+00
18	12910	1.001E+00
19	12910	1.000E+00
20	12910	1.001E+00
21	12910	1.000E+00
22	12910	1.000E+00
23	12910	1.001E+00
24	10320	1.001E+00
25	10320	1.001E+00
26	14205	1.001E+00
27	14205	1.000E+00
28	14205	1.000E+00
29	14205	1.000E+00
30	14205	1.000E+00

31	14205	1.000E+00
32	14205	1.000E+00
33	14205	1.001E+00
34	14205	1.001E+00
36	15500	1.000E+00
37	15500	1.000E+00
38	15500	1.000E+00
39	15500	1.001E+00
40	15500	1.001E+00
42	10320	1.000E+00
43	10320	1.001E+00
44	10320	1.001E+00
45	10320	1.001E+00
46	10320	1.000E+00
47	10320	1.000E+00
48	10320	1.001E+00
49	10320	1.001E+00
50	9030	1.000E+00
51	9030	1.000E+00

Table B.8: Experimental Data: Vapour Quality at the Inlet of Compressor

Dataset	**Speed [RPM]**	**q_1**
1	10320	0.6677
2	10320	0.6074
3	10320	0.6046
4	10320	0.5824
5	10320	0.7674
6	10320	0.6291
7	10320	0.5623
8	10320	0.7047
9	10320	0.5653
10	10320	0.8231
11	10320	0.8887
12	12910	0.5046
13	12910	0.5671
14	12910	0.6121
15	12910	0.5923
16	12910	0.5578
17	12910	0.5878
18	12910	0.7188
19	12910	0.6467
20	12910	0.6481
21	12910	0.6766
22	12910	0.6616
23	12910	0.7393
24	10320	0.6208
25	10320	0.5651
26	14205	0.7718
27	14205	0.6818
28	14205	0.6517
29	14205	0.6512
30	14205	0.6033
31	14205	0.5608

32	14205	0.6146
33	14205	0.7884
34	14205	0.7557
36	15500	0.6544
37	15500	0.6207
38	15500	0.6207
39	15500	0.7767
40	15500	0.5751
42	10320	0.6176
43	10320	0.6215
44	10320	0.6429
45	10320	0.6420
46	10320	0.6565
47	10320	0.7039
48	10320	0.7191
49	10320	0.8798
50	9030	0.7073
51	9030	0.7740

B.5. Mass Flows

Table B.9: Experimental Data: Mass Flows in kg/s

Dataset	Speed [RPM]	m_L	m_v	m_{flow}	m_{cw} [l/h]
1	10320	0.0069	0.0138	0.0207	876.3500
2	10320	0.0095	0.0147	0.0243	875.5286
3	10320	0.0097	0.0148	0.0245	875.5286
4	10320	0.0114	0.0160	0.0274	694.7000
5	10320	0.0049	0.0161	0.0210	821.7125
6	10320	0.0105	0.0179	0.0284	829.9000
7	10320	0.0115	0.0147	0.0262	829.0778
8	10320	0.0073	0.0174	0.0247	830.3667
9	10320	0.0118	0.0154	0.0272	827.8450
10	10320	0.0048	0.0225	0.0274	688.8833
11	10320	0.0028	0.0224	0.0252	689.0750
12	12910	0.0130	0.0132	0.0262	892.0625
14	12910	0.0117	0.0185	0.0303	1012.5000
15	12910	0.0107	0.0155	0.0261	1011.4000
16	12910	0.0125	0.0158	0.0283	894.7818
17	12910	0.0108	0.0153	0.0261	894.5100
18	12910	0.0061	0.0157	0.0218	917.2286
19	12910	0.0103	0.0188	0.0291	927.0000
20	12910	0.0093	0.0171	0.0263	926.6625
21	12910	0.0086	0.0181	0.0267	926.9000
22	12910	0.0099	0.0193	0.0292	926.0333
23	12910	0.0110	0.0312	0.0422	892.9833
24	10320	0.0120	0.0196	0.0316	713.1545
25	10320	0.0119	0.0154	0.0273	660.7800
26	14205	0.0087	0.0295	0.0382	943.0813
27	14205	0.0103	0.0220	0.0323	1015.0000
28	14205	0.0115	0.0214	0.0329	1016.6667
29	14205	0.0114	0.0213	0.0328	1017.0000
30	14205	0.0108	0.0165	0.0273	1000.5000
31	14205	0.0121	0.0154	0.0275	1000.5000

32	14205	0.0113	0.0180	0.0292	1000.5000
33	14205	0.0088	0.0327	0.0415	1004.0000
34	14205	0.0100	0.0310	0.0410	1026.6667
36	15500	0.0113	0.0215	0.0328	1153.0000
37	15500	0.0111	0.0181	0.0291	1132.4000
38	15500	0.0111	0.0181	0.0291	1188.7500
39	15500	0.0086	0.0300	0.0386	1325.0000
40	15500	0.0124	0.0168	0.0291	1361.8333
42	10320	0.0099	0.0160	0.0259	705.5273
43	10320	0.0097	0.0159	0.0255	706.1800
44	10320	0.0088	0.0158	0.0245	779.1500
45	10320	0.0088	0.0158	0.0245	779.1500
46	10320	0.0081	0.0155	0.0237	786.4818
47	10320	0.0075	0.0178	0.0253	787.3500
48	10320	0.0060	0.0152	0.0212	814.9333
49	10320	0.0039	0.0284	0.0323	815.4400
50	9030	0.0073	0.0177	0.0250	725.3444
51	9030	0.0054	0.0186	0.0241	725.4500

B.6. Densities

Table B.10: Experimental Data: Densities in kg/m^3

Dataset	Speed [RPM]	ρ_L	ρ_v	ρ_1
1	10320	887.4343	1.0549	1.5789
2	10320	885.6809	1.1526	1.8959
3	10320	885.4591	1.1826	1.9545
4	10320	887.3100	1.1338	1.9452
5	10320	891.1579	0.9550	1.2440
6	10320	885.6624	1.2920	2.0519
7	10320	888.6478	1.0822	1.9227
8	10320	888.6442	1.0766	1.5269
9	10320	889.8621	1.0390	1.8365
10	10320	879.2704	1.6176	1.9645
11	10320	882.8533	1.4672	1.6505
12	12910	886.6916	1.1452	2.2667
14	12910	886.9689	1.1288	1.8428
15	12910	887.5110	1.1579	1.9531
16	12910	890.0035	1.1260	2.0166
17	12910	890.9721	1.1021	1.8732
18	12910	887.7375	1.1717	1.6292
19	12910	889.5491	1.1225	1.7346
20	12910	886.6869	1.2507	1.9281
21	12910	890.2702	1.0564	1.5604
22	12910	888.0694	1.1356	1.7153
23	12910	880.6402	1.5352	2.0753
24	10320	888.7969	1.2624	2.0317
25	10320	889.1924	1.0768	1.9039
26	14205	885.5183	1.2618	1.6341
27	14205	890.1216	1.0848	1.5900
28	14205	891.1368	1.0400	1.5949
29	14205	891.1437	1.0416	1.5985
30	14205	897.5563	0.8462	1.4018
31	14205	896.8591	0.9358	1.6674

32	14205	896.1655	0.8984	1.4608
33	14205	883.0238	1.4088	1.7863
34	14205	884.3249	1.3337	1.7639
36	15500	893.6102	0.9264	1.4149
37	15500	896.3498	0.8229	1.3249
38	15500	896.3498	0.8229	1.3249
39	15500	888.0239	1.1650	1.4993
40	15500	893.6527	0.9491	1.6489
42	10320	889.5871	1.0862	1.7575
43	10320	887.3991	1.1977	1.9254
44	10320	887.2343	1.2035	1.8706
45	10320	887.2896	1.2033	1.8729
46	10320	890.4673	1.0484	1.5959
47	10320	888.3566	1.1724	1.6646
48	10320	889.1857	1.1211	1.5583
49	10320	877.9986	1.8324	2.0822
50	9030	886.2694	1.2725	1.7980
51	9030	886.3780	1.2998	1.6787

B.7. Ammonia Concentrations

Table B.11: Experimental Data: Ammonia Concentrations in kg of ammonia/kg of ammonia-water

Dataset	Speed [RPM]	w_L	w_v	w_1
1	10320	0.260	0.920	0.701
2	10320	0.259	0.915	0.657
3	10320	0.257	0.912	0.653
4	10320	0.252	0.911	0.636
5	10320	0.253	0.925	0.768
6	10320	0.245	0.903	0.659
7	10320	0.251	0.910	0.622
8	10320	0.252	0.918	0.721
9	10320	0.249	0.912	0.624
10	10320	0.248	0.906	0.790
11	10320	0.243	0.911	0.836
12	12910	0.254	0.911	0.586
14	12910	0.255	0.917	0.660
15	12910	0.249	0.908	0.639
16	12910	0.239	0.899	0.607
17	12910	0.237	0.898	0.625
18	12910	0.246	0.905	0.720
19	12910	0.242	0.905	0.671
20	12910	0.243	0.901	0.669
21	12910	0.246	0.912	0.697
22	12910	0.248	0.911	0.687
23	12910	0.248	0.903	0.732
24	10320	0.231	0.891	0.641
25	10320	0.249	0.910	0.622
26	14205	0.249	0.909	0.758
27	14205	0.243	0.905	0.695
28	14205	0.243	0.906	0.675
29	14205	0.242	0.905	0.674
30	14205	0.233	0.902	0.636

31	14205	0.225	0.886	0.596
32	14205	0.234	0.900	0.643
33	14205	0.247	0.903	0.764
34	14205	0.248	0.905	0.744
36	15500	0.243	0.908	0.678
37	15500	0.242	0.909	0.656
38	15500	0.242	0.909	0.656
39	15500	0.245	0.905	0.757
40	15500	0.240	0.899	0.619
42	10320	0.246	0.908	0.655
43	10320	0.245	0.903	0.654
44	10320	0.245	0.904	0.669
45	10320	0.245	0.904	0.668
46	10320	0.245	0.909	0.681
47	10320	0.243	0.906	0.710
48	10320	0.244	0.905	0.719
49	10320	0.237	0.893	0.814
50	9030	0.244	0.905	0.712
51	9030	0.240	0.904	0.754

B.8. Enthalpies

Table B.12: Experimental Data: Enthalpies in J/kg

Dataset	Speed [RPM]	h_L	h_v	h_1	$h_{2.\,is}$	h_2
1	10320	1.6199E+05	1.8277E+06	1.2743E+06	1.5821E+06	1.9796E+06
2	10320	1.6045E+05	1.8393E+06	1.1802E+06	1.4380E+06	1.8286E+06
3	10320	1.6158E+05	1.8428E+06	1.1780E+06	1.4342E+06	1.8205E+06
4	10320	1.5749E+05	1.8449E+06	1.1402E+06	1.3162E+06	1.7060E+06
5	10320	1.4952E+05	1.8239E+06	1.4346E+06	1.6374E+06	1.9779E+06
6	10320	1.7767E+05	1.8582E+06	1.2349E+06	1.3491E+06	1.7422E+06
7	10320	1.5881E+05	1.8442E+06	1.1065E+06	1.3569E+06	1.6738E+06
8	10320	1.6505E+05	1.8372E+06	1.3434E+06	1.5042E+06	1.8593E+06
9	10320	1.5470E+05	1.8395E+06	1.1070E+06	1.2968E+06	1.6022E+06
10	10320	1.8161E+05	1.8650E+06	1.5672E+06	1.6588E+06	2.0474E+06
11	10320	1.2103E+05	1.8558E+06	1.6628E+06	1.6955E+06	2.0836E+06
12	12910	1.6579E+05	1.8402E+06	1.0107E+06	1.1629E+06	1.7865E+06
14	12910	1.5936E+05	1.8434E+06	1.1901E+06	1.3228E+06	1.7501E+06
15	12910	1.5738E+05	1.8458E+06	1.1575E+06	1.2630E+06	1.8674E+06
16	12910	1.7575E+05	1.8602E+06	1.1154E+06	1.2473E+06	1.8068E+06
17	12910	1.6835E+05	1.8599E+06	1.1627E+06	1.2920E+06	1.9272E+06
18	12910	1.7253E+05	1.8536E+06	1.3809E+06	1.4917E+06	2.2610E+06
19	12910	1.6900E+05	1.8539E+06	1.2586E+06	1.3790E+06	1.8775E+06
20	12910	1.7582E+05	1.8603E+06	1.2676E+06	1.3816E+06	1.9461E+06
21	12910	1.6174E+05	1.8457E+06	1.3012E+06	1.4377E+06	1.9477E+06
22	12910	1.6053E+05	1.8483E+06	1.2772E+06	1.4007E+06	1.9509E+06
23	12910	2.2107E+05	1.8715E+06	1.4412E+06	1.5387E+06	1.9239E+06
24	10320	1.8789E+05	1.8752E+06	1.2354E+06	1.3253E+06	1.6694E+06
25	10320	1.6289E+05	1.8434E+06	1.1125E+06	1.2869E+06	1.6220E+06
26	14205	2.1427E+05	1.8617E+06	1.4858E+06	1.6194E+06	2.0572E+06
27	14205	1.7398E+05	1.8639E+06	1.3262E+06	1.4639E+06	2.0159E+06
28	14205	1.6619E+05	1.8625E+06	1.2717E+06	1.4164E+06	1.9337E+06
29	14205	1.6717E+05	1.8627E+06	1.2713E+06	1.4165E+06	1.9316E+06

30	14205	1.5673E+05	1.8516E+06	1.1792E+06	1.3453E+06	1.9197E+06
31	14205	1.7357E+05	1.8679E+06	1.1237E+06	1.2712E+06	1.9286E+06
32	14205	1.5744E+05	1.8576E+06	1.2024E+06	1.3528E+06	1.8902E+06
33	14205	2.1822E+05	1.8730E+06	1.5228E+06	1.6362E+06	2.0841E+06
34	14205	2.1156E+05	1.8702E+06	1.4650E+06	1.5845E+06	2.0265E+06
36	15500	1.5364E+05	1.8596E+06	1.2700E+06	1.4246E+06	2.0013E+06
37	15500	1.4640E+05	1.8516E+06	1.2049E+06	1.3732E+06	2.1237E+06
38	15500	1.4640E+05	1.8516E+06	1.2049E+06	1.3732E+06	2.0123E+06
39	15500	1.9827E+05	1.8693E+06	1.4962E+06	1.6323E+06	2.1417E+06
40	15500	1.6085E+05	1.8609E+06	1.1386E+06	1.2898E+06	2.0454E+06
42	10320	1.6190E+05	1.8463E+06	1.2022E+06	1.3561E+06	1.7287E+06
43	10320	1.7900E+05	1.8552E+06	1.2208E+06	1.3640E+06	1.8084E+06
44	10320	1.8761E+05	1.8551E+06	1.2596E+06	1.4082E+06	1.8725E+06
45	10320	1.8510E+05	1.8553E+06	1.2574E+06	1.4052E+06	1.8700E+06
46	10320	1.6622E+05	1.8434E+06	1.2673E+06	1.4516E+06	1.8163E+06
47	10320	1.8514E+05	1.8534E+06	1.3595E+06	1.4999E+06	1.8798E+06
48	10320	1.8471E+05	1.8503E+06	1.3824E+06	1.5898E+06	2.0527E+06
49	10320	1.6738E+05	1.8861E+06	1.6795E+06	1.7171E+06	2.0645E+06
50	9030	1.8351E+05	1.8578E+06	1.3678E+06	1.5192E+06	1.8153E+06
51	9030	1.6272E+05	1.8612E+06	1.4772E+06	1.6101E+06	1.9186E+06

B.9. Subcooler Properties

The enthalpies are given in J/kg. The heat exchange that takes place in the subcooler is given in W. The temperature at the outlet of the subcooler is given in °C.

Table B.13: Subcooler Properties

Dataset	Speed [RPM]	$h_{in.sub}$	$\dot{Q}_{cw.sub}$	$h_{out.sub}$	$T_{out.sub}$
1	10320	2.7751E+05	3.9312E+02	2.2028E+05	73.2780
2	10320	2.9491E+05	6.9587E+02	2.2188E+05	73.5914
3	10320	3.0234E+05	6.9587E+02	2.3044E+05	75.4438
4	10320	2.9394E+05	7.6195E+02	2.2735E+05	74.6621
5	10320	2.4113E+05	7.4367E-01	2.4098E+05	77.7294
6	10320	3.0342E+05	5.8305E+02	2.4812E+05	79.0858
7	10320	2.9343E+05	7.8196E+02	2.2529E+05	74.1712
8	10320	2.6584E+05	3.5260E+02	2.1741E+05	72.4575
9	10320	2.8522E+05	5.4517E+02	2.3912E+05	77.2156
10	10320	3.0411E+05	2.6966E+02	2.4846E+05	79.2505
11	10320	2.7296E+05	1.0082E+02	2.3705E+05	76.6081
12	12910	2.9843E+05	8.2623E+02	2.3475E+05	76.3488
14	12910	2.7943E+05	5.5204E+02	2.3241E+05	75.8534
15	12910	2.9720E+05	5.3912E+02	2.4659E+05	78.8479
16	12910	3.0637E+05	7.6661E+02	2.4504E+05	78.2488
17	12910	3.0351E+05	7.9013E+02	2.3004E+05	74.8376
18	12910	2.9967E+05	4.6676E+02	2.2368E+05	73.6852
19	12910	2.8965E+05	3.4326E+02	2.5630E+05	80.8396
20	12910	3.0959E+05	5.1303E+02	2.5423E+05	80.4050
21	12910	2.7343E+05	3.3613E+02	2.3456E+05	76.1132
22	12910	2.8280E+05	4.9836E+02	2.3232E+05	75.6785
23	12910	3.1314E+05	7.2005E+02	2.4768E+05	79.0676
24	10320	3.1056E+05	8.0318E+02	2.4357E+05	77.6887
25	10320	2.8852E+05	5.3849E+02	2.4316E+05	78.0922
26	14205	2.9324E+05	4.0248E+02	2.4704E+05	78.9474

27	14205	2.9247E+05	4.7726E+02	2.4598E+05	78.5735
28	14205	2.9040E+05	5.1181E+02	2.4573E+05	78.5106
29	14205	2.9083E+05	4.7811E+02	2.4900E+05	79.2314
30	14205	2.7898E+05	4.1997E+02	2.4025E+05	77.0126
31	14205	3.1040E+05	6.5482E+02	2.5609E+05	80.2867
32	14205	2.8519E+05	5.7689E+02	2.3399E+05	75.6307
33	14205	3.1217E+05	5.7545E+02	2.4658E+05	78.8008
34	14205	3.0622E+05	6.5681E+02	2.4059E+05	77.4850
36	15500	2.8405E+05	5.9052E+02	2.3199E+05	75.4655
37	15500	2.7645E+05	4.4788E+02	2.3591E+05	76.3102
38	15500	2.7645E+05	4.4788E+02	2.3591E+05	76.3102
39	15500	3.0041E+05	4.8203E+02	2.4451E+05	78.3015
40	15500	3.0849E+05	8.6130E+02	2.3891E+05	76.9059
42	10320	2.8791E+05	4.1383E+02	2.4613E+05	78.6770
43	10320	3.0440E+05	5.3304E+02	2.4918E+05	79.3296
44	10320	3.0294E+05	4.5561E+02	2.5090E+05	79.7197
45	10320	3.0365E+05	4.5561E+02	2.5179E+05	79.9096
46	10320	2.8303E+05	3.4628E+02	2.4044E+05	77.4084
47	10320	2.8806E+05	3.1740E+02	2.4564E+05	78.4992
48	10320	2.9489E+05	2.8175E+02	2.4755E+05	78.9455
49	10320	3.2056E+05	2.6195E+02	2.5302E+05	79.9538
50	9030	2.9429E+05	4.8572E+02	2.2779E+05	74.5407
51	9030	2.9185E+05	4.1819E+02	2.1504E+05	71.6030

B.10. Compressor Power Consumptions

Table B.14: Experimental Data: Power consumption of the compressor in W

Dataset	Speed [RPM]	$\dot{W}_{\text{in}}$	$\dot{W}_{\text{comp}}$
1	10320	1.8238E+04	1.4583E+04
2	10320	1.9430E+04	1.5737E+04
3	10320	1.9430E+04	1.5726E+04
4	10320	1.9041E+04	1.5503E+04
5	10320	1.4890E+04	1.1403E+04
6	10320	1.8090E+04	1.4421E+04
7	10320	1.8516E+04	1.4874E+04
8	10320	1.6328E+04	1.2723E+04
9	10320	1.7037E+04	1.3468E+04
10	10320	1.6906E+04	1.3151E+04
11	10320	1.4029E+04	1.0620E+04
12	12910	2.5017E+04	2.0319E+04
14	12910	2.1731E+04	1.6948E+04
15	12910	2.3281E+04	1.8550E+04
16	12910	2.4285E+04	1.9543E+04
17	12910	2.4674E+04	1.9948E+04
18	12910	2.3973E+04	1.9225E+04
19	12910	2.2678E+04	1.8027E+04
20	12910	2.2667E+04	1.7872E+04
21	12910	2.1902E+04	1.7292E+04
22	12910	2.4227E+04	1.9655E+04
23	12910	2.5267E+04	2.0364E+04
24	10320	1.7288E+04	1.3721E+04
25	10320	1.7316E+04	1.3908E+04
26	14205	2.7250E+04	2.1816E+04

27	14205	2.7687E+04	2.2254E+04
28	14205	2.7247E+04	2.1778E+04
29	14205	2.7102E+04	2.1637E+04
30	14205	2.5495E+04	2.0240E+04
31	14205	2.7413E+04	2.2096E+04
32	14205	2.5414E+04	2.0110E+04
33	14205	2.8884E+04	2.3270E+04
34	14205	2.8710E+04	2.3005E+04
36	15500	3.0098E+04	2.3997E+04
37	15500	3.2411E+04	2.6769E+04
38	15500	2.9495E+04	2.3525E+04
39	15500	3.1256E+04	2.4933E+04
40	15500	3.2573E+04	2.6421E+04
42	10320	1.7141E+04	1.3637E+04
43	10320	1.8581E+04	1.4985E+04
44	10320	1.8737E+04	1.5025E+04
45	10320	1.8737E+04	1.5033E+04
46	10320	1.6635E+04	1.2996E+04
47	10320	1.6843E+04	1.3147E+04
48	10320	1.7917E+04	1.4203E+04
49	10320	1.6383E+04	1.2420E+04
50	9030	1.4388E+04	1.1170E+04
51	9030	1.3877E+04	1.0631E+04

B.11. Losses

Table B.15: Experimental Data: Losses of the compressor in W

Dataset	Speed [RPM]	$\dot{Q}_{\text{cw}}$	$\dot{Q}_{\text{evap}}$	$\dot{Q}_{\text{oil process}}$
1	10320	4.5253E+03	3.4439E+04	8.7011E+02
2	10320	4.5585E+03	4.0750E+04	8.6591E+02
3	10320	4.5774E+03	4.1148E+04	8.7340E+02
4	10320	4.3651E+03	4.6232E+04	8.2732E+02
5	10320	4.1991E+03	3.5138E+04	7.1221E+02
6	10320	4.4384E+03	4.7773E+04	7.6877E+02
7	10320	4.4578E+03	4.4188E+04	8.1539E+02
8	10320	4.3508E+03	4.1235E+04	7.4512E+02
9	10320	4.3669E+03	4.5830E+04	7.9778E+02
10	10320	4.4231E+03	4.6104E+04	6.6813E+02
11	10320	4.1554E+03	4.3774E+04	7.4630E+02
12	12910	5.7030E+03	4.3858E+04	1.0054E+03
14	12910	5.6151E+03	5.0963E+04	8.3169E+02
15	12910	5.6790E+03	4.4117E+04	9.4858E+02
16	12910	5.6425E+03	4.7616E+04	9.0068E+02
17	12910	5.6408E+03	4.4135E+04	9.1478E+02
18	12910	5.7477E+03	3.6718E+04	9.9929E+02
19	12910	5.4614E+03	4.9079E+04	8.1087E+02
20	12910	5.7101E+03	4.4370E+04	9.1468E+02
21	12910	5.4188E+03	4.5042E+04	8.0936E+02
22	12910	5.3870E+03	4.9235E+04	8.1435E+02
23	12910	5.5833E+03	6.9629E+04	6.8018E+02
24	10320	4.2674E+03	5.3344E+04	7.0090E+02
25	10320	4.2103E+03	4.5872E+04	8.0237E+02
26	14205	6.1650E+03	6.2905E+04	7.3146E+02

27	14205	6.2675E+03	5.4527E+04	8.3446E+02
28	14205	6.3053E+03	5.5799E+04	8.3668E+02
29	14205	6.3022E+03	5.5558E+04	8.3719E+02
30	14205	6.1415E+03	4.6327E+04	8.8629E+02
31	14205	6.2743E+03	4.6509E+04	9.5660E+02
32	14205	6.1709E+03	4.9713E+04	8.6709E+02
33	14205	6.3524E+03	6.8608E+04	7.3835E+02
34	14205	6.4515E+03	6.7951E+04	7.4603E+02
36	15500	6.9896E+03	5.5980E+04	8.8878E+02
37	15500	6.5885E+03	4.9684E+04	9.4615E+02
38	15500	6.9164E+03	4.9684E+04	9.4615E+02
39	15500	7.1273E+03	6.4540E+04	8.0372E+02
40	15500	7.2013E+03	4.9534E+04	1.0492E+03
42	10320	4.3142E+03	4.3624E+04	8.0938E+02
43	10320	4.4492E+03	4.2750E+04	8.5270E+02
44	10320	4.5664E+03	4.0881E+04	8.5407E+02
45	10320	4.5584E+03	4.0990E+04	8.5486E+02
46	10320	4.4483E+03	3.9705E+04	8.0960E+02
47	10320	4.4485E+03	4.2157E+04	7.5248E+02
48	10320	4.5648E+03	3.5291E+04	8.5137E+02
49	10320	4.5411E+03	5.5444E+04	5.7744E+02
50	9030	3.9072E+03	4.1782E+04	6.8906E+02
51	9030	3.9100E+03	4.0909E+04	6.6467E+02

B.12. Isentropic Efficiency

Table B.16: Experimental Data: Isentropic Efficiencies

Dataset	Speed [RPM]	η_{is}	η_{total}
1	10320	0.4365	0.3249
2	10320	0.3977	0.2999
3	10320	0.3987	0.3004
4	10320	0.3111	0.2358
5	10320	0.3732	0.2661
6	10320	0.2250	0.1670
7	10320	0.4414	0.3301
8	10320	0.3117	0.2261
9	10320	0.3834	0.2821
10	10320	0.1908	0.1382
11	10320	0.0779	0.0549
12	12910	0.1961	0.1483
14	12910	0.2370	0.1721
15	12910	0.1486	0.1102
16	12910	0.1908	0.1430
17	12910	0.1691	0.1273
18	12910	0.1260	0.0941
19	12910	0.1947	0.1441
20	12910	0.1680	0.1233
21	12910	0.2112	0.1552
22	12910	0.1834	0.1385
23	12910	0.2019	0.1515
24	10320	0.2071	0.1530
25	10320	0.3423	0.2560

26	14205	0.2339	0.1743
27	14205	0.1996	0.1493
28	14205	0.2186	0.1627
29	14205	0.2199	0.1634
30	14205	0.2244	0.1659
31	14205	0.1833	0.1375
32	14205	0.2187	0.1611
33	14205	0.2020	0.1515
34	14205	0.2128	0.1588
36	15500	0.2115	0.1570
37	15500	0.1832	0.1408
38	15500	0.2084	0.1548
39	15500	0.2108	0.1566
40	15500	0.1668	0.1260
42	10320	0.2923	0.2165
43	10320	0.2437	0.1829
44	10320	0.2424	0.1810
45	10320	0.2414	0.1803
46	10320	0.3357	0.2442
47	10320	0.2700	0.1962
48	10320	0.3095	0.2284
49	10320	0.0979	0.0691
50	9030	0.3384	0.2446
51	9030	0.3010	0.2147

B.13. Mechanical Efficiency

Table B.17: Experimental Data: Mechanical Efficiency

Dataset	**Speed [RPM]**	$\eta_{\mathbf{mech}}$
1	10320	0.7444
2	10320	0.7541
3	10320	0.7535
4	10320	0.7580
5	10320	0.7130
6	10320	0.7421
7	10320	0.7479
8	10320	0.7254
9	10320	0.7360
10	10320	0.7242
11	10320	0.7048
12	12910	0.7562
14	12910	0.7261
15	12910	0.7418
16	12910	0.7492
17	12910	0.7527
18	12910	0.7466
19	12910	0.7401
20	12910	0.7340
21	12910	0.7351
22	12910	0.7553
23	12910	0.7503
24	10320	0.7389
25	10320	0.7478

26	14205	0.7454
27	14205	0.7483
28	14205	0.7441
29	14205	0.7433
30	14205	0.7391
31	14205	0.7504
32	14205	0.7367
33	14205	0.7500
34	14205	0.7460
36	15500	0.7423
37	15500	0.7689
38	15500	0.7426
39	15500	0.7426
40	15500	0.7552
42	10320	0.7406
43	10320	0.7508
44	10320	0.7465
45	10320	0.7470
46	10320	0.7274
47	10320	0.7267
48	10320	0.7380
49	10320	0.7058
50	9030	0.7228
51	9030	0.7133

B.14. Volumetric Efficiency

Table B.18: Experimental Data: Rotational Speed in rev/s and Evaporation Fraction

Dataset	**Speed [RPM]**	ω	$\mathbf{r_{evap}}$
1	10320	172.00	0.0253
2	10320	172.00	0.0212
3	10320	172.00	0.0212
4	10320	172.00	0.0179
5	10320	172.00	0.0203
6	10320	172.00	0.0161
7	10320	172.00	0.0185
8	10320	172.00	0.0181
9	10320	172.00	0.0174
10	10320	172.00	0.0145
11	10320	172.00	0.0170
12	12910	215.17	0.0229
14	12910	215.17	0.0163
15	12910	215.17	0.0215
16	12910	215.17	0.0189
17	12910	215.17	0.0207
18	12910	215.17	0.0272
19	12910	215.17	0.0165
20	12910	215.17	0.0206
21	12910	215.17	0.0180
22	12910	215.17	0.0165
23	12910	215.17	0.0098
24	10320	172.00	0.0131
25	10320	172.00	0.0175

26	14205	236.75	0.0116
27	14205	236.75	0.0153
28	14205	236.75	0.0150
29	14205	236.75	0.0151
30	14205	236.75	0.0191
31	14205	236.75	0.0206
32	14205	236.75	0.0174
33	14205	236.75	0.0108
34	14205	236.75	0.0110
36	15500	258.33	0.0159
37	15500	258.33	0.0190
38	15500	258.33	0.0190
39	15500	258.33	0.0125
40	15500	258.33	0.0212
42	10320	172.00	0.0186
43	10320	172.00	0.0199
44	10320	172.00	0.0209
45	10320	172.00	0.0209
46	10320	172.00	0.0204
47	10320	172.00	0.0178
48	10320	172.00	0.0241
49	10320	172.00	0.0104
50	9030	150.50	0.0165
51	9030	150.50	0.0162

Table B.19: Experimental Data: Volumetric Efficiencies

Dataset	**Speed [RPM]**	$\eta_{\mathbf{vol.evap}}$
1	10320	0.3367
2	10320	0.3295
3	10320	0.3224
4	10320	0.3622
5	10320	0.4311
6	10320	0.3551
7	10320	0.3512
8	10320	0.4133
9	10320	0.3811
10	10320	0.3552
11	10320	0.3892
12	12910	0.2397
14	12910	0.3368
15	12910	0.2755
16	12910	0.2887
17	12910	0.2868
18	12910	0.2751
19	12910	0.3439
20	12910	0.2804
21	12910	0.3510
22	12910	0.3482
23	12910	0.4141
24	10320	0.3982
25	10320	0.3689
26	14205	0.4327

27	14205	0.3771
28	14205	0.3836
29	14205	0.3813
30	14205	0.3643
31	14205	0.3086
32	14205	0.3733
33	14205	0.4295
34	14205	0.4301
36	15500	0.3954
37	15500	0.3762
38	15500	0.3762
39	15500	0.4372
40	15500	0.3034
42	10320	0.3785
43	10320	0.3404
44	10320	0.3366
45	10320	0.3366
46	10320	0.3807
47	10320	0.3884
48	10320	0.3486
49	10320	0.3941
50	9030	0.4056
51	9030	0.4185

C

Heterogeneous Calculation Scheme Data

Contains the data from the calculation scheme used as an alternative heterogeneous formulation.

Table C.1: Heterogeneous Model Data: Ammonia Concentrations in kg of ammonia/kg of ammonia-water

Dataset	Speed [RPM]	w_{LL}	w_{VL}
1	10320	0,134	0,676
2	10320	0,146	0,702
3	10320	0,144	0,696
4	10320	0,161	0,745
5	10320	0,161	0,767
6	10320	0,168	0,761
7	10320	0,152	0,723
8	10320	0,166	0,769
9	10320	0,164	0,756
10	10320	0,179	0,782
11	10320	0,150	0,731
12	12910	0,126	0,645
14	12910	0,161	0,749
15	12910	0,140	0,691
16	12910	0,138	0,687
17	12910	0,132	0,672
18	12910	0,122	0,638
19	12910	0,156	0,740
20	12910	0,138	0,683
21	12910	0,152	0,736
22	12910	0,159	0,746
23	12910	0,186	0,792
24	10320	0,175	0,778
25	10320	0,162	0,752
26	14205	0,173	0,773
27	14205	0,154	0,732
28	14205	0,154	0,734
29	14205	0,154	0,733
30	14205	0,134	0,690
31	14205	0,122	0,643
32	14205	0,142	0,709
33	14205	0,176	0,773
34	14205	0,175	0,772

36	15500	0,148	0,720
37	15500	0,135	0,689
38	15500	0,135	0,689
39	15500	0,164	0,753
40	15500	0,121	0,632
42	10320	0,159	0,745
43	10320	0,151	0,719
44	10320	0,148	0,711
45	10320	0,148	0,711
46	10320	0,152	0,731
47	10320	0,162	0,754
48	10320	0,137	0,687
49	10320	0,191	0,804
50	9030	0,173	0,775
51	9030	0,174	0,780

Table C.2: Heterogeneous Model Data: Liquid Fraction of Ammonia

Dataset	**Speed [RPM]**	$\mathbf{q_L}$
1	10320	0,2333
2	10320	0,2030
3	10320	0,2031
4	10320	0,1553
5	10320	0,1522
6	10320	0,1289
7	10320	0,1729
8	10320	0,1420
9	10320	0,1447
10	10320	0,1145
11	10320	0,1615
12	12910	0,2476
14	12910	0,1598
15	12910	0,1968
16	12910	0,1834
17	12910	0,1936
18	12910	0,2397
19	12910	0,1474
20	12910	0,1930
21	12910	0,1598
22	12910	0,1522
23	12910	0,1023
24	10320	0,0942
25	10320	0,1463
26	14205	0,1258
27	14205	0,1547
28	14205	0,1527
29	14205	0,1533
30	14205	0,1784
31	14205	0,1992
32	14205	0,1621
33	14205	0,1188
34	14205	0,1216
36	15500	0,1668

37	15500	0,1933
38	15500	0,1933
39	15500	0,1373
40	15500	0,2330
42	10320	0,1481
43	10320	0,1656
44	10320	0,1732
45	10320	0,1721
46	10320	0,1612
47	10320	0,1371
48	10320	0,1937
49	10320	0,0747
50	9030	0,1171
51	9030	0,1093

Table C.3: Heterogeneous Model Data: Ammonia Concentrations at the Compressor Discharge in kg of ammonia/kg of ammonia-water

Dataset	**Speed [RPM]**	$w_{L,out}$	$w_{v,out}$
1	10320	0,134	0,895
2	10320	0,146	0,890
3	10320	0,144	0,887
4	10320	0,161	0,895
5	10320	0,161	0,918
6	10320	0,168	0,893
7	10320	0,152	0,888
8	10320	0,166	0,910
9	10320	0,164	0,896
10	10320	0,179	0,903
11	10320	0,150	0,907
12	12910	0,126	0,859
14	12910	0,161	0,901
15	12910	0,140	0,882
16	12910	0,138	0,872
17	12910	0,132	0,871
18	12910	0,122	0,883
19	12910	0,156	0,893
20	12910	0,138	0,880
21	12910	0,152	0,900
22	12910	0,159	0,900
23	12910	0,186	0,899
24	10320	0,175	0,885
25	10320	0,162	0,894
26	14205	0,173	0,904
27	14205	0,154	0,894
28	14205	0,154	0,893
29	14205	0,154	0,892
30	14205	0,134	0,879
31	14205	0,122	0,854
32	14205	0,142	0,883
33	14205	0,176	0,899
34	14205	0,175	0,900
36	15500	0,148	0,892

37	15500	0,135	0,886
38	15500	0,135	0,886
39	15500	0,164	0,899
40	15500	0,121	0,859
42	10320	0,159	0,895
43	10320	0,151	0,887
44	10320	0,148	0,887
45	10320	0,148	0,887
46	10320	0,152	0,895
47	10320	0,162	0,898
48	10320	0,137	0,890
49	10320	0,191	0,892
50	9030	0,173	0,899
51	9030	0,174	0,900

Table C.4: Heterogeneous Model Data: Ammonia Concentration at Compressor Discharge in kg of ammonia/kg of ammonia-water

Dataset	**Speed [RPM]**	w_2
1	10320	0,701
2	10320	0,657
3	10320	0,653
4	10320	0,636
5	10320	0,768
6	10320	0,659
7	10320	0,622
8	10320	0,721
9	10320	0,624
10	10320	0,790
11	10320	0,836
12	12910	0,586
14	12910	0,660
15	12910	0,639
16	12910	0,607
17	12910	0,625
18	12910	0,720
19	12910	0,671
20	12910	0,669
21	12910	0,697
22	12910	0,687
23	12910	0,732
24	10320	0,641
25	10320	0,622
26	14205	0,758
27	14205	0,695
28	14205	0,675
29	14205	0,674
30	14205	0,636
31	14205	0,596
32	14205	0,643
33	14205	0,764
34	14205	0,744
36	15500	0,678

37	15500	0,656
38	15500	0,656
39	15500	0,757
40	15500	0,619
42	10320	0,655
43	10320	0,654
44	10320	0,669
45	10320	0,668
46	10320	0,681
47	10320	0,710
48	10320	0,719
49	10320	0,814
50	9030	0,712
51	9030	0,754

Table C.5: Heterogeneous Model Data: Enthalpies at the Compressor Discharge in J/kgK

Dataset	**Speed [RPM]**	$h_{L,out}$	$h_{v,out}$	$h_{2s,het}$	$h_{2,het}$
1	10320	4,8814E+05	1,9683E+06	2,0632E+06	1,5912E+06
2	10320	4,8786E+05	1,9718E+06	2,0680E+06	1,5075E+06
3	10320	4,9531E+05	1,9777E+06	2,0737E+06	1,5106E+06
4	10320	4,5668E+05	1,9561E+06	2,0523E+06	1,4272E+06
5	10320	4,0134E+05	1,9157E+06	2,0003E+06	1,6171E+06
6	10320	4,4849E+05	1,9537E+06	2,0057E+06	1,4674E+06
7	10320	4,6777E+05	1,9657E+06	2,0709E+06	1,4234E+06
8	10320	4,1930E+05	1,9293E+06	2,0140E+06	1,5467E+06
9	10320	4,4087E+05	1,9488E+06	2,0534E+06	1,3881E+06
10	10320	4,3875E+05	1,9421E+06	1,9654E+06	1,7066E+06
11	10320	4,4003E+05	1,9397E+06	1,8876E+06	1,7998E+06
12	12910	5,1615E+05	2,0074E+06	2,0726E+06	1,4516E+06
14	12910	4,4501E+05	1,9464E+06	2,0193E+06	1,4570E+06
15	12910	4,8637E+05	1,9778E+06	1,9953E+06	1,4894E+06
16	12910	4,8732E+05	1,9864E+06	2,0498E+06	1,4451E+06
17	12910	4,9044E+05	1,9885E+06	2,0408E+06	1,4906E+06
18	12910	5,1255E+05	1,9876E+06	2,0007E+06	1,6722E+06
19	12910	4,4746E+05	1,9539E+06	2,0125E+06	1,5001E+06
20	12910	4,9639E+05	1,9833E+06	2,0121E+06	1,5611E+06
21	12910	4,3932E+05	1,9454E+06	2,0221E+06	1,5362E+06
22	12910	4,4359E+05	1,9471E+06	2,0066E+06	1,5158E+06
23	12910	4,3905E+05	1,9446E+06	1,9938E+06	1,5923E+06
24	10320	4,3166E+05	1,9535E+06	1,9931E+06	1,4308E+06
25	10320	4,4534E+05	1,9520E+06	2,0511E+06	1,3926E+06
26	14205	4,3580E+05	1,9402E+06	2,0247E+06	1,6402E+06
27	14205	4,5516E+05	1,9565E+06	2,0413E+06	1,5527E+06
28	14205	4,5174E+05	1,9558E+06	2,0511E+06	1,5119E+06
29	14205	4,5258E+05	1,9565E+06	2,0522E+06	1,5124E+06
30	14205	4,5660E+05	1,9683E+06	2,0691E+06	1,4756E+06
31	14205	4,9958E+05	2,0055E+06	2,0884E+06	1,4758E+06
32	14205	4,5270E+05	1,9642E+06	2,0638E+06	1,4761E+06
33	14205	4,4999E+05	1,9498E+06	2,0112E+06	1,6701E+06
34	14205	4,4596E+05	1,9475E+06	2,0194E+06	1,6253E+06
36	15500	4,5460E+05	1,9572E+06	2,0619E+06	1,5245E+06
37	15500	4,6339E+05	1,9661E+06	2,0736E+06	1,5063E+06

38	15500	4,6339E+05	1,9661E+06	2,0736E+06	1,5063E+06
39	15500	4,5125E+05	1,9505E+06	2,0373E+06	1,6617E+06
40	15500	5,1723E+05	2,0077E+06	2,0824E+06	1,5220E+06
42	10320	4,4608E+05	1,9520E+06	2,0434E+06	1,4614E+06
43	10320	4,7420E+05	1,9695E+06	2,0467E+06	1,4973E+06
44	10320	4,7761E+05	1,9704E+06	2,0511E+06	1,5297E+06
45	10320	4,7759E+05	1,9706E+06	2,0518E+06	1,5281E+06
46	10320	4,4993E+05	1,9529E+06	2,0455E+06	1,5199E+06
47	10320	4,3879E+05	1,9463E+06	2,0277E+06	1,5612E+06
48	10320	4,8213E+05	1,9700E+06	2,0556E+06	1,6330E+06
49	10320	4,2701E+05	1,9456E+06	1,9210E+06	1,7767E+06
50	9030	4,3100E+05	1,9422E+06	2,0253E+06	1,5517E+06
51	9030	4,2308E+05	1,9386E+06	2,0120E+06	1,6334E+06

Table C.6: Heterogeneous Model Data: Power required for Compression [W], the Isentropic and Mechanical Efficiencies

Dataset	**Speed [RPM]**	$\dot{W}_{\mathbf{comp,het}}$	$\eta_{\mathbf{is,het}}$	$\eta_{\mathbf{total,het}}$	$\eta_{\mathbf{mech,het}}$
1	10320	7,4228E+03	0,4889	0,1852	0,3789
2	10320	8,8100E+03	0,4329	0,1828	0,4221
3	10320	9,0136E+03	0,4295	0,1855	0,4319
4	10320	8,6903E+03	0,4231	0,1798	0,4249
5	10320	4,5430E+03	0,6540	0,1858	0,2841
6	10320	7,3780E+03	0,3847	0,1461	0,3797
7	10320	9,1231E+03	0,4157	0,1907	0,4587
8	10320	5,7583E+03	0,5653	0,1856	0,3283
9	10320	8,4437E+03	0,4329	0,1998	0,4614
10	10320	4,4851E+03	0,5168	0,1277	0,2470
11	10320	4,2043E+03	0,1734	0,0484	0,2790
12	12910	1,2553E+04	0,3042	0,1421	0,4671
14	12910	7,9973E+03	0,4028	0,1538	0,3817
15	12910	9,6222E+03	0,2729	0,1050	0,3848
16	12910	1,0221E+04	0,3350	0,1313	0,3919
17	12910	9,4723E+03	0,3328	0,1189	0,3574
18	12910	7,3640E+03	0,3430	0,0981	0,2860
19	12910	7,8452E+03	0,4114	0,1325	0,3221
20	12910	8,6456E+03	0,3311	0,1176	0,3551
21	12910	7,0967E+03	0,4841	0,1460	0,3017
22	12910	7,7754E+03	0,4235	0,1266	0,2988
23	12910	7,0523E+03	0,5607	0,1457	0,2598
24	10320	6,8774E+03	0,3556	0,1317	0,3704
25	10320	8,4487E+03	0,4220	0,1917	0,4542
26	14205	6,6245E+03	0,7524	0,1703	0,2263
27	14205	8,1415E+03	0,5140	0,1407	0,2738
28	14205	8,7391E+03	0,5003	0,1494	0,2986
29	14205	8,7353E+03	0,5011	0,1504	0,3001
30	14205	8,9871E+03	0,4459	0,1463	0,3282
31	14205	1,0622E+04	0,3694	0,1333	0,3607
32	14205	8,8703E+03	0,4602	0,1495	0,3250
33	14205	6,8430E+03	0,6811	0,1502	0,2206
34	14205	7,3138E+03	0,6566	0,1557	0,2372
36	15500	9,2409E+03	0,5116	0,1462	0,2858
37	15500	9,7287E+03	0,4613	0,1289	0,2795
38	15500	9,7287E+03	0,4613	0,1417	0,3071

39	15500	7,1982E+03	0,7278	0,1560	0,2144
40	15500	1,2221E+04	0,3560	0,1244	0,3493
42	10320	7,5240E+03	0,4574	0,1869	0,4087
43	10320	7,9043E+03	0,4228	0,1675	0,3960
44	10320	7,4744E+03	0,4531	0,1683	0,3714
45	10320	7,4978E+03	0,4523	0,1685	0,3725
46	10320	6,7888E+03	0,5018	0,1907	0,3800
47	10320	5,8491E+03	0,5606	0,1813	0,3233
48	10320	6,1608E+03	0,5462	0,1748	0,3201
49	10320	3,7128E+03	0,2699	0,0569	0,2110
50	9030	5,2783E+03	0,5871	0,2005	0,3415
51	9030	4,4262E+03	0,6553	0,1946	0,2970

D

Model Simulation Data

D.1. Base Case Model Data

Table D.1: Simulation Data: Base Case

Dataset	Speed [RPM]	η_{is}	η_{vol}	m_{leak} [kg/s]	m_{flow} [kg/s]
1	10320	0.6683	0.8233	4.2262E-05	4.4849E-02
2	10320	0.6761	0.8279	5.2331E-05	5.5109E-02
3	10320	0.6765	0.8281	5.4145E-05	5.6984E-02
4	10320	0.6839	0.8316	5.6785E-05	5.9670E-02
5	10320	0.6581	0.8203	3.3844E-05	3.7755E-02
6	10320	0.6753	0.8299	5.9867E-05	6.5806E-02
7	10320	0.6815	0.8308	5.3253E-05	5.5587E-02
8	10320	0.6659	0.8246	4.3010E-05	4.7402E-02
9	10320	0.6854	0.8324	5.3302E-05	5.5566E-02
10	10320	0.6196	0.8180	4.9983E-05	6.3591E-02
11	10320	0.5763	0.8159	3.9574E-05	5.4965E-02
12	12910	0.7325	0.8487	7.2876E-05	8.8733E-02
14	12910	0.7173	0.8445	5.7144E-05	7.3877E-02
15	12910	0.7235	0.8460	6.3745E-05	8.0678E-02
16	12910	0.7257	0.8467	6.4545E-05	8.0828E-02
17	12910	0.7218	0.8456	5.9803E-05	7.5699E-02
18	12910	0.7094	0.8405	5.1792E-05	6.7468E-02
19	12910	0.7124	0.8432	5.3784E-05	7.0520E-02
20	12910	0.7134	0.8432	6.0648E-05	7.9188E-02
21	12910	0.7084	0.8417	4.7465E-05	6.2715E-02
22	12910	0.7104	0.8426	5.2830E-05	6.9650E-02
23	12910	0.6856	0.8389	5.9892E-05	8.5147E-02
24	10320	0.6757	0.8309	5.9698E-05	6.6077E-02
25	10320	0.6861	0.8327	5.5473E-05	5.8121E-02
26	14205	0.7093	0.8429	4.9188E-05	7.2878E-02
27	14205	0.7253	0.8463	5.0652E-05	7.0790E-02
28	14205	0.7284	0.8473	5.1306E-05	7.0545E-02
29	14205	0.7284	0.8473	5.1389E-05	7.0675E-02
30	14205	0.7315	0.8490	4.6040E-05	6.0977E-02
31	14205	0.7351	0.8507	5.6758E-05	7.3491E-02
32	14205	0.7316	0.8488	4.8173E-05	6.4379E-02
33	14205	0.7065	0.8424	5.4148E-05	8.0931E-02
34	14205	0.7117	0.8436	5.3908E-05	7.9427E-02

36	15500	0.7397	0.8511	4.7900E-05	6.8426E-02
37	15500	0.7386	0.8521	4.5935E-05	6.3347E-02
38	15500	0.7386	0.8521	4.5935E-05	6.3347E-02
39	15500	0.7303	0.8472	4.8195E-05	7.3809E-02
40	15500	0.7399	0.8537	5.9558E-05	7.9855E-02

D.2. Varying Clearance

Table D.2: Simulation Data: C = 0.1 mm

Dataset	Speed [RPM]	η_{is}	η_{vol}	m_{leak} [kg/s]	m_{flow} [kg/s]
11	10320	0.4329	0.7778	3.0152E-05	5.2397E-02
25	10320	0.5500	0.8081	4.4957E-05	5.6405E-02
12	12910	0.6286	0.8361	6.4672E-05	8.7414E-02
23	12910	0.5775	0.8202	5.2608E-05	8.3248E-02
31	14205	0.6352	0.8392	4.9550E-05	7.2497E-02
33	14205	0.6082	0.8262	4.9121E-05	7.9374E-02
39	15500	0.6355	0.8339	4.4632E-05	7.2650E-02
40	15500	0.6490	0.8438	5.0648E-05	7.8929E-02

Table D.3: Simulation Data: C = 0.15 mm

Dataset	Speed [RPM]	η_{is}	η_{vol}	m_{leak} [kg/s]	m_{flow} [kg/s]
11	10320	0.3819	0.7422	2.7091E-05	5.0000E-02
25	10320	0.3972	0.7639	2.1730E-05	5.3324E-02
12	12910	0.5245	0.8176	5.2088E-05	8.5475E-02
23	12910	0.4672	0.7924	4.0819E-05	8.0421E-02
31	14205	0.5396	0.8230	4.2443E-05	7.1100E-02
33	14205	0.5082	0.8032	4.0501E-05	7.7163E-02
39	15500	0.5464	0.8156	3.8448E-05	7.1057E-02
40	15500	0.5586	0.8305	4.5902E-05	7.7683E-02

D.3. Varying Flow Coefficient for Leakage

Table D.4: Simulation Data: C = 0.05 mm. C_{fl} = 1.4

Dataset	Speed [RPM]	η_{is}	η_{vol}	m_{leak} [kg/s]	m_{flow} [kg/s]
11	10320	0.5413	0.7979	3.7461E-05	5.3753E-02
25	10320	0.6520	0.8200	5.2997E-05	5.7239E-02
12	12910	0.7076	0.8408	7.0103E-05	8.7908E-02
23	12910	0.6592	0.8283	5.8036E-05	8.4062E-02
31	14205	0.7113	0.8434	5.4340E-05	7.2855E-02
33	14205	0.6811	0.8328	5.2811E-05	8.0003E-02
39	15500	0.7059	0.8389	4.6786E-05	7.3084E-02
40	15500	0.7189	0.8471	5.6574E-05	7.9240E-02

Table D.5: Simulation Data: C = 0.05 mm. C_{fl} = 1.6

Dataset	Speed [RPM]	η_{is}	η_{vol}	m_{leak} [kg/s]	m_{flow} [kg/s]
11	10320	0.5035	0.7770	3.4863E-05	5.2345E-02
25	10320	0.6168	0.8057	5.0538E-05	5.6242E-02
12	12910	0.6819	0.8322	6.7466E-05	8.7008E-02
23	12910	0.6318	0.8164	5.5925E-05	8.2861E-02
31	14205	0.6870	0.8354	5.2157E-05	7.2165E-02
33	14205	0.6560	0.8222	5.1298E-05	7.8983E-02
39	15500	0.6815	0.8299	4.5475E-05	7.2295E-02
40	15500	0.6968	0.8400	5.4039E-05	7.8577E-02

Table D.6: Simulation Data: C = 0.05 mm. C_{fl} = 1.8

Dataset	Speed [RPM]	η_{is}	η_{vol}	m_{leak} [kg/s]	m_{flow} [kg/s]
11	10320	0.4610	0.7521	3.1513E-05	5.0665E-02
25	10320	0.5804	0.7894	4.7366E-05	5.5101E-02
12	12910	0.6555	0.8229	6.4944E-05	8.6028E-02
23	12910	0.6031	0.8033	5.3516E-05	8.1526E-02
31	14205	0.6621	0.8267	5.0138E-05	7.1415E-02
33	14205	0.6302	0.8105	4.9503E-05	7.7860E-02
39	15500	0.6568	0.8200	4.4219E-05	7.1434E-02
40	15500	0.6741	0.8324	5.1746E-05	7.7861E-02

Table D.7: Simulation Data: C = 0.05 mm. C_{fl} = 2.0

Dataset	Speed [RPM]	η_{is}	η_{vol}	m_{leak} [kg/s]	m_{flow} [kg/s]
11	10320	0.4095	0.7205	2.6797E-05	4.8540E-02
25	10320	0.5412	0.7702	4.2987E-05	5.3764E-02
12	12910	0.6285	0.8126	6.2513E-05	8.4955E-02
23	12910	0.5727	0.7885	5.0722E-05	8.0030E-02
31	14205	0.6366	0.8172	4.8187E-05	7.0599E-02
33	14205	0.6033	0.7976	4.7443E-05	7.6619E-02
39	15500	0.6319	0.8092	4.2962E-05	7.0494E-02
40	15500	0.6509	0.8241	4.9686E-05	7.7088E-02

D.4. Varying Flow Coefficient for Suction

Table D.8: Simulation Data: C = 0.05 mm. C_{fs} = 0.1

Dataset	Speed [RPM]	η_{is}	η_{vol}	m_{leak} [kg/s]	m_{flow} [kg/s]
11	10320	0.5387	0.8011	3.6814E-05	5.3970E-02
25	10320	0.6435	0.8162	5.1748E-05	5.6973E-02
12	12910	0.6713	0.8285	6.7236E-05	8.6620E-02

23	12910	0.6332	0.8212	5.5651E-05	8.3350E-02
31	14205	0.6727	0.8298	5.2166E-05	7.1683E-02
33	14205	0.6505	0.8239	5.0433E-05	7.9149E-02
39	15500	0.6691	0.8273	4.4669E-05	7.2075E-02
40	15500	0.6745	0.8316	5.4240E-05	7.7786E-02

Table D.9: Simulation Data: C = 0.05 mm. C_{fs} = 0.3

Dataset	**Speed [RPM]**	$\eta_{\mathbf{is}}$	$\eta_{\mathbf{vol}}$	$\mathbf{m_{leak}}$ **[kg/s]**	$\mathbf{m_{flow}}$ **[kg/s]**
11	10320	0.5690	0.8126	3.8935E-05	5.4740E-02
25	10320	0.6785	0.8293	5.4677E-05	5.7884E-02
12	12910	0.7227	0.8451	7.1806E-05	8.8357E-02
23	12910	0.6768	0.8355	5.9030E-05	8.4797E-02
31	14205	0.7252	0.8471	5.5910E-05	7.3177E-02
33	14205	0.6973	0.8390	5.3414E-05	8.0595E-02
39	15500	0.7205	0.8437	4.7527E-05	7.3497E-02
40	15500	0.7299	0.8499	5.8575E-05	7.9505E-02

Table D.10: Simulation Data: C = 0.05 mm. C_{fs} = 0.5

Dataset	**Speed [RPM]**	$\eta_{\mathbf{is}}$	$\eta_{\mathbf{vol}}$	$\mathbf{m_{leak}}$ **[kg/s]**	$\mathbf{m_{flow}}$ **[kg/s]**
11	10320	0.5735	0.8146	3.9318E-05	5.4875E-02
25	10320	0.6833	0.8313	5.5158E-05	5.8028E-02
12	12910	0.7291	0.8474	7.2453E-05	8.8589E-02
23	12910	0.6825	0.8376	5.9552E-05	8.5010E-02
31	14205	0.7317	0.8493	5.6433E-05	7.3372E-02
33	14205	0.7032	0.8411	5.3860E-05	8.0801E-02
39	15500	0.7268	0.8459	4.7935E-05	7.3689E-02
40	15500	0.7365	0.8523	5.9178E-05	7.9724E-02

Table D.11: Simulation Data: C = 0.05 mm. C_{fs} = 0.7

Dataset	**Speed [RPM]**	$\eta_{\mathbf{is}}$	$\eta_{\mathbf{vol}}$	$\mathbf{m_{leak}}$ **[kg/s]**	$\mathbf{m_{flow}}$ **[kg/s]**
11	10320	0.5753	0.8154	3.9485E-05	5.4933E-02
25	10320	0.6852	0.8322	5.5359E-05	5.8088E-02
12	12910	0.7314	0.8482	7.2720E-05	8.8683E-02
23	12910	0.6845	0.8385	5.9771E-05	8.5098E-02
31	14205	0.7339	0.8502	5.6642E-05	7.3449E-02
33	14205	0.7054	0.8420	5.4045E-05	8.0885E-02
39	15500	0.7291	0.8468	4.8103E-05	7.3766E-02
40	15500	0.7388	0.8532	5.9424E-05	7.9809E-02

D.5. Varying Flow Coefficient for Discharge

Table D.12: Simulation Data: C = 0.05 mm. C_{fd} = 0.1

Dataset	Speed [RPM]	η_{is}	η_{vol}	m_{leak} [kg/s]	m_{flow} [kg/s]
11	10320	0.6359	0.8158	5.1456E-05	5.4961E-02
25	10320	0.6605	0.8326	5.9384E-05	5.8118E-02
12	12910	0.7055	0.8487	8.3963E-05	8.8732E-02
23	12910	0.6969	0.8389	7.0644E-05	8.5145E-02
31	14205	0.7097	0.8507	6.6024E-05	7.3491E-02
33	14205	0.7083	0.8424	6.3098E-05	8.0930E-02
39	15500	0.7187	0.8472	5.6236E-05	7.3808E-02
40	15500	0.7173	0.8537	7.0036E-05	7.9855E-02

Table D.13: Simulation Data: C = 0.05 mm. C_{fs} = 0.2

Dataset	Speed [RPM]	η_{is}	η_{vol}	m_{leak} [kg/s]	m_{flow} [kg/s]
11	10320	0.5955	0.8159	4.4247E-05	5.4963E-02
25	10320	0.6736	0.8326	5.7161E-05	5.8120E-02
12	12910	0.7226	0.8487	7.6878E-05	8.8732E-02
23	12910	0.6903	0.8389	6.4769E-05	8.5146E-02
31	14205	0.7252	0.8507	5.9952E-05	7.3491E-02
33	14205	0.7085	0.8424	5.8068E-05	8.0931E-02
39	15500	0.7269	0.8472	5.1361E-05	7.3808E-02
40	15500	0.7313	0.8537	6.3537E-05	7.9855E-02

Table D.14: Simulation Data: C = 0.05 mm. C_{fd} = 0.3

Dataset	Speed [RPM]	η_{is}	η_{vol}	m_{leak} [kg/s]	m_{flow} [kg/s]
11	10320	0.5725	0.8159	4.1064E-05	5.4964E-02
25	10320	0.6785	0.8327	5.6150E-05	5.8121E-02
12	12910	0.7271	0.8487	7.4465E-05	8.8733E-02
23	12910	0.6815	0.8389	6.1807E-05	8.5146E-02
31	14205	0.7301	0.8507	5.7982E-05	7.3491E-02
33	14205	0.7028	0.8424	5.5599E-05	8.0931E-02
39	15500	0.7263	0.8472	4.9442E-05	7.3809E-02
40	15500	0.7360	0.8537	6.1101E-05	7.9855E-02

Table D.15: Simulation Data: C = 0.05 mm. C_{fd} = 0.4

Dataset	Speed [RPM]	η_{is}	η_{vol}	m_{leak} [kg/s]	m_{flow} [kg/s]
11	10320	0.5718	0.8159	4.0012E-05	5.4965E-02
25	10320	0.6830	0.8327	5.5721E-05	5.8121E-02

12	12910	0.7299	0.8487	7.3372E-05	8.8733E-02
23	12910	0.6820	0.8389	6.0470E-05	8.5147E-02
31	14205	0.7329	0.8507	5.7171E-05	7.3491E-02
33	14205	0.7033	0.8424	5.4578E-05	8.0931E-02
39	15500	0.7276	0.8472	4.8579E-05	7.3809E-02
40	15500	0.7383	0.8537	6.0046E-05	7.9855E-02

D.6. Varying Contact Line Length

Table D.16: Simulation Data: C = 0.05 mm. Contact Line Length = 20 mm

Dataset	Speed [RPM]	η_{is}	η_{vol}	m_{leak} [kg/s]	m_{flow} [kg/s]
11	10320	0.5798	0.8167	3.9722E-05	5.5017E-02
25	10320	0.6899	0.8332	5.5709E-05	5.8157E-02
12	12910	0.7353	0.8490	7.3179E-05	8.8764E-02
23	12910	0.6884	0.8394	6.0020E-05	8.5189E-02
31	14205	0.7378	0.8510	5.7043E-05	7.3515E-02
33	14205	0.7093	0.8428	5.4237E-05	8.0967E-02
39	15500	0.7329	0.8475	4.8327E-05	7.3836E-02
40	15500	0.7423	0.8539	5.9932E-05	7.9878E-02

Table D.17: Simulation Data: C = 0.05 mm. Contact Line Length = 40 mm

Dataset	Speed [RPM]	η_{is}	η_{vol}	m_{leak} [kg/s]	m_{flow} [kg/s]
11	10320	0.5739	0.8154	3.9482E-05	5.4931E-02
25	10320	0.6836	0.8323	5.5324E-05	5.8098E-02
12	12910	0.7306	0.8485	7.2674E-05	8.8713E-02
23	12910	0.6838	0.8387	5.9809E-05	8.5118E-02
31	14205	0.7333	0.8505	5.6580E-05	7.3476E-02
33	14205	0.7047	0.8422	5.4090E-05	8.0907E-02
39	15500	0.7284	0.8470	4.8108E-05	7.3790E-02
40	15500	0.7384	0.8535	5.9311E-05	7.9840E-02

Table D.18: Simulation Data: C = 0.05 mm. Contact Line Length = 50 mm

Dataset	Speed [RPM]	η_{is}	η_{vol}	m_{leak} [kg/s]	m_{flow} [kg/s]
11	10320	0.5710	0.8147	3.9360E-05	5.4888E-02
25	10320	0.6805	0.8319	5.5142E-05	5.8067E-02
12	12910	0.7283	0.8483	7.2434E-05	8.8687E-02
23	12910	0.6814	0.8383	5.9700E-05	8.5083E-02
31	14205	0.7311	0.8503	5.6357E-05	7.3456E-02
33	14205	0.7024	0.8419	5.4016E-05	8.0877E-02
39	15500	0.7262	0.8468	4.8003E-05	7.3767E-02
40	15500	0.7364	0.8533	5.9002E-05	7.9821E-02

Table D.19: Simulation Data: C = 0.05 mm. Contact Line Length = 60 mm

Dataset	Speed [RPM]	η_{is}	η_{vol}	m_{leak} [kg/s]	m_{flow} [kg/s]
11	10320	0.5680	0.8141	3.9230E-05	5.4844E-02
25	10320	0.6773	0.8315	5.4953E-05	5.8037E-02
12	12910	0.7260	0.8480	7.2198E-05	8.8660E-02
23	12910	0.6791	0.8379	5.9594E-05	8.5046E-02
31	14205	0.7288	0.8501	5.6137E-05	7.3436E-02
33	14205	0.7001	0.8416	5.3947E-05	8.0847E-02
39	15500	0.7240	0.8465	4.7901E-05	7.3744E-02
40	15500	0.7345	0.8531	5.8709E-05	7.9802E-02

Table D.20: Simulation Data: C = 0.05 mm. Contact Line Length = 70 mm

Dataset	Speed [RPM]	η_{is}	η_{vol}	m_{leak} [kg/s]	m_{flow} [kg/s]
11	10320	0.5650	0.8134	3.9099E-05	5.4799E-02
25	10320	0.6742	0.8310	5.4778E-05	5.8006E-02
12	12910	0.7236	0.8478	7.1967E-05	8.8634E-02
23	12910	0.6768	0.8376	5.9482E-05	8.5010E-02
31	14205	0.7266	0.8498	5.5917E-05	7.3416E-02
33	14205	0.6978	0.8413	5.3880E-05	8.0816E-02
39	15500	0.7217	0.8462	4.7802E-05	7.3721E-02
40	15500	0.7325	0.8529	5.8412E-05	7.9783E-02

D.7. Varying Sealing Line Length

Table D.21: Simulation Data: C = 0.05 mm. Sealing Line Length: Male Rotor Tip: 160 mm. Female Rotor Tip: 120 mm

Dataset	Speed [RPM]	η_{is}	η_{vol}	m_{leak} [kg/s]	m_{flow} [kg/s]
11	10320	0.5866	0.8214	4.0411E-05	5.5339E-02
25	10320	0.6952	0.8367	5.6341E-05	5.8400E-02
12	12910	0.7388	0.8513	7.3671E-05	8.9002E-02
23	12910	0.6931	0.8424	6.0646E-05	8.5494E-02
31	14205	0.7410	0.8531	5.7391E-05	7.3699E-02
33	14205	0.7136	0.8456	5.4723E-05	8.1230E-02
39	15500	0.7367	0.8499	4.8680E-05	7.4044E-02
40	15500	0.7450	0.8558	6.0241E-05	8.0056E-02

Table D.22: Simulation Data: C = 0.05 mm. Sealing Line Length: Male Rotor Tip: 200 mm. Female Rotor Tip: 160 mm

Dataset	Speed [RPM]	η_{is}	η_{vol}	m_{leak} [kg/s]	m_{flow} [kg/s]
11	10320	0.5830	0.8195	4.0121E-05	5.5210E-02
25	10320	0.6921	0.8353	5.6044E-05	5.8304E-02
12	12910	0.7366	0.8504	7.3397E-05	8.8909E-02

23	12910	0.6905	0.8412	6.0387E-05	8.5374E-02
31	14205	0.7389	0.8523	5.7163E-05	7.3627E-02
33	14205	0.7111	0.8445	5.4523E-05	8.1126E-02
39	15500	0.7344	0.8490	4.8514E-05	7.3962E-02
40	15500	0.7433	0.8551	6.0003E-05	7.9987E-02

Table D.23: Simulation Data: C = 0.05 mm. Sealing Line Length: Male Rotor Tip: 240 mm. Female Rotor Tip: 200 mm

Dataset	**Speed [RPM]**	η_{is}	η_{vol}	m_{leak} **[kg/s]**	m_{flow} **[kg/s]**
11	10320	0.5794	0.8176	3.9833E-05	5.5080E-02
25	10320	0.6889	0.8339	5.5740E-05	5.8207E-02
12	12910	0.7344	0.8495	7.3118E-05	8.8815E-02
23	12910	0.6879	0.8400	6.0125E-05	8.5253E-02
31	14205	0.7368	0.8514	5.6943E-05	7.3555E-02
33	14205	0.7087	0.8434	5.4323E-05	8.1022E-02
39	15500	0.7322	0.8481	4.8342E-05	7.3880E-02
40	15500	0.7415	0.8543	5.9764E-05	7.9916E-02

Table D.24: Simulation Data: C = 0.05 mm. Sealing Line Length: Male Rotor Tip: 280 mm. Female Rotor Tip: 240 mm

Dataset	**Speed [RPM]**	η_{is}	η_{vol}	m_{leak} **[kg/s]**	m_{flow} **[kg/s]**
11	10320	0.5758	0.8156	3.9534E-05	5.4948E-02
25	10320	0.6857	0.8325	5.5431E-05	5.8108E-02
12	12910	0.7322	0.8486	7.2838E-05	8.8721E-02
23	12910	0.6853	0.8388	5.9858E-05	8.5131E-02
31	14205	0.7348	0.8506	5.6730E-05	7.3482E-02
33	14205	0.7062	0.8423	5.4122E-05	8.0917E-02
39	15500	0.7299	0.8471	4.8170E-05	7.3798E-02
40	15500	0.7397	0.8536	5.9525E-05	7.9846E-02

Table D.25: Simulation Data: C = 0.05 mm. Sealing Line Length: Male Rotor Tip: 320 mm. Female Rotor Tip: 280 mm

Dataset	**Speed [RPM]**	η_{is}	η_{vol}	m_{leak} **[kg/s]**	m_{flow} **[kg/s]**
11	10320	0.5721	0.8137	3.9238E-05	5.4814E-02
25	10320	0.6825	0.8311	5.5125E-05	5.8009E-02
12	12910	0.7300	0.8477	7.2551E-05	8.8626E-02
23	12910	0.6826	0.8376	5.9591E-05	8.5007E-02
31	14205	0.7327	0.8498	5.6511E-05	7.3408E-02
33	14205	0.7037	0.8412	5.3917E-05	8.0811E-02
39	15500	0.7277	0.8462	4.7994E-05	7.3714E-02
40	15500	0.7379	0.8528	5.9283E-05	7.9775E-02

D.8. Varying Housing Cusp Blow Hole Area

Table D.26: Simulation Data: C = 0.05 mm. Housing Cusp Blow Hole Area = 10mm^2

Dataset	Speed [RPM]	η_{is}	η_{vol}	m_{leak} [kg/s]	m_{flow} [kg/s]
11	10320	0.5843	0.8182	3.9903E-05	5.5122E-02
25	10320	0.6948	0.8343	5.6026E-05	5.8234E-02
12	12910	0.7390	0.8497	7.3583E-05	8.8836E-02
23	12910	0.6920	0.8403	6.0190E-05	8.5284E-02
31	14205	0.7412	0.8516	5.7419E-05	7.3570E-02
33	14205	0.7129	0.8437	5.4371E-05	8.1048E-02
39	15500	0.7364	0.8483	4.8504E-05	7.3899E-02
40	15500	0.7453	0.8545	6.0420E-05	7.9931E-02

Table D.27: Simulation Data: C = 0.05 mm. Housing Cusp Blow Hole Area = 30mm^2

Dataset	Speed [RPM]	η_{is}	η_{vol}	m_{leak} [kg/s]	m_{flow} [kg/s]
11	10320	0.5641	0.8123	3.9047E-05	5.4721E-02
25	10320	0.6731	0.8302	5.4694E-05	5.7947E-02
12	12910	0.7229	0.8472	7.1884E-05	8.8576E-02
23	12910	0.6760	0.8369	5.9425E-05	8.4936E-02
31	14205	0.7258	0.8493	5.5851E-05	7.3371E-02
33	14205	0.6971	0.8406	5.3837E-05	8.0752E-02
39	15500	0.7210	0.8457	4.7755E-05	7.3671E-02
40	15500	0.7319	0.8524	5.8331E-05	7.9740E-02

Table D.28: Simulation Data: C = 0.05 mm. Housing Cusp Blow Hole Area = 40mm^2

Dataset	Speed [RPM]	η_{is}	η_{vol}	m_{leak} [kg/s]	m_{flow} [kg/s]
11	10320	0.5540	0.8091	3.8573E-05	5.4510E-02
25	10320	0.6624	0.8280	5.4101E-05	5.7797E-02
12	12910	0.7148	0.8459	7.1104E-05	8.8443E-02
23	12910	0.6680	0.8351	5.9015E-05	8.4756E-02
31	14205	0.7181	0.8481	5.5138E-05	7.3269E-02
33	14205	0.6893	0.8390	5.3587E-05	8.0599E-02
39	15500	0.7133	0.8443	4.7421E-05	7.3553E-02
40	15500	0.7250	0.8514	5.7410E-05	7.9642E-02

D.9. Validation

Table D.29: Validation of the compressor model with the experimental results for a clearance of 0.05mm using values of the contributing factors giving the lowest possible efficiency.

Dataset	Speed [RPM]	$\eta_{is.model}$	$\eta_{vol.model}$	m_{leak} [kg/s]	m_{flow} [kg/s]
11	10320	0.2876	0.6633	1.2484E-05	4.4682E-02
25	10320	0.3330	0.7006	1.4657E-05	4.8905E-02
12	12910	0.4592	0.7699	4.6445E-05	8.0494E-02
23	12910	0.4489	0.7408	4.5516E-05	7.5186E-02
31	14205	0.4721	0.7756	3.5623E-05	6.7000E-02
33	14205	0.4853	0.7539	3.8310E-05	7.2422E-02
39	15500	0.4917	0.7673	3.6427E-05	6.6847E-02
40	15500	0.4807	0.7827	3.4774E-05	7.3216E-02

Table D.30: Validation of the compressor model with the experimental results for a clearance of 0.15mm using optimum values of the contributing factors.

Dataset	Speed [RPM]	$\eta_{is.model}$	$\eta_{vol.model}$	m_{leak} [kg/s]	m_{flow} [kg/s]
11	10320	0.2462	0.4890	2.3028E-05	3.2940E-02
7	10320	0.3991	0.7605	2.1222E-05	5.0882E-02
25	10320	0.3616	0.7333	1.6249E-05	5.1186E-02
12	12910	0.2922	0.7176	6.6934E-07	7.5019E-02
14	12910	0.2873	0.6640	1.2526E-05	5.8087E-02
23	12910	0.2124	0.5649	1.4150E-05	5.7336E-02
31	14205	0.3047	0.7370	1.5365E-06	6.3672E-02
32	14205	0.2764	0.6887	1.0058E-06	5.2234E-02
33	14205	0.2300	0.6041	1.9472E-05	5.8031E-02
39	15500	0.2341	0.6397	1.2506E-05	5.5731E-02
40	15500	0.3311	0.7565	1.0215E-05	7.0762E-02
36	15500	0.3022	0.7118	4.5460E-06	5.7228E-02

E

Varying the Compressor Port Size

In this Appendix. the effect of varying the compressor port size on the performance of the compressor is seen. Figure 4.15 shows how the axial discharge port scales with respect to the discharge ports of Tang (1995) and Zaytsev (2003). It can be seen that the discharge port used in this study is much larger in comparison. In this Appendix. the discharge port is reduced to 286 mm^2. Table E.1 gives the results of the simulations with the new discharge port size. A difference between the isentropic efficiency of the base case to that obtained with the reduced discharge port size is also found to show the effect of change in size of the discharge port. As can be seen. the isentropic efficiency reduces. on average. 0.43% from the base case. The discharge port area size has no effect on the volumetric efficiency of the compressor since the model uses the mass flow at the suction to compute this efficiency.

Table E.1: Simulation Data: C = 0.05 mm. Discharge Port Area = 286mm^2

Dataset	**Speed [RPM]**	$\eta_{\textbf{is}}$	$\eta_{\textbf{vol}}$	**Difference in** $\eta_{\textbf{is}}$
11	10320	0.5706	0.8159	0.0057
25	10320	0.6806	0.8327	0.0055
12	12910	0.7284	0.8487	0.0042
23	12910	0.6808	0.8389	0.0048
31	14205	0.7314	0.8507	0.0037
33	14205	0.7024	0.8424	0.0041
39	15500	0.7266	0.8472	0.0037
40	15500	0.7371	0.8537	0.0028

The axial suction port is also changed to see its effect on the compressor performance. The axial suction port size was increased to 458 mm^2 and it effect on this compressor performance was noted. On average. the isentropic efficiency increases by 0.054% and the volumetric efficiency increases by 0.025% from the base case.

Table E.2: Simulation Data: C = 0.05 mm. Axial Suction Port Area = 458mm^2

Dataset	Speed [RPM]	η_{is}	η_{vol}	Difference in η_{is}	Difference in η_{vol}
11	10320	0.5768	0.8162	0.0005	0.0003
25	10320	0.6866	0.8329	0.0005	0.0003
12	12910	0.7331	0.8490	0.0006	0.0003
23	12910	0.6862	0.8392	0.0005	0.0003
31	14205	0.7356	0.8510	0.0006	0.0003
33	14205	0.7071	0.8427	0.0006	0.0003
39	15500	0.7308	0.8475	0.0006	0.0003
40	15500	0.7405	0.8539	0.0006	0.0003

Bibliography

Amanatidis, G. European policies on climate and energy towards 2020, 2030 and 2050. Technical report, Policy Department for Economic, Scientific and Quality of Life Policies, European Parliament, 2019.

Chamoun, M., Rulliere, R., Haberschill, P., and Peureux, J. L. Modelica-based modeling and simulation of a twin screw compressor for heat pump applications. *Applied Thermal Engineering*, 58(1-2):479–489, 9 2013. ISSN 13594311. doi: 10.1016/j.applthermaleng.2013.04.020.

Denver, G. Oil-Free (Oil-Less) Air Compressors, 2020. URL https://www.gardnerdenver.com/en-us/knowledge-hub/articles/oil-free-air-compressor-technologies-explained.

Edenhofer, O., Pichs-Madruga, R., Sokona, Y., Agrawala, S., Bashmakov, I., Blanco, G., Broome, J., Bruckner, T., Brunner, S., Bustamante, M., Clarke, L., Creutzig, F., Dhakal, S., Dubash, N., Eickemeier, P., Farahani, E., Fischedick, M., Fleurbaey, M., Gerlagh, R., Gomez Echeverri, L., Gupta, S., Harnisch, J., Jiang, K., Kadner, S., Kartha, S., Klasen, S., Kolstad, C., Krey, V., Kunreuther, H. C., Lucon, O., Masera, O., Minx, J., Mulugetta, Y., Patt, T., Ravindranath, N., Riahi, K., Roy, J., Schaeffer, R., Schlömer, S., Seto, K., Seyboth, K., Sims, R., Skea, J., Smith, P., Somanathan, E., Stavins, R., von Stechow, C., Sterner, T., Sugiyama, T., Suh, S., Urama, K., Ürge-Vorsatz, D., Victor, D., Zhou, D., Zou, J., and Zwickel, T. Summary for policymakers. *Intergovernmental Panel for Climate Change*, 2014.

Fleming, J. S. and Tang, Y. The analysis of leakage in a twin screw compressor and its application to performance improvement, 1995. ISSN 20413009.

Gruijthuijsen, D. A. W. Experimental validation of wet compression with NH3-CO2-H2O (Master Thesis), 2019. URL http://repository.tudelft.nl/.

Gudjonsdottir, V., Kothari, V., Goethals, A., and Infante Ferreira, C. A. Experimental performance of a wet compressor operating with ammonia-water under high temperature compression-resorption heat pump conditions. 2020.

Gudjonsdottir, V. *Upgrading Waste Heat Streams with Wet Compression*. PhD thesis, Delft University of Technology, 2020. URL http://repository.tudelft.nl/.

Guðmundsdóttir, K. Wet compression with a twin screw compressor prototype (Master Thesis), 2018. URL http://repository.tudelft.nl/.

He, Y., Xing, L., Zhang, Y., Zhang, J., Cao, F., and Xing, Z. Development and experimental investigation of an oil-free twin-screw air compressor for fuel cell systems. *Applied Thermal Engineering*, 145: 755–762, 12 2018. ISSN 13594311. doi: 10.1016/j.applthermaleng.2018.09.064.

Itard, L. C. M. and Machielsen, C. H. M. Considerations when modelling compression/resorption heat pumps. Technical report, Delft University of Technology, 1994.

Itard, L. *Wet Compression Resorption Heat Pump Cycles: Thermodynamic Analysis and Design*. PhD thesis, Delft University of Technology, 1998.

Jensen, J. K., Markussen, W. B., Reinholdt, L., and Elmegaard, B. On the development of high temperature ammonia-water hybrid absorption-compression heat pumps. *International Journal of Refrigeration*, 58:79–89, 10 2015a. ISSN 01407007. doi: 10.1016/j.ijrefrig.2015.06.006.

Jensen, J. K., Ommen, T., Markussen, W. B., Reinholdt, L., and Elmegaard, B. Technical and economic working domains of industrial heat pumps: Part 2 - Ammonia-water hybrid absorption-compression heat pumps. *International Journal of Refrigeration*, 55:183–200, 7 2015b. ISSN 01407007. doi: 10.1016/j.ijrefrig.2015.02.011.

Jung, C. W., An, S. S., and Kang, Y. T. Thermal performance estimation of ammonia-water plate bubble absorbers for compression/absorption hybrid heat pump application. *Energy*, 75:371–378, 10 2014. ISSN 03605442. doi: 10.1016/j.energy.2014.07.086.

Jung, C. W., Song, J. Y., and Kang, Y. T. Study on ammonia/water hybrid absorption/compression heat pump cycle to produce high temperature process water. *Energy*, 145:458–467, 2 2018. ISSN 03605442. doi: 10.1016/j.energy.2017.12.141.

Kim, J., Park, S. R., Baik, Y. J., Chang, K. C., Ra, H. S., Kim, M., and Kim, Y. Experimental study of operating characteristics of compression/absorption high-temperature hybrid heat pump using waste heat. *Renewable Energy*, 54:13–19, 6 2013. ISSN 09601481. doi: 10.1016/j.renene.2012.09.032.

Kiss, A. A. and Infante Ferreira, C. A. *Heat pumps in chemical process industry*. CRC Press, 2017. ISBN 9781498718950.

Lemmon, E., Bell, I., Huber, M., and McLinden, M. NIST Standard Reference Database 23: Reference Fluid Thermodynamic and Transport Properties-REFPROP, Version 10.0, National Institute of Standards and Technology. Technical report, Standard Reference Data Program, Gaithersburg, 2018. URL https://www.nist.gov/srd/refprop.

Liu, C., Jiang, Y., Han, W., and Kang, Q. A high-temperature hybrid absorption-compression heat pump for waste heat recovery. *Energy Conversion and Management*, 172:391–401, 9 2018. ISSN 01968904. doi: 10.1016/j.enconman.2018.07.027.

Osenbruck, A. Verfahren zur Kälteerzeugung bei Absorptionsmaschinen, 1895.

Prins, J. and Infante Ferreira, C. Feasibility and design of leakage experiments on a running twin screw compressor. *From Thermo-Economics to Sustainability, edited by Hirs, G.G. Part 2: ECOS 2000 Proceedings*, (University of Twente, Netherlands):869–880, 2000.

Rinder, L. *Schraubenverdichter*. Springer Vienna, 1979. doi: 10.1007/978-3-7091-8554-4.

Shaftel, H., Jackson, R., Callery, S., and Bailey, D. Climate Change: How Do We Know?, 2020. URL climate.nasa.gov/evidence/.

Siegfried, S. *A fundamental equation for the mixture of ammonia and water and the calculation of absorption refrigeration machine processes*. PhD thesis, Ruhr-University Bochum, 1971.

Spoelstra, S. ., Wemmers, A., and Green Marks, R. Dutch program for the Accelaration of Sustainable Heat management in industry: Scoping Study Final report. Technical report, ECN Biomass & Energy Efficiency, 2018.

Tang, Y. *Computer aided design of twin screw compressors*. PhD thesis, University of Strathclyde, 1995.

Taylor, J. *Introduction to error analysis, the study of uncertainties in physical measurements*. University Science Books, 1997, 1997. ISBN 093570275X, 9780935702750. URL https://ui.adsabs.harvard.edu/abs/1997ieas.book.....T/abstract.

Tian, Y., Yuan, H., Wang, C., Wu, H., and Xing, Z. Numerical investigation on mass and heat transfer in an ammonia oil-free twin-screw compressor with liquid injection. *International Journal of Thermal Sciences*, 120:175–184, 10 2017. ISSN 12900729. doi: 10.1016/j.ijthermalsci.2017.06.007.

Van de Bor, D. M. and Infante Ferreira, C. A. Quick selection of industrial heat pump types including the impact ofthermodynamic losses. *Energy*, 53:312–322, 5 2013. ISSN 03605442. doi: 10.1016/j.energy.2013.02.065.

Van De Bor, D. M., Infante Ferreira, C. A., and Kiss, A. A. Optimal performance of compression-resorption heat pump systems. *Applied Thermal Engineering*, 65(1-2):219–225, 4 2014. ISSN 13594311. doi: 10.1016/j.applthermaleng.2013.12.067.

van de Bor, D. M., Infante Ferreira, C. A., and Kiss, A. A. Low grade waste heat recovery using heat pumps and power cycles. *Energy*, 89:864–873, 9 2015. ISSN 03605442. doi: 10.1016/j.energy.2015.06.030.

Wang, C., Xing, Z., Chen, W., Yang, Q., and He, Z. Development of an oil free water-lubricated twin-screw air compressor. *Applied Thermal Engineering*, 143:396–402, 10 2018. ISSN 13594311. doi: 10.1016/j.applthermaleng.2018.07.119.

Wang, C., Xing, Z., Chen, W., Sun, S., and He, Z. Analysis of the leakage in a water-lubricated twin-screw air compressor. *Applied Thermal Engineering*, 155:217–225, 6 2019. ISSN 13594311. doi: 10.1016/j.applthermaleng.2019.04.001.

Yilmaz, M. Performance analysis of a vapor compression heat pump using zeotropic refrigerant mixtures. *Energy Conversion and Management*, 44(2):267–282, 1 2003. ISSN 01968904. doi: 10.1016/S0196-8904(02)00054-7.

Zaytsev, D. *Development of Wet Compressor for Application in Compression - Resorption Heat Pumps.* PhD thesis, Delft University of Technology, 2003. URL http://repository.tudelft.nl/.

Ziegler, B. and Trepp, C. Equation of state for ammonia-water mixtures. *International Journal of Refrigeration*, 7(2):101–106, 1984.